



City Research Online

City, University of London Institutional Repository

Citation: Abdan, S. (2023). Investigation of Mechanical Losses in Oil-flooded, Twin-screw Air Compressors. (Unpublished Doctoral thesis, City, University of London)

This is the accepted version of the paper.

This version of the publication may differ from the final published version.

Permanent repository link: <https://openaccess.city.ac.uk/id/eprint/31485/>

Link to published version:

Copyright: City Research Online aims to make research outputs of City, University of London available to a wider audience. Copyright and Moral Rights remain with the author(s) and/or copyright holders. URLs from City Research Online may be freely distributed and linked to.

Reuse: Copies of full items can be used for personal research or study, educational, or not-for-profit purposes without prior permission or charge. Provided that the authors, title and full bibliographic details are credited, a hyperlink and/or URL is given for the original metadata page and the content is not changed in any way.

Investigation of Mechanical Losses in Oil-flooded, Twin-screw Air Compressors



by
Suraj Abdan

Thesis submitted for the degree of
Doctor of Philosophy
in
Mechanical Engineering

**Centre for Compressor Technology
School of Science and Technology
City, University of London**

August, 2023

I dedicate this thesis to my loved ones...

Acknowledgments

The thesis presented is an outcome of a one-of-a-kind opportunity provided by the collaboration between my employer, Kirloskar Pneumatic Company Limited (KPCL), Pune, India and the Centre for Compressor Technology, City, University of London, London, U.K. where I enrolled as a part-time, external student in April 2017.

No one better than Prof. Stosic, my first supervisor, can teach the screw machines. It is impossible that one will not understand the physics of processes happening inside the screw compressor after his enthusiastic elaborations. His patience, motivation and constant guidance kept me focused during the work. He rightly said once that if anyone starts working with the screw machines, he/she will continue to do so rest of his/her life which I can personally experience now. I feel very honoured to be his student. I would also like to thank my second supervisor, Prof. Kovacevic, for teaching me the basics of screw compressors and giving me continuous input on the study. Being the Principal Investigator of the project as well, he created a very healthy and balanced environment for project deliverables and studies. Without the critical review of the research papers and suggestions for improvement in writing skills and language from Prof. Smith, the publications could not have been possible. The suggestions that he gave turned around the look of the paper and it seemed to have been written by an expert. I wish to extend my gratitude to him.

I wish to thank the management team of Kirloskar for believing in me, providing this opportunity and relieving me from time to time to work on my studies. KPCL's higher management team, Srinivasan K, Sadashib Padhee, Mahesh Nadurkar, Neeraj Bhargava, Pradeep Deore and Neeraj Asati provided me with useful support in many ways. Many thanks to my colleagues and friends who provided the necessary help and advice. Pannkaaaj, Sagar, Sumit, Sham, Abhishek, Nausheen, Yang, Afia and Sun are a few of them who made this journey joyous and created lasting memories.

Finally, I am highly indebted to my wife, parents, sister and grandparents as they sacrificed a lot of things to see me achieve what I wanted to achieve. I wish I could have spent more quality time with them which I will do now.

Suraj Abdan
Pune, India,
August, 2023

Declaration

I, Suraj Kuber Abdan, hereby declare that except where specific reference is made to the work of others, the contents of this dissertation are original and have not been submitted in whole or in part for consideration for any other degree or qualification in this or any other university. This dissertation is my own work and contains nothing which is the outcome of work done in collaboration with others, except where specified in the text.

Suraj Abdan
August, 2023

Abstract

Approximately 15-20% of the world's generated electrical power is consumed by compressors where rotary oil-lubricated compressors account for nearly 60% of the entire air compressor market. According to market research, the demand for those of the twin-screw type is likely to increase at a Compound Annual Growth Rate (CAGR) of 5% from 2021 to 2026. Thus, even minor improvements in their efficiency can lead to a substantial reduction in carbon footprint.

With the increasing demand for more energy-efficient machines, one of the ideas in the screw compressor for optimising their performance is to focus on reducing power loss. To do this, the elements contributing to the power loss and their quantification need to be understood. Analytical procedures for the design and performance estimation of twin screw compressors are well-developed and widely available, but the determination of power loss, in oil-flooded machines is only approximated.

This study focuses on finding the elements of power loss arising from the oil-injected, twin-rotor screw compressor and quantifying the contribution of individual elements' power loss for different compressor sizes. The approach is to find available technologies and develop new methods for the prediction of power loss in elements like rolling element bearings, shaft seals, oil drag and transmission.

After a comparison of available methods bearing power loss prediction and literature available experimental results, the Harris model fits best for the prediction of power loss arising from rolling element bearing. Based on the semi-analytical approach and experimental measurement presented by Frölich et al. (2014) and Engelke (2011), respectively, a combined model is developed for the prediction of power loss from the shaft seals. As the oil in the compressor experiences inertial and pressure-induced flow, a combined Couette-Poiseuille flow model is established for drag loss estimation. This drag loss model is experimentally validated with different screw rotor profile configurations. It is understood from the predictions for total power loss and its comparison for different sizes of the compressor, that the bearing power loss and oil drag loss are the main contributing elements to the total power loss whereas shaft seal power loss is negligible.

With the use of the proposed method and parametric analysis, the elements contributing to power loss and the effect of different operational parameters like pressure ratio, speed and size of the compressor are analysed. This can help the designers to optimise the working of the compressor at the design stage.

Contents

Acknowledgments	v
Abstract	ix
List of Figures	xv
List of Tables	xix
List of Symbols	xxi
1 Introduction	1
1.1 Introduction	1
1.2 Rotary Compressors	3
1.2.1 Vane Compressor	4
1.2.2 Liquid Ring Compressor	4
1.2.3 Lobe Compressor	5
1.2.4 Screw Compressor	6
1.3 Development of Screw Machines	6
1.4 Types of Screw Machines	8
1.4.1 Twin-rotor Screw Compressor	8
1.4.2 Single-rotor Screw Compressor	10
1.4.3 Other Types of Screw Compressor	11
1.4.3.1 Variable Lead Twin Screw Compressor	11
1.4.3.2 Tri-rotor Screw Compressor	12
1.4.3.3 Internal Conical Rotary Screw Compressor	13
1.4.3.4 Internally Geared Parallel Rotor Machine	14
1.5 Air Screw Compressor System	14
1.6 Motivation to Investigate Screw Compressor System	16
2 Literature Review	19
2.1 Introduction	19
2.2 Screw Compressor	21
2.2.1 Twin-rotor Screw Compressor Geometry	21
2.2.2 Screw Compressor Mathematical Models	23

2.2.3	Bearing Power Loss	25
2.2.3.1	SKF model	25
2.2.3.2	Harris model	25
2.2.3.3	Palmgren model	25
2.2.3.4	Comparison of SKF, Harris and Palmgren model . .	26
2.2.3.5	PDSim bearing model	33
2.2.4	Radial Shaft Seal Power Loss	34
2.2.5	Oil Drag Loss	38
2.2.5.1	Analytical Models	39
2.2.5.2	Computational Models	45
2.2.5.3	Experimental Investigation	46
2.3	Power Transmission Loss	47
2.3.1	Gear Drive	47
2.3.1.1	Power loss in mesh, under load, for a single gear pair	47
2.3.1.2	Power loss in idle motion	50
2.3.2	Belt Drive	52
2.4	Electric Motors and Frequency Converter Losses	52
2.5	Summary	54
3	Research Aims	57
3.1	Aim of Research	58
3.2	Methods Used	58
3.3	Expected Contribution	58
4	Development of Power Loss Model	61
4.1	Introduction	61
4.2	Bearing Power Loss	62
4.2.1	SKF model	62
4.2.1.1	Rolling frictional moment	63
4.2.1.2	Sliding frictional moment	65
4.2.1.3	Drag loss	66
4.2.2	Harris model	68
4.2.2.1	Torque due to applied load	69
4.2.2.2	Torque due to viscous lubricant friction	70
4.2.2.3	Torque due to roller end-roller flange sliding friction	71
4.2.3	Palmgren model	72
4.2.4	Comparison of predictions from SKF, Harris and Palmgren model	73
4.3	Oil Drag Loss	75
4.4	Summary	82

5	Case Studies and Parametric Analysis	85
5.1	Introduction	85
5.2	Case Study on Bearing Power Loss	85
5.2.1	Oil injected compressor	85
5.2.1.1	Type and magnitude of the load	86
5.2.1.2	Effect of pressure ratio and shaft speed	87
5.2.1.3	Effect of size and load	88
5.3	Case Study on Radial Shaft Seal Power Loss	89
5.3.1	Effect of shaft speed	89
5.3.2	Effect of shaft diameter	89
5.3.3	Effect of surface roughness	90
5.3.4	Effect of oil temperature	90
5.4	Case Study on Oil Drag Loss	91
5.4.1	Effect of compressor size	91
5.4.2	Effect of pressure ratio	93
5.4.3	Effect of oil viscosity	94
5.4.4	Effect of various clearances	95
5.4.5	Comparison of Couette and Poiseuille flow in clearance	96
5.4.5.1	Effect of tip speed and radial clearance	96
5.4.5.2	Effect of pressure ratio and radial clearance	97
5.5	Case Study on Gear Power Loss	98
5.6	Contribution of each Element to Power Loss	100
5.7	Summary	101
6	Experimental Validation and Discussions	105
6.1	Introduction	105
6.2	Experimental Validation of Drag Loss Predictions	105
6.2.1	Drag loss model	105
6.2.1.1	Rotor profiles designed for different levels of drag losses	106
6.2.1.2	Experimental measurements	107
6.2.1.3	Summary	110
6.2.2	Accuracy and Uncertainty Analysis	114
6.3	Experimental Validation of Total Power Predictions	116
6.3.1	Test rig	117
6.3.2	Instrumentation and data acquisition	118
6.3.3	Results	121
6.4	Regression Analysis	123
6.4.1	Summary of regression analysis	127
6.5	Summary	127

7	Conclusions and Recommendations for Future Work	129
7.1	Summary of Research	129
7.2	Conclusions	131
7.3	Future Work	132
	Appendices	133
A	SKF Model	135
B	Palmgren Model	149
C	Harris Model	151
D	Shaft Seal Power Loss	155
E	Drag Loss	157
	References	167
	List of Publications	175

List of Figures

1.1	Global stationary air compressor market size, by Application, 2020 (GMI, 2022)	2
1.2	Classification of compressors (Yen, 2022)	2
1.3	Typical application ranges of compressor types	3
1.4	Vane compressor (Mechanical-Jungle, 2022; Ref-Wiki, 2022)	4
1.5	Liquid ring compressor (Compressed-Air-Blog, 2022)	5
1.6	Lobe compressor (Chaprabazaar, 2022)	5
1.7	Working principle of a twin screw compressor (Rane, 2015)	9
1.8	Typical pressure and volume variation in a twin screw compressor (Rane, 2015)	9
1.9	Geometry and basic components of a single-screw compressor (Wu and Feng, 2008)	10
1.10	Meshing of twin-screw uniform and variable lead rotors (Kovacevic and Stosic, 2013)	11
1.11	Tri rotor screw compressor (Jacobs, 2006)	12
1.12	Conical screw profile (Vert, 2021)	13
1.13	Internally geared parallel rotor machine (Read et al., 2017)	14
1.14	Schematic of air screw compressor package (Compressed-Air-Best-Practices, 2022)	15
1.15	Global stationary air compressor market size, by Technology (GMI, 2022)	17
1.16	Global stationary air compressor market share, by Region (GMI, 2022)	17
2.1	Sankey diagram of power	19
2.2	A cross-section of the bare screw compressor of Kirloskar Pneumatic Company Limited	20
2.3	Effect of oil temperature on load independent friction torque (Tu, 2016)	27
2.4	Effect of oil level on load independent friction torque (Tu, 2016)	27
2.5	Effect of oil type on load independent friction torque (Tu, 2016)	28
2.6	Effect of oil level on load-dependent friction torque (Tu, 2016)	29
2.7	Effect of oil type on load-dependent friction torque (Tu, 2016)	30
2.8	Effect of different loads on load-dependent friction torque (Tu, 2016)	31

2.9	Frictional torque of ball bearing from experimental data at different loads (Gradu, 2000)	32
2.10	Frictional torque of ball bearing from the output of existing models at different loads	32
2.11	PDSim Bearing frictional loss methods (Bell et al., 2020)	33
2.12	Schematics of journal and slider bearings (Bell et al., 2020)	34
2.13	Flow chart of iteration for seal frictional moment calculation	37
2.14	Scopes of modelling	42
2.15	Vibration factor (Jelaska, 2012)	49
2.16	Power flow of single-phase induction motor (Bell et al., 2020)	54
2.17	A 55 kW, air screw compressor unit of Kirloskar Pneumatic Company Limited	55
4.1	Shearing of lubricant (SKF, 2018)	63
4.2	Drag loss factor (SKF, 2018)	67
4.3	Bearing oil level (SKF, 2018)	68
4.4	Different clearances within the screw compressor	76
4.5	Couette-Poiseuille velocity profile	77
4.6	Oil volume fraction on a cross-sectional plane in the twin-screw compressor at injection (Basha et al., 2018)	79
4.7	Shear flow region for radial clearance	81
4.8	Shear flow region for axial clearance	81
4.9	Shear flow region for interlobe clearance	82
5.1	Type and magnitude of the load on different bearings	86
5.2	Frictional power loss in bearings	87
5.3	Effect of pressure ratio and speed on bearing power loss	88
5.4	Oil injected bearings power loss	88
5.5	Seal power loss v/s shaft speed	89
5.6	Seal power loss v/s shaft diameter	90
5.7	Seal power loss v/s shaft surface roughness	90
5.8	Seal power loss v/s oil temperature	91
5.9	The effect of different sizes of the screw compressor on drag loss elements with respect to speed	92
5.10	Effect of pressure ratio on drag loss with respect to speed for size 2 compressor	93
5.11	Effect of oil viscosity on drag loss for different sizes of compressors and pressure ratio 8.5	94
5.12	Effect of various clearances on drag loss at pressure ratio 8.5 with speed for size 2 compressor	95
5.13	Effect of tip speed and radial clearance on drag loss	97
5.14	Effect of pressure ratio and radial clearance on drag loss	98

5.15	Power loss v/s input power	99
5.16	Power loss v/s gear ratio	99
5.17	Transmission efficiency v/s gear ratio	100
5.18	Contribution of each element of power loss	101
6.1	Schematic representation of slanting female rotor top land in ‘beta-1’, ‘beta-2’ and ‘beta-3’ profiles compared to the flat land on ‘N’ profile	106
6.2	Schematic representation of ‘N’, ‘beta-1’ and ‘beta-2’ female rotor top lands where oil film shears in the radial gap	107
6.3	A Kirloskar 55 kW oil-flooded, twin-screw, air compressor package	108
6.4	Actual photographs of rotors with the tweaked profiles ‘beta-1’, ‘beta-2’ and ‘beta-3’	109
6.5	Schematic of air and oil flow through the compressor package (Prasanna, 2023)	110
6.6	Compressor test rig – 141mm compressor	117
6.7	Compressor test rig - Auxiliary systems	118
6.8	Labview front panel of experiment monitoring	121
6.9	Total shaft power of 98mm compressor	122
6.10	Total shaft power of 141mm compressor	122
6.11	Total shaft power of 231mm compressor	123
6.12	Prediction v/s Regression analysis: Bearing power loss	126
6.13	Prediction v/s Regression analysis: Shaft seal power loss	126
6.14	Prediction v/s Regression analysis: Oil drag loss	127

List of Tables

2.1	Relative radial shaft seal force for different materials	36
2.2	Rough values of factor K_A application (Jelaska, 2012)	48
2.3	Correction factor (Jelaska, 2012)	49
4.1	Geometric constants K_Z and K_L (SKF, 2018)	64
4.2	Geometric constants G_{rr} and G_{sl} (SKF, 2018)	66
4.3	Values of Z and y (Harris and Kotzalas, 2007)	69
4.4	f_1 for cylindrical roller bearings (Harris and Kotzalas, 2007)	69
4.5	Values of f_o for ball bearing type and lubrication (Harris and Kotzalas, 2007)	70
4.6	Values of f_o for cylindrical roller bearing type and lubrication (Harris and Kotzalas, 2007)	71
4.7	Values of f_f for cylindrical roller bearings (Harris and Kotzalas, 2007)	71
4.8	Size 1: Bearing power loss predictions at 3,500 rpm	74
4.9	Size 2: Bearing power loss predictions at 3,000 rpm	74
4.10	Size 3: Bearing power loss predictions at 3,000 rpm	75
5.1	Bearings used in screw compressors	86
6.1	Profile geometric characteristics and assembly clearances	108
6.2	Drag loss prediction for ‘N’, ‘beta-1’, ‘beta-2’ and ‘beta-3’	111
6.3	Flow and shaft power predictions for ‘N’, ‘beta-1’, ‘beta-2’ and ‘beta-3’	112
6.4	Experimental measurements for flow and shaft power for ‘N’, ‘beta-1’, ‘beta-2’ and ‘beta-3’	112
6.5	A comparison of prediction and measured shaft power ‘N’, ‘beta-1’, ‘beta-2’ and ‘beta-3’	113
6.6	Accuracy of instruments	114
6.7	Uncertainty Analysis of ‘N’ and ‘beta-1’ Measurements	115
6.8	Uncertainty Analysis of ‘beta-2’ and ‘beta-3’ Measurements	116
6.9	Measurement and instrumentation listing	120
6.11	Constants for power loss in bearing, shaft seal and oil drag	125

List of Symbols

α	bearing nominal contact angle, Harris [°]	59
α_t	pressure angle in transverse plane [°]	41
α_w	pressure angle in pitch circle [°]	41
β_b	helix angle at base circle [°]	41
ϵ_1	partial contact ratio of pinion	41
ϵ_2	partial contact ratio of wheel	41
ϵ_α	transverse plane contact ratio	41
η	dynamic viscosity, Palmgren [mPa.s]	61
η_{50}	dynamic viscosity of oil at operating temperature of 50°C [Pa.s]	41
η_{oil}	dynamic viscosity of oil at operating temperature [mPa.s]	39
μ_{bl}	coefficient depending on the additive package in the lubricant, SKF	55
μ_{EHL}	sliding friction coefficient in full-film conditions, SKF	55
μ_{mZ}	mean coefficient of friction in mesh	39
μ_{sl}	sliding friction coefficient, SKF	54
ν	actual operating viscosity of oil or the base oil of the grease, SKF [mm ² /s]	52
ν	kinematic viscosity [m ² /s]	41
ν_o	kinematic viscosity of lubricant, Harris [cSt]	59
ν_{oil}	kinematic viscosity of oil [mm ² /s]	43
ω	angular velocity of the bearing rings in relation to each other, Palmgren [rad/s]	61
ϕ_{bl}	weighting factor for sliding friction coefficient, SKF	55
ϕ_{ish}	inlet shear heating reduction factor, SKF	52

ϕ_{rs}	kinematic replenishment/starvation reduction factor, SKF.....	52
π	pressure ratio.....	73
ρ_{cn}	equivalent radius of meshed profiles [mm].....	39
ρ_{cn}	equivalent radius of meshed profiles curvature at pitch point C [mm]	41
ρ_{oil}	lubricant density [kg/dm ³].....	43
ϑ_{oil}	operating temperature of oil [°C].....	41
a	centre distance [mm].....	41
A_K	inside surface of the gear drive housing near the wheel gear [m ²] ...	42
B	bearing width, SKF [mm].....	56
b	gear width [mm].....	43
C_1	bath lubrication factor for gear width.....	42
C_2	bath lubrication factor for depth of diving in the oil bath.....	42
C_s	basic static load rating, Harris [N].....	58
C_w	variable, SKF.....	56
C_{Sp}	factor of oil spraying.....	42
D	bearing outside diameter, SKF [mm].....	56
d	bearing bore diameter, SKF [mm].....	56
d	diameter [mm].....	43
d_m	bearing mean diameter, SKF [mm].....	53
d_w	pitch diameter of dived gear [mm].....	43
e	base of natural logarithm, SKF.....	53
e_1	depths of diving of the pinion [mm].....	43
e_2	depths of diving of the gear [mm].....	43
e_{max}	maximum of two values e_1 and e_2 of the diving depth of mated gears [mm].....	42
f_1	factor depending on the bearing design and relative bearing load, Harris	58
F_a	axial load, Harris [N].....	59

f_A	variable, SKF	57
f_F	correction factor for K_V	40
f_f	factor for the type of cylindrical roller bearing, lubricant and lubrication method, Harris	60
f_o	factor depending on the type of bearing and method of lubrication, Harris	59
F_r	radial load, Harris [N]	59
F_s	static equivalent load, Harris [N]	58
F_t	reference circle peripheral force [N]	39
f_t	variable, SKF	56
F_β	factor which depends on the magnitude and direction of the applied load, Harris	58
$g_1 P_0$	factor, Palmgren	61
G_{rr}	variable depending on bearing type, mean diameter and loads, SKF	52
G_{sl}	variable depending on bearing type, mean diameter and loads, SKF	54
H	height of oil level, SKF [mm]	57
h_c	height of the pitch point over the deepest dive point [mm]	42
H_V	factor of power losses in the mesh	39
i_{rw}	number of ball rows, SKF	56
k	total number of gear pairs in a drive	43
K_A	application factor	39
K_L	roller bearing type related geometric constant, SKF	56
K_V	internal dynamic factor	39
k_v	vibration factor	40
K_Z	bearing type related geometric constant, SKF	56
K_Z	bearing type related geometric constant, SKF	53
$K_{B\alpha}$	transverse load factor	39
$K_{B\beta}$	face width factor	39

$K_{B\gamma}$	helix angle factor	39
K_{ball}	ball bearing constant, SKF	56
K_{roll}	rolling bearing constant, SKF	56
K_{rs}	replenishment/starvation constant, SKF	53
l_D	variable, SKF	57
l_h	hydraulic length of the gear drive housing [mm]	42
M	total friction torque, Harris [Nmm]	61
M	total frictional moment, SKF [Nmm]	52
M_f	torque applied due to roller end-roller flange sliding friction, Harris [Nmm]	60
M_l	load dependent friction torque, Palmgren [Nm]	61
M_l	torque due to applied load, Harris [Nmm]	58
m_n	normal module [mm]	43
M_o	load independent friction torque, Palmgren [Nm]	61
M_v	torque due to lubricant viscous friction, Harris [Nmm]	59
M_{drag}	frictional moment of drag losses, churning, splashing etc., SKF [Nmm] 52	
M_{rr}	rolling frictional moment, SKF [Nmm]	52
M_{seal}	frictional moment of seals, SKF [Nmm]	52
M_{sl}	sliding frictional moment, SKF [Nmm]	52
n	rotational speed, SKF [rpm]	52
O	perimeter of the inside surface of gear drive housing near the wheel gear [mm]	42
p	difference between atmospheric pressure and the vaporization pressure of the oil in Palmgren model, Palmgren [kg/mm ²]	61
p	pressure [Pa]	67
P_Z	total power loss in gear mesh [W]	43
P_{loss}	bearing frictional power loss, SKF [W]	52
P_{Z0}	power loss in idle motion [W]	43

P_{ZP}	power loss in gear mesh under load [kW]	39
Q_e	quantity of lubricant sprayed [dm ³ /min]	43
Q_{e0}	constant, 2 dm ³ /min	43
R_a	arithmetic mean roughness [μ m]	39
R_s	variable, SKF	56
t	variable, SKF	57
T_H	hydraulic moment of power loss [Nm]	42
u	gear ratio	40
u, v and w	velocity [m/s]	67
v	peripheral speed [m/s]	40
v	reference circle peripheral speed [m/s]	43
v	reference circle peripheral speed of dived gear [m/s]	42
V_M	drag loss factor, SKF	56
v_s	speed of sprayed lubricant [m/s]	43
$v_{\Sigma C}$	sum of the peripheral speeds in pitch point [m/s]	39
v_{t0}	speed constant, 10 [m/s]	42
w_{Bt}	specific tooth load in transverse plane [N/m]	39
x, y and z	spatial coordinates	67
z_1	number of teeth on pinion	40
z_2	number of teeth on wheel	41

Chapter 1

Introduction

1.1 Introduction

Compressors are used to increase the pressure of the compressible fluid. The fluid can be either gas or vapour, with a variety of molecular weights. The inlet pressure can range from vacuum to positive pressure, while the discharge pressure can range from atmospheric to thousands of bar. A variety of applications for compressed gas makes compressors an essential part of ever-increasing industrialisation. Typically compressed gas is used in Oil and Gas, Process Gas extraction, Refrigeration and Air-conditioning, Civil Engineering, Building industry and Manufacturing industry; the Manufacturing industry is one of the biggest users of compressors as shown in Figure 1.1. Although the numbers shown in Figure 1.1 are not presented in the original reference, these are calculated based on certain measurements and are indicative.

Based on compression methods, mainly effected by mechanical motion, the compressors can be divided into two groups, either positive displacement compressors or dynamic compressors. The positive displacement compressors work in cycles wherein a specific quantity of the gas is moved into the compressor, compressed and discharged from the compressor. This cycle is repeated, thus providing the intermittent flow of the compressed gas.

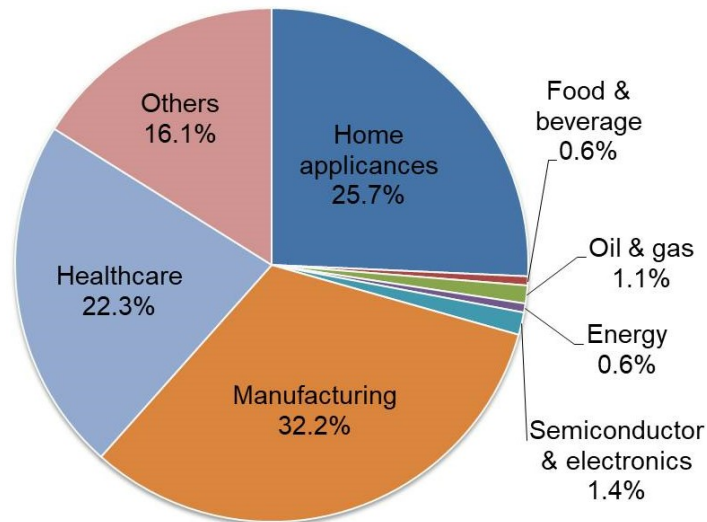


Figure 1.1: Global stationary air compressor market size, by Application, 2020 (GMI, 2022)

In the case of dynamic compressors, the gas is compressed less intermittently, as compared to positive displacement compressors, during the compression process; hence they are continuous flow compressors. The classification of commonly used industrial compressors is shown in Figure 1.2.

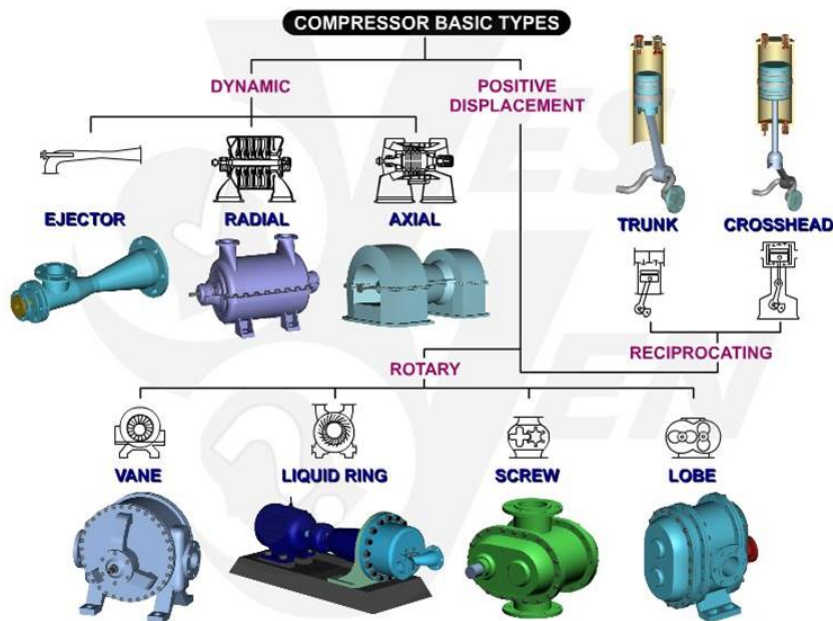


Figure 1.2: Classification of compressors (Yen, 2022)

Positive displacement compressors work on the principle of reduction of the gas volume to increase its pressure. This reduction in volume is achieved by reducing the volume of the working chamber where the gas is compressed. Two distinct types

of positive displacement compressors are referred to as; reciprocating and rotary compressors.

In dynamic compressors, energy is transferred to the gas from a moving set of blades. The rapidly rotating element accelerates the gas as it passes through it, converting the kinetic energy to pressure, partially in the rotating element and partially in stationary diffusers or blades.

A typical application range of these compressors is shown in Figure 1.3. The reciprocating compressors are used in low-medium flow rate and medium-high pressure ratios. The rotary compressors best suit the medium flow rate and medium pressure ratio, while the dynamic compressors are used for high flow and low-medium pressure ratios.

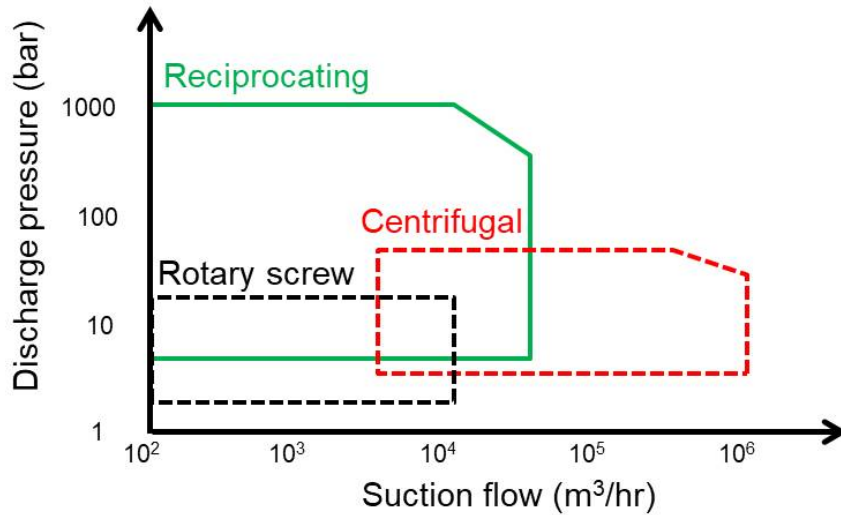


Figure 1.3: Typical application ranges of compressor types

1.2 Rotary Compressors

Rotary compressors are a part of positive displacement compressors, where the gas is compressed by one or multiple rotating elements. This being a type of positive displacement compressor, the compression is performed in an intermittent mode. In reciprocating compressors, the rotary motion of the prime mover is converted into linear motion, which inherently makes them mechanically less efficient. Whereas in the case of rotary compressors, the rotary motion of the prime mover is directly transferred to rotate the rotor/s to create pressure. This enables rotary machines to

run at higher speeds, making them one of the most efficient compressors with high mechanical and volumetric efficiency. As indicated in Figure 1.2, several types of rotary compressors are explained in the next section.

1.2.1 Vane Compressor

The construction of a sliding-vane compressor consists of a single rotating element. The cylindrical housing and the rotor are mounted eccentrically. The rotor has slots fitted with vanes, as shown in Figure 1.4. As the rotor rotates inside the housing, the vanes oscillate in and out of the slots. The gas is trapped between a pair of vanes when the slots pass the inlet port. The successive rotation of the rotor reduces the trapped gas volume and increases the pressure before it is discharged into the port.

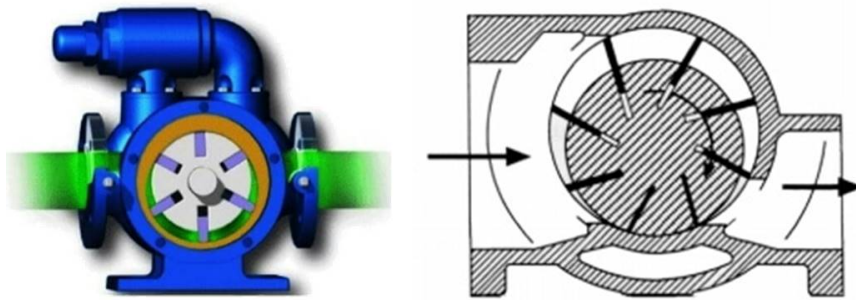


Figure 1.4: Vane compressor (Mechanical-Jungle, 2022; Ref-Wiki, 2022)

This configuration is widely used as a compressor and as a vacuum pump. The disadvantage of this type of compressor is that the discharge pressure is limited if the suction pressure is atmospheric. However, it can also be used as a booster compressor to deliver discharge pressure up to 27 bar. Because these compressors are not flexible to capacity control and the high cost of multi-staging limits the use of Vane compressors in certain applications.

1.2.2 Liquid Ring Compressor

Similar to rotary vane compressors, an offset rotor is placed in a cylindrical housing of the liquid ring compressors. The fluid, mainly water, is fed into the housing, which is thrown towards the periphery of the housing because of the centrifugal action. The void created at the rotor centre draws the gas inside the compression chamber from the inlet port. Further rotation of the rotor compresses the gas within the chamber

and is finally released through the discharge port, as shown in Figure 1.5.

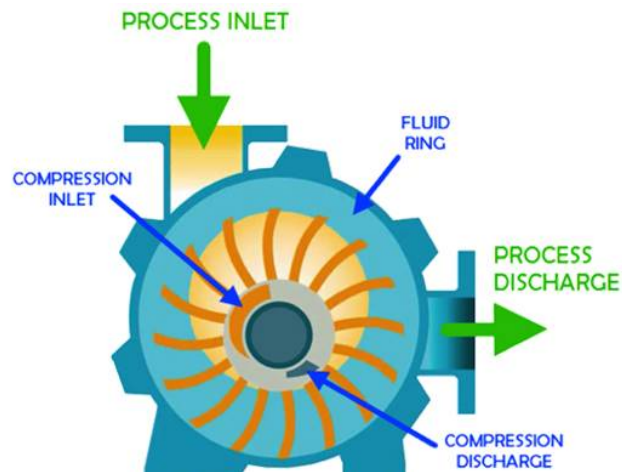


Figure 1.5: Liquid ring compressor (Compressed-Air-Blog, 2022)

This type of machine is being used not only as a compressor but also as a vacuum pump. Since the gas is washed through the liquid, liquid ring compressors are better suited for harsh environments and can tolerate contaminants.

1.2.3 Lobe Compressor

The Lobe compressor, also commonly known as Roots Blower, consists of two un-twisted or straight lobes that intermesh, as shown in Figure 1.6. Generally, the rotor pair used is a twin-lobe configuration, but three-lobe configuration rotors are also available.

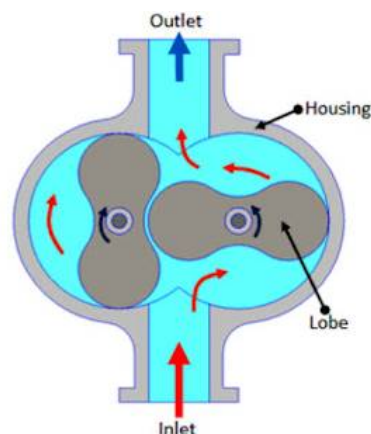


Figure 1.6: Lobe compressor (Chaprabazaar, 2022)

The lobes do not contact each other as they are driven through the timing gears. As they rotate, the gas is trapped between the lobes once they pass through the

inlet port. The backflow from the discharge port compresses the gas. In the two-lobe configuration, four cycles of compression take place in the period of one shaft revolution. These compressors are used for low-volume flow rates and low discharge pressures of up to 1 bar for a single stage and 1.5 bar for two stages. Lack of internal compression, limited pressure range and application where noise matter limits the usage of Lobe compressors.

1.2.4 Screw Compressor

When the straight lobes of the lobe compressor are twisted, it becomes the helical lobe, generally referred to as the screw rotor. The gas is compressed in two inter-meshing screw rotors and the compression housing. When the interlobe of the screw rotor passes over the suction port, it traps a quantity of gas. Subsequent rotation of screw rotors moves gas in the axial and circumferential direction and reduces the volume of the trapped gas. This reduction in the volume increases the pressure of the gas. The position of the discharge port controls the compression ratio within the compressor.

The advantage of the screw machines is lower contact forces because of the involute meshing at the contact faces and the design of the rotor profile. This allows minimum torque acting on the driven rotor and better reliability than other positive displacement machines. The development of screw machines, different types and their advantages over other configurations are discussed in the next section.

1.3 Development of Screw Machines

The performance of the screw machine is mainly a function of the shape of the screw rotor profile. Alf Lysholm, a Swedish Engineer, began working on the development of high-speed screw compressors in the nineteen thirties. Although the screw compressor was first patented in 1878 by Heinrich Krigar in Germany (Brown, 1997), its workable design was first prototyped, as an oil-free screw compressor, by Alf Lysholm in 1934. This design was not easy to manufacture using the manufacturing technology available in those days. Until the mid-nineteen sixties, these machines were not widely used due to the inability to manufacture the rotors accurately at a reasonable

cost.

The single most significant advance in screw compressor performance was achieved through the adoption of asymmetric rotor profiles in screw rotors around the nineteen seventies, as seen in the patents by Lysholm (1967), Persson (1968) and Schibbye (1970). The development and supply of thread milling machines, in 1952, by Holroyd, UK to Howden Company in the UK contributed significantly to the development of oil-flooded screw compressors. The introduction of “A” screw rotor profile in nineteen seventy-three by SRM, a Swedish company, accelerated the use of screw machines. Increased efficiency of the screw machines was realised with SRM “A” profile which reduced the internal leakage path area, also known as blow hole area, by 90%. With the advent of oil-flooded machines, the stage pressure ratios could be increased while maintaining higher operational efficiencies that lead to the wide use of screw compressors (Stosic et al., 2005).

During mid nineteen eighty, using CAD and computer programs, mathematical models and suitable simulation tools were developed by Sangfors (1984), Singh and Onuschak (1984), Fujiwara et al. (1984) and Stosic et al. (1986). Further contributions by Singh and Onuschak (1984), Tang (1995), Hanjalic and Stosic (1997), Stosic and Hanjalic (1997) and Fleming et al. (1998) led to the ability to generate screw rotor profiles and accurately predicting overall screw compressor performance with ease on computers. The development of the “N” profile by Stosic (1996) turned out to be one of the best profiles for screw compressor rotors with distinguishing features such as rack generation, cycloidal curves on high-pressure sides of lobes and flexibility in control over curves and curve refinement (Stosic and Hanjalic, 1997).

Further gain in computer computational power led to the exploration of newer ways to optimize (Kauder et al., 2002) (Stosic et al., 2003) or generate screw rotor profiles based on previously untouched methods such as the use of bezier curves by Helpertz (2003), b-splines by Hauser et al. (2008), sealing line by Zaytsev and Ferreira (2005) and deviation function method by Huang (2015).

Improved manufacturing technologies combined with computer computational power lead to newer frontiers in the field. To mention a few, three-dimensional CFD (Computational Fluid Dynamics) of screw compressors by Kovacevic et al. (1999),

Kovacevic et al. (2002), Kovacevic et al. (2007), Kovacevic and Stosic (2013), Rane (2015), Basha et al. (2018) and Vasuthevan and Brümmer (2018) lead research in the field of CFD. The high-pressure applications of screw compressors by Hauser et al. (2016) and Vaidya (2019), internally geared screw compressors by Read et al. (2017), highly complex screw rotors by Gray et al. (2018), etc are the latest applications of screw machines.

1.4 Types of Screw Machines

According to different geometries and configurations of the rotors, the screw compressors can be classified by, the number of rotors: Single, Twin or multiple; rotor axis: Parallel or Non-parallel; rotor lead: Uniform or Variable; rotor profile: Uniform or Variable, relative motion: Intersecting or Non-intersecting; engagement: Planar, Cylindrical or Globoidal.

Twin-screw and single-screw rotor configurations are the two widely used screw rotor compressor configurations. Some other variants of the screw compressor listed above are also in commercial use, while the remaining configurations are under research.

1.4.1 Twin-rotor Screw Compressor

The most widely used configuration of the rotary screw compressor is the twin-screw compressor. A twin-screw compressor's construction is simple, comprising only a pair of meshing rotors which have helical grooves machined in them. These rotors are assembled in a casing that fits closely around them. A minimal clearance is maintained between the rotors and the casing. As the rotors rotate, they mesh like gears while the trapped volume between the rotors and the casing is progressively reduced. This reduction in volume causes the pressure of the trapped working fluid to rise.

The operating principle of the twin-screw compressor is explained with the help of Figure 1.7 and Figure 1.8.

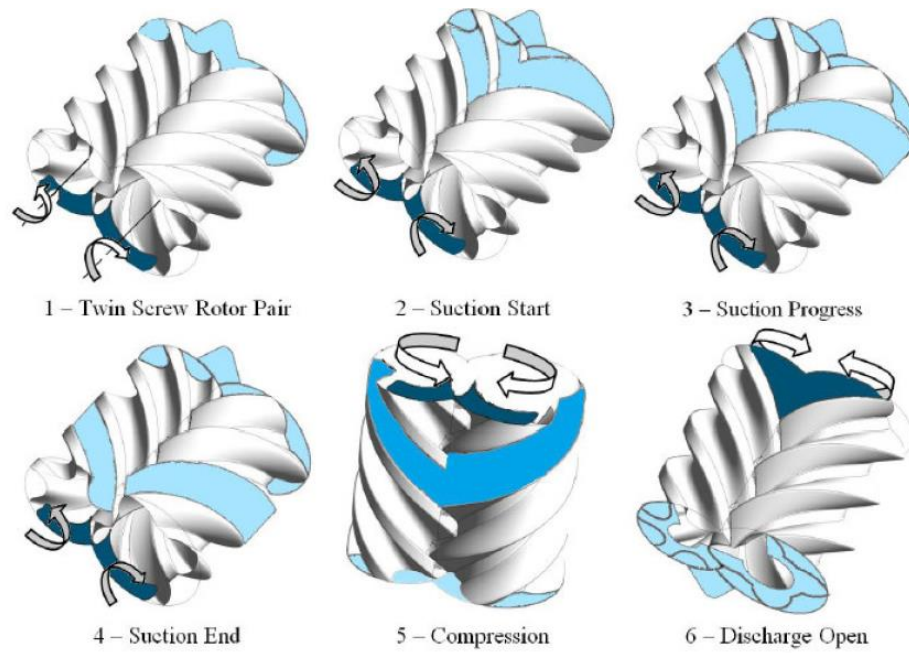


Figure 1.7: Working principle of a twin screw compressor (Rane, 2015)

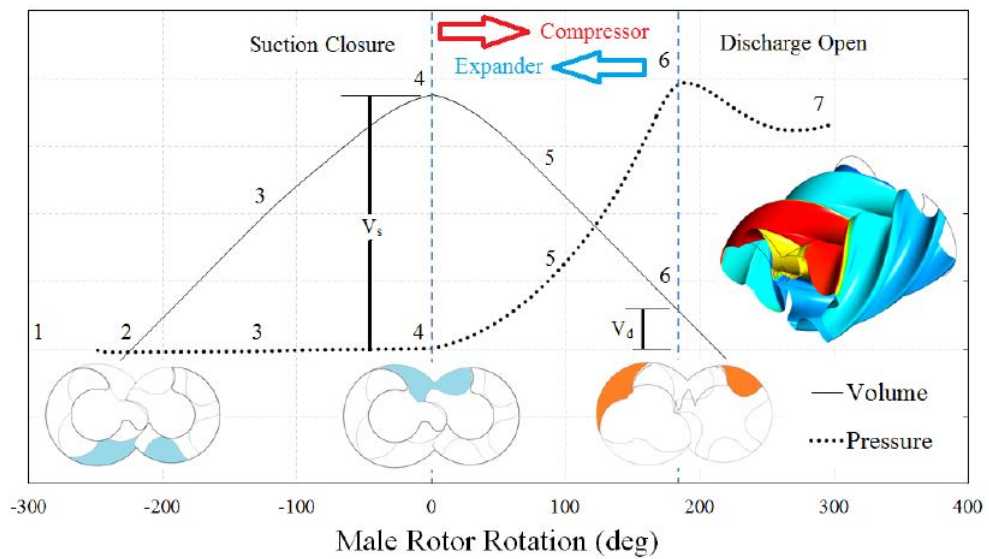


Figure 1.8: Typical pressure and volume variation in a twin screw compressor (Rane, 2015)

As the rotors rotate, the engagement of the lobes creates suction at one end of the rotor. Further rotation of the rotors draws more volume of the fluid into the working chamber. This is presented in Figure 1.7 and Figure 1.8 as a stage from 2 to 3. As the lobes of rotors pass the suction port, the gas gets trapped in between the rotors and the casing. At this point, suction ends and compression starts as shown in Figure 1.7 as stage 4 and indicated by point number 4 in Figure 1.8. The

volume of the gas trapped at point 4 is the maximum volume, V_s . As the rotation of rotors continues, the trapped volume of gas reduces, causing pressurisation of the gas till the lobes are exposed to the discharge port at the other end, as shown in Figure 1.7 as stage 6. The volume of gas discharged when the lobes are open to the discharge port is V_d . The ratio of suction volume to discharge volume, V_s/V_d , is called the built-in volume ratio, V_i . This process is repeated between successive lobes giving a continuous flow of pressurised gas. The compressed gas type determines the maximum pressure ratio developed by the compressor depending on the polytropic index of the gas.

1.4.2 Single-rotor Screw Compressor

Another type of screw rotor compressor which is used commercially is a single-rotor screw compressor. Unlike the twin-rotor screw, this configuration has a single screw rotor and was originated in 1962 by Zimmern and Patel. The geometry and components of the single-rotor screw compressor are shown in Figure 1.9 (Wu and Feng, 2008). Inside the single-rotor screw compressor, only a single-screw rotor is present, which meshes with two or more idler star-wheel rotors as shown in Figure 1.9. These star wheels are designed in the form of stars and envelop the lobes of the screw rotor. The star wheels are positioned so that their axes are perpendicular to the axis of the screw rotor.

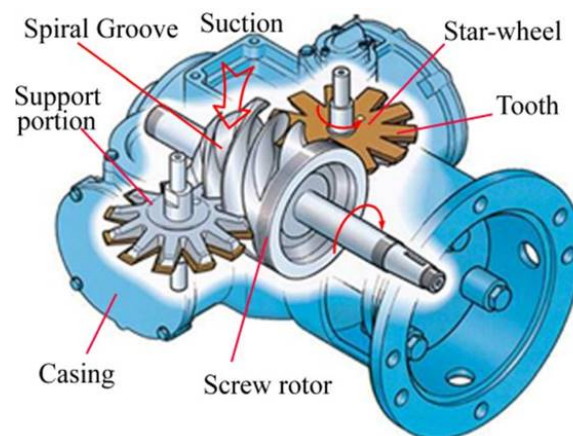


Figure 1.9: Geometry and basic components of a single-screw compressor (Wu and Feng, 2008)

The advantage of a single-rotor screw design is that the axial and radial loads

across the screw rotor are balanced between the high-pressure and low-pressure sides. This is achieved by recirculating leakage from the compression chamber to the suction through drilled holes. With the loads balanced between the high-pressure and low-pressure sides, the bearings' life can be considerably enhanced.

A few more geometries of single-rotor screw compressors are designed and under the research stage. To list a few; Planar Screw – Cylindrical Gate (PC type), Cylindrical Screw – Planar Gate (CP type), Planar Screw – Planar Gate (PP type) and Cylindrical Screw – Cylindrical Gate (CC type). The nomenclature is based on different configurations and relative axial arrangements of the male and female rotors.

1.4.3 Other Types of Screw Compressor

A few more variants of screw compressors are being researched for commercial use. They are described in detail below.

1.4.3.1 Variable Lead Twin Screw Compressor

The idea of screw rotors with variable lead was first proposed by Gardner (1969) in a patent. A twin-screw rotor pair with constant lead is shown in Figure 1.10 (a), whereas another set of the twin-screw rotor pair with the same diameter and length but with variable lead is presented in Figure 1.10 (b).

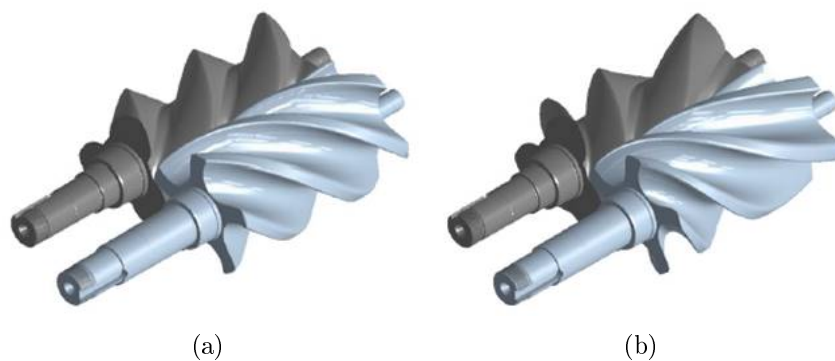


Figure 1.10: Meshing of twin-screw uniform and variable lead rotors (Kovacevic and Stosic, 2013)

For the same male rotor rotation angle, when compared with the conventional twin-screw (constant lead) compressor, the variable lead compressor can pressurise

the gas more. This increased built-in volume ratio makes them more suitable for high-pressure applications. Another advantage of this design is that the discharge port area near the end of the compression can be enlarged. This larger discharge port area reduces the leakage loss at the high-pressure discharge side. Additionally, the length of the sealing line can be shortened by varying the lead from the suction side to the discharge side. This shortening of the sealing line results in reduced leakage across the sealing line, thereby increasing the volume throughput.

On the contrary, with the increase in the overlap between rotors caused by a change in lead, the volume trapped between the rotors and the housing reduces. This reduces compressor delivery. Another challenge with the variable lead design is the manufacturing of the rotors. The available manufacturing processes are suitable for the constant lead, which cannot be readily used for manufacturing variable lead rotors which limits the use of these compressors.

1.4.3.2 Tri-rotor Screw Compressor

An increase in pressure difference across the rotor lobes increases the loads on the rotor. This increase in load reduces the reliability of screw compressors due to increased deflections. Different design philosophies are adopted to enable rotor design to take such high loads. One such philosophy is to increase the rotor diameter and the lobe combination. This increases the stiffness of the rotors, thereby reducing the rotor deflection. However, the disadvantage of such designs is that the gas chamber cross-section and, thus, the volume flow rate reduces.

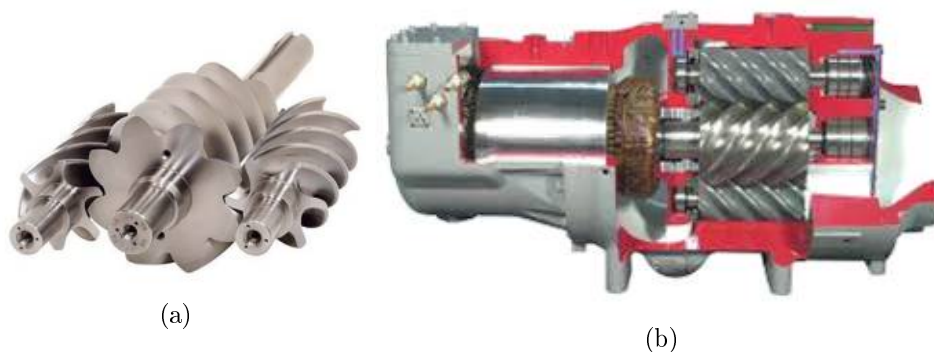


Figure 1.11: Tri rotor screw compressor (Jacobs, 2006)

One of the ways to increase this cross-sectional area is by increasing the number

of rotors. A single male rotor can drive two female rotors as shown in Figure 1.11 (Jacobs, 2006). This allows the reduced radial load on the male rotor because the suction and discharge occur at both ends of the male rotor. Although the number of female rotors in this configuration is twice that of a twin-screw rotor compressor, the displacement is not twice. Also, the female rotor's higher radial forces are not compensated like that of the male rotor. These reasons and the relatively larger size of the male rotor make this design of screw compressor less popular.

1.4.3.3 Internal Conical Rotary Screw Compressor

A configuration of the screw compressor, which is analogous to planetary gears, is developed by Vert-Rotors (Vert, 2021). The shape of rotors is designed in a conical helical shape, as shown in Figure 1.12.

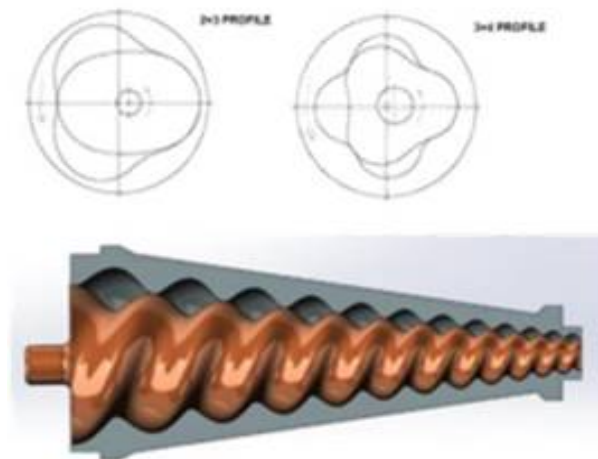


Figure 1.12: Conical screw profile (Vert, 2021)

Out of the two rotors of this compressor, one acts as an internal rotor while another acts as an external rotor. The configurations of the rotors shown in Figure 1.12 are $2/3$ and $3/4$. The first number indicates the number of lobes on the external rotor while the second number indicates the number of lobes on the internal rotor. This type of screw compressor achieves compression by a progressive reduction in the rotor diameters.

1.4.3.4 Internally Geared Parallel Rotor Machine

A configuration of the screw machine, which has straight lobes, is an internally geared parallel rotor machine. As the name indicates, it consists of inner and outer rotors whose axes are parallel. The inner rotor is geared externally while the outer rotor is geared internally, as shown in Figure 1.13. The continuous contact points between inner and outer rotors allow the formation of an enclosed chamber whose volume changes with respect to the rotation of rotors enabling compression or expansion. The compression or expansion is achieved by the positioning of the end plate(s) and port(s).

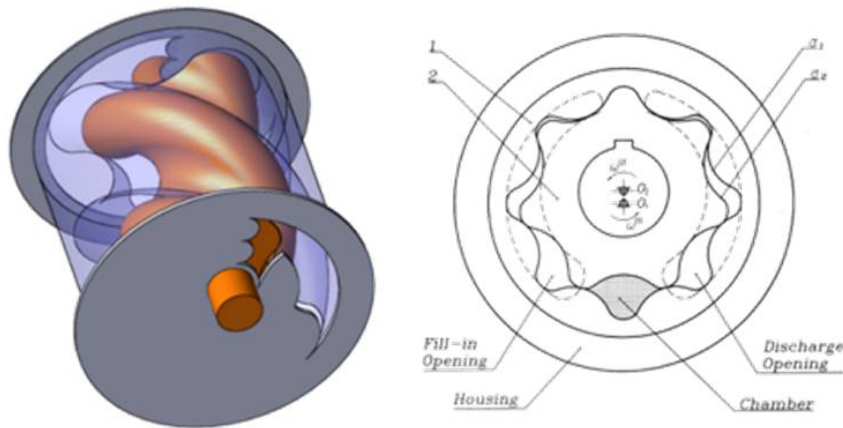


Figure 1.13: Internally geared parallel rotor machine (Read et al., 2017)

1.5 Air Screw Compressor System

Several types of screw compressors with their configuration, advantages and disadvantages have been presented in the previous section. All applications require not only the compressor but also a packaged unit of the compressor which will deliver the desired effect, compressed air or gas, to the end user. The packaged unit of an electric motor-driven oil-injected air screw compressor consists of two circuits; an air circuit and an oil circuit, as shown in Figure 1.14.

The atmospheric air is admitted into the system through an intake air filter, where dust and suspended particles get trapped to allow clean air to pass through. Before providing this admitted atmospheric air to the compressor, the intake valve, based on the application requirement, decides to load or unload the compressor.

Generally, this intake valve is a spring-operated and pneumatically controlled valve which opens and closes based on application requirements. When there is a demand for compressed air, the intake valve opens and loads the compressor, allowing atmospheric air to go to the compressor. On sensing no demand for the compressed air from the application, the control system commands the intake valve to close, thereby unloading the compressor.

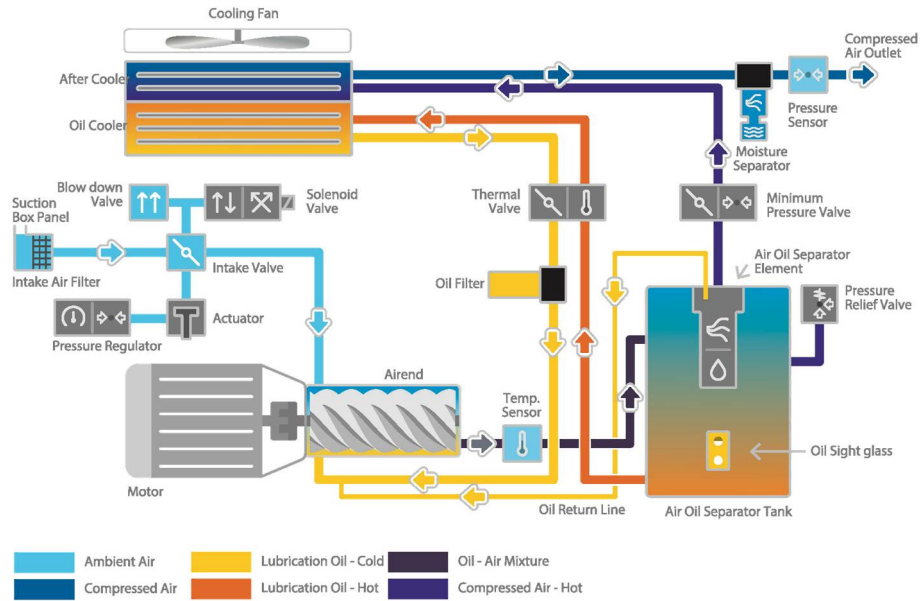


Figure 1.14: Schematic of air screw compressor package (Compressed-Air-Best-Practices, 2022)

Once the atmospheric air is admitted into the compressor because of the suction created by the rotation of the screw rotors, it gets compressed to a required pressure level within the compressor. The oil is injected into the compressor during the compression to achieve near-isothermal compression. Additionally, the injection of oil into the compressor benefits in lubricating the contact surfaces and sealing the clearance gaps. The discharge end of the compressor sees high-pressure, high-temperature air and oil mixture. This mixture after exiting from the compressor enters tangentially into the air-oil separator tank. Here, the oil gets separated from the air in two stages, dynamic, which utilises the cyclone effect and static which traps droplets which are not separated by the dynamic part. The separated oil settles down at the bottom of the tank on account of gravity. The suspended oil particles in the compressed air coming from the top of the air-oil separator tank are trapped in an

air-oil separator element at the top of the tank. This trapped and collected oil is scavenged back to the compressor from the separator element. A minimum pressure valve, MPV, situated at the top of the air-oil separator tank, acts as a relief valve allowing a certain pressure to build in the tank. In addition to returning oil to the compressor, the minimum pressure valve also helps in maintaining the required pressure across the separator element for effective separation of oil. Once this pressure inside the tank rises above a certain level, the MPV opens, and high-pressure air is passed through an after-cooler before it is made available to the application. This completes the airflow circuit of the oil-injected air screw compressor package.

The oil which is separated from the compressed air in the air-oil separator tank is passed to the oil cooler through a thermal valve. The pressure inside the tank drives the oil through the oil circuit and no additional pump is required. If the oil temperature is above a certain value, the thermal valve allows oil to go to the oil cooler, if not, it is recirculated back to the compressor without cooling. Finally, the oil is injected back into the compressor after filtration, completing the oil circuit.

1.6 Motivation to Investigate Screw Compressor System

This research is a part of the collaborative initiative involving Kirloskar Pneumatic Company Limited in Pune, India, and City, University of London in the UK. The core focus of this collaboration is the design, development, and rigorous testing of a family of oil-flooded, twin-screw air compressors. The results obtained from this study will serve as a validation framework for proposed power loss prediction methodologies, offering potential ways for optimizing the design of these compressors. While the preceding sections delve into the various categories of rotary screw machines and the intricate geometries inherent to screw compressors, it's noteworthy that the study's primary emphasis lies in the exploration and quantification of mechanical losses within twin-screw, oil-injected air compressors. Nevertheless, the insights obtained from this investigation hold promise for extending their applicability to other cited varieties of rotary screw machinery.

Given the structural similarities among crucial components—ranging from the rotating elements, encompassing screw rotors, lobes, or vanes, to the supporting

bearings; the lubrication mediums of oil or water, coupled with their associated drag losses; and the sealing mechanisms—slight tweaks in input variables and geometric parameters render the methods proposed in this study for calculating mechanical power loss adaptable to diverse screw machine iterations.

As projected by IMARC Group, a prominent global market analysis and research consultancy, the worldwide screw compressor market is poised to experience a Compound Annual Growth Rate (CAGR) of 5% from 2021 to 2026 (IMARC, 2021). Of notable significance, rotary air compressors are expected to command a substantial 60% of the overall market share (GMI, 2022). This distribution of the Rotary compressor segment in relation to alternative compression technologies, such as Centrifugal and Reciprocating, is visually represented in Figure 1.15.

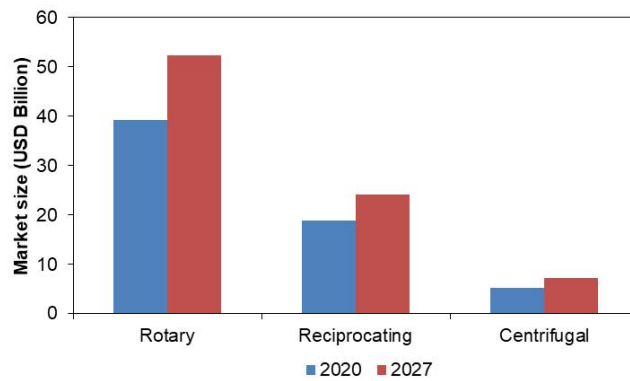


Figure 1.15: Global stationary air compressor market size, by Technology (GMI, 2022)

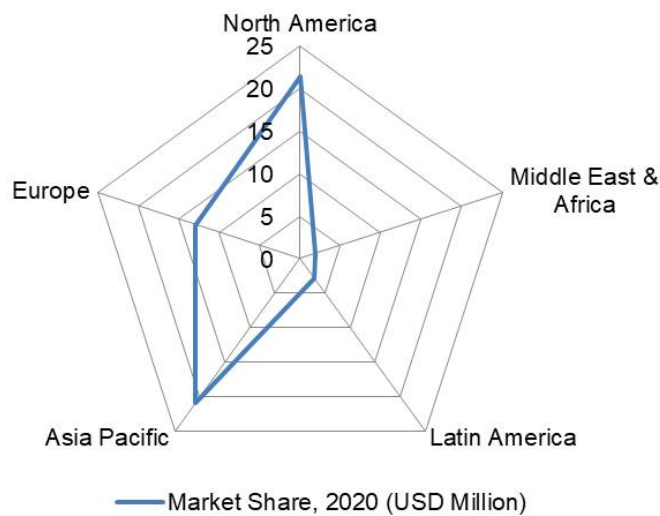


Figure 1.16: Global stationary air compressor market share, by Region (GMI, 2022)

The numbers presented in Figure 1.15 and Figure 1.16 are not indicated in the original reference, these are calculated based on certain measurements and are indicative. In parallel, the escalating demand for rotary compressors is anticipated to amplify industrial power consumption. In developed nations, compressors presently account for a significant 15-20% of total electricity consumption, intensifying the imperative to curb energy usage. To cater to the ongoing drive for enhanced energy efficiency, a pivotal focus revolves around minimizing specific power consumption—a metric defined as the power prerequisite for compressing a unit volume of delivered gas.

This objective can be achieved either by augmenting compressor flow delivery at a constant shaft power or by reducing shaft power requirements while maintaining consistent delivery. The volume displacement from the compressor is intrinsically tied to rotor dimensions, profiles, and their inherent attributes. Extensive prior research has centred on optimizing rotor profiles to achieve maximal flow with minimal leakages and reduced contact forces. However, in the pursuit of further minimizing shaft power consumption, a necessary step involves addressing losses within the compressor. Since adiabatic shaft power hinges on gas properties, volume flow rate, and compression ratio, identification and quantification of power loss-contributing elements within the compressor assume pivotal importance, offering a strategic viewpoint for potential enhancements.

Chapter 2

Literature Review

2.1 Introduction

The oil-flooded screw compressors can attain very high isothermal efficiency because of the cooling effect of oil circulation. However, mainly because the flow through them is not axisymmetric, bearing loads within them, because of higher pressure forces, are much larger than in turbo-compressors, and these, together with oil drag, and shaft seal losses, can reduce their overall efficiency. A better understanding of the sources of loss and an improved ability to predict them is essential if these relatively significant losses are to be minimised. A Sankey diagram representing elements of power in a screw compressor package is shown in Figure 2.1.

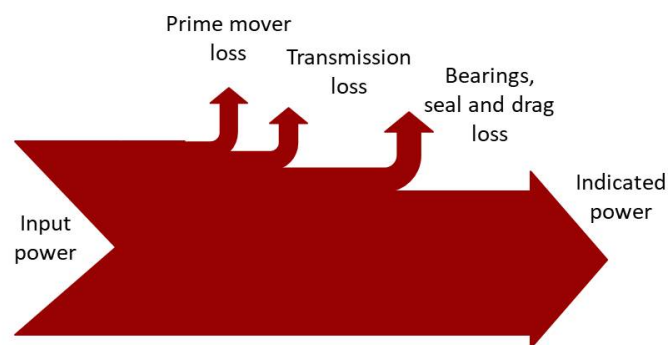


Figure 2.1: Sankey diagram of power

As seen from the figure, only a part of the total input power to the screw compressor package is available for compression. The remaining part is lost in overcoming prime mover, transmission, bearing, seal, and oil drag losses.

Currently, although adiabatic power input, efficiencies and the magnitude of the bearing loads can be predicted very accurately, there are no established methods to predict frictional losses. These are usually accounted for, assuming they are some percentage of the total input power. The components of the electrically driven air screw compressor plant which contribute to the mechanical losses are the electric motor, the power transmission drive-like gears and the bare compressor. Within the bare screw compressor, components that contribute to power loss are rolling element bearings, seals and drag loss caused by lubricating oil. A cross-section of the bare screw compressor is shown in Figure 2.2.

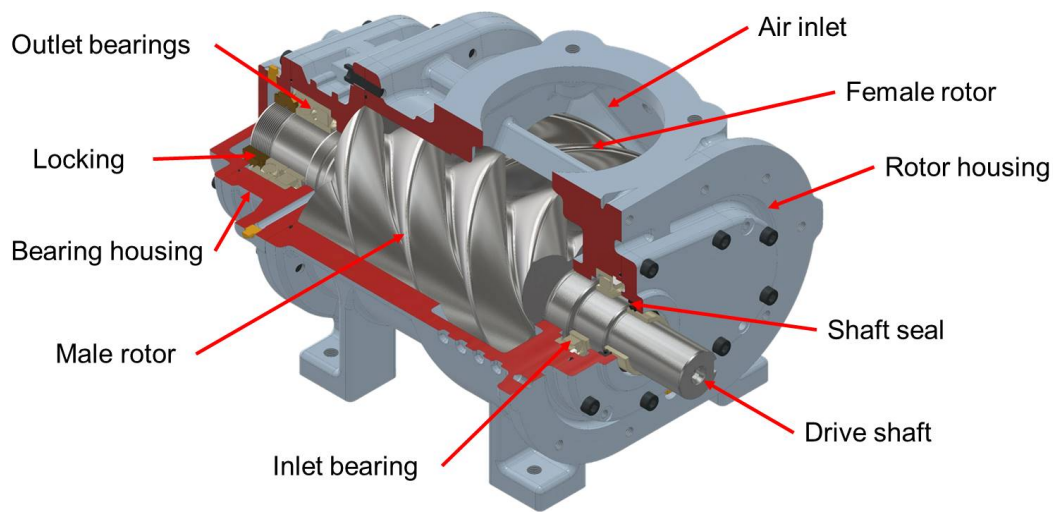


Figure 2.2: A cross-section of the bare screw compressor of Kirloskar Pneumatic Company Limited

Individual literature studies are available that present power loss prediction methods for electric motors, gears, bearings, seals, and oil drag. A few of the literature on power loss prediction is presented here. A basic model for calculating power loss through different types of losses within the induction motor is presented in Hughes and Drury (2019). Mehlretter (2014), El-Ibiary (2003), Sirov y et al. (2011) and Bell et al. (2020) have presented performance prediction and power loss of an induction motor, the control philosophy to achieve the best efficiency from the motor and optimization of variable speed drives etc. The details of the methods presented in the literature are discussed in this chapter.

The physical phenomenon happening inside the screw compressor, the basics of compression in screw compressor and its design is reported in books published by

Sakun (1960), Rinder (1979), Xing (2000), O’Neill (1993) and Stosic et al. (2005). Numerical simulation models like SCORPATH (Screw COmpressor Rotor Profiling And THERmodynamics) developed by City, University of London researchers is presented in Stosic (2005) and PDSim, a simulation model for positive displacement machines, is presented by Ziviani et al. (2020). These models are studied to understand the loss prediction methods. These simulation frameworks predict thermodynamic performance by solving governing equations and calculate the mechanical efficiency of the compressor at different operating conditions.

A few popular rolling element bearing power loss prediction models like SKF (2018) and Harris and Kotzalas (2007) are studied, while studies by Tu (2016) and Gradu (2000) provide the experimental measurement of bearing power loss which can be used for validation of SKF, Harris and Palmgren bearing power loss prediction models.

For the calculation of shaft seal power loss, a combination of finite element approach and empirical correlation is proposed by Frölich et al. (2014) is studied while Engelke (2011) presented experimental measurements of frictional torque for different elastomer material shaft seals.

Limited literature is available for calculating and predicting drag loss arising from lubricating oil. Deipenwisch and Kauder (1999), Gräßer and Brümmer (2014), Gräßer and Brümmer (2015) and Gräßer and Brümmer (2016) are a few literature that presents and analyses the effect of lubricant and its properties on the performance of screw compressor as well as screw expander.

The details of the literature sources cited above, and a few more are discussed in detail in the next section to understand the principles on which these models have been developed.

2.2 Screw Compressor

2.2.1 Twin-rotor Screw Compressor Geometry

As detailed in Section 1.4.1, the twin-rotor screw compressor incorporates a pair of screw rotors, each featuring helical grooves meticulously machined into them. These

rotors align in parallel axes and engage with one another through opposing rotations within the compressor housing. This meshing action produces low pressure at one end of the compressor and high pressure at the opposite end. These pressure differentials impose significant axial and radial forces, necessitating their transmission to the housing via bearings. Generally, rolling element bearings are favoured for smaller to medium-sized compressors, whereas journal bearings are tailored for larger counterparts. In rolling element bearing set-ups, cylindrical or tapered roller bearings are strategically positioned on both the suction and discharge sides to manage radial loads. To address axial loads, ball bearings are predominantly situated on the discharge side.

The pursuit of nearly isothermal compression, integral for cooling the primary or operational fluid, introduces a secondary or cooling fluid during compression. This fluid injection-based classification system differentiates screw compressors into two categories:

- Fluid-injected compressors
- Dry running compressors

In fluid-injected compressors, a secondary fluid is introduced into the rotor cavities during compression. This injection serves multiple purposes, including sealing the gaps between the rotors, absorbing compression-generated heat from the gas, lubricating rotor contacts, and preventing corrosion. The secondary fluid, which could be oil, refrigerant, or water, mixes with the primary fluid during compression and is subsequently separated downstream using various techniques. The high-temperature separated secondary fluid is then recirculated within a closed loop, re-entering the compressor post-cooling and filtration.

Typically, fluid-injected screw compressors operate within a range of rotor tip speeds from 25-60 m/s, while single-stage compressor discharge pressures vary from 7 to 13 bar, and up to 25 bar for two-stage compressors. For water-injected screw compressors, corrosion-preventive coatings are applied to the rotors, and meticulous sealing is employed between the bearings and the compression chamber to prevent leaks. Refrigerant-cooled compressors can adopt similar layouts to either oil-injected or water-injected screw compressors.

Conversely, dry running compressors avert rotor contact to prevent additional heating in the absence of cooling fluid. This is achieved through the integration of timing gears on extended rotor shafts, ensuring precise coordination between the rotors. The lubricated timing gears and bearings are sealed off from the compression chamber. Due to elevated operating temperatures, clearances in dry running compressors are intentionally maintained larger compared to fluid-injected counterparts. This strategy anticipates contact between rotating parts, which may expand due to thermal effects. To counteract increased leakages arising from larger clearances, these compressors operate at higher tip speeds, typically surpassing 70 m/s. Multi-stage compression is used to control discharge temperatures until a pressure range of 7 to 10 bar is reached.

2.2.2 Screw Compressor Mathematical Models

The performance of the screw compressor is governed by the effects of thermodynamic and fluid flow processes, and the machine geometry. These interactive effects need to be calculated simultaneously to predict performance. A mathematical model of the thermodynamic and fluid flow processes within positive displacement machines, which is valid for both the screw compressor and expander modes of operation, is presented in Stosic et al. (2005). It includes the use of the equations of conservation of mass, momentum, and energy. An instantaneous control volume is defined to which these conservation equations are simultaneously solved. While solving these equations for the trapped fluid control volume, considerations are given to primary and secondary fluid leakages, heat transfer and the assumption of real fluid properties. From this calculation, the pressure-volume diagrams may be derived from the entire admission, discharge and compression or expansion process within the machine.

A screw machine volume is defined by the rotor profile which is generated by the use of a general gearing algorithm and the port shape and size. This algorithm demonstrates the meshing condition which, when solved explicitly, enables a variety of rotor primary arcs to be defined either analytically or by discrete point curves. Its use greatly simplifies the design since only primary arcs need to be specified and these can be located on either the male or female rotor or even on any other rotor

including a rack, which is a rotor of infinite radius. The most efficient profiles have been obtained from a combined rotor-rack generation procedure (Stosic et al., 2005).

Stošić et al. (1992) in their study has investigated the influence of oil injection upon the screw compressor working process. The influence of oil injection temperature, oil injection diameter, mass flow, and position has been experimentally recorded. The study concludes that the influence of oil injection temperature and its positioning has a considerable effect on specific power consumption. However, the oil-to-gas mass ratio and viscosity have a small influence on the performance.

A paper by Hanjalic and Stosic (1997) presents the development of a computer package which facilitates the general specification of key parameters of rotors. This is used for the computation of cross-sectional area and volume for the prediction of thermodynamic performance and design optimisation.

A book published on mathematical modelling and performance calculation by Stosic et al. (2005) is focused on contemporary methods for the design of screw compressors. The methods given for rotor profiling are based on the mathematical theory of gearing. The model assumes real properties of fluid that provide more reliable and realistic predictions which include the computer-simulated compression and expansion processes by allowing leakages.

Ziviani et al. (2020) presents the methods based on which PDSim, a performance simulation tool for positive displacement machines, is developed. This open-source numerical model solves governing equations for calculating volume curves, leakage flow, heat transfer and frictional losses of different types of positive displacement compressors and expanders.

Chukanova (2016) in her PhD thesis, presented a one-dimensional mathematical model which predicts screw compressor package performance under intermittent operating conditions and its experimental validation. The unsteady operation of the plant and its effect on components, such as storage tanks, control valves, and connecting pipes, have been studied. This includes the effect of sudden changes in pressure, speed, and valve area. The model developed is compatible with oil-injected as well as oil-free screw compressors.

2.2.3 Bearing Power Loss

There are several mathematical models available to estimate a rolling element bearing's frictional power loss. The most commonly used among them are SKF, Harris, and Palmgren models. These three models are studied in this section, and predictions of these methods are compared.

2.2.3.1 SKF model

The SKF model (SKF, 2018) consists of four elements: rolling frictional moment, sliding frictional moment, the frictional moment from seal/s and frictional moment from drag losses, churning and splashing.

The rolling frictional moment considers the effect of oil shearing at the inlet of the rolling element, the kinematic replenishment/starvation, bearing type, dimensions and loads acting on it, and the actual operating viscosity of oil or the base oil of the grease while calculating the frictional moment. In the case of sliding frictional moment, it is dependent on bearing type, geometry, the loads and the sliding friction coefficient. The drag loss element of SKF's model is a function of bearing speed, oil viscosity, oil level and bearing size.

2.2.3.2 Harris model

In Harris model (Harris and Kotzalas, 2007), the friction torque is separated into a component due to applied load and a component due to the viscous properties of the lubricant. The viscous properties depend upon the lubricant type and the amount of lubricant employed. The properties of lubricant in the rolling element raceway contacts contribute significantly to the applied load component of friction torque. The methods presented by Palmgren and Harris are useful for comparison between rolling bearings and fluid film bearings.

2.2.3.3 Palmgren model

Similar to the Harris model, the Palmgren model (Tu, 2016) divides frictional torque into two parts, load-independent friction torque, and load-dependent friction torque. However, Palmgren proposed a more detailed model for load-independent friction

torque for oils of different densities.

2.2.3.4 Comparison of SKF, Harris and Palmgren model

Different studies have presented different ways for the calculation of bearing friction loss. A few such ways are the use of one friction coefficient factor, the use of existing methods like Palmgren, Harris, and SKF, etc., or correlations developed by experimental fitting. A comparison between the SKF, Harris, and Palmgren models with experimental results available in the literature is presented in this section. This analysis helps for better prediction of bearing frictional loss by selecting an appropriate model for a given operating condition. Firstly, the frictional loss of a cylindrical roller bearing is studied followed by an angular contact ball bearing. This is done by comparing model predictions with the experimental measurements presented in the literature.

Roller bearing

Tu (2016) as a Master of Science study worked on different power loss prediction models of bearings used in a gearbox. The loads on the gearbox bearing under test were between 0.6 to 9 kN, speeds up to 3500 rpm, and oil temperatures ranging from 30 to 120°C. The bearing that was studied for the prediction of power loss is NJ 406 which is a cylindrical roller bearing.

One of the objectives of the study was to accurately and repeatedly predict the NJ 406 bearing power loss which is used in the back-to-back arrangement. The gearbox setup was modified by assembling a housing, lever, and known weights to simulate different load conditions on the bearings. Three existing bearing power loss prediction models, Palmgren, Harris, and SKF, were studied. The experimental measurements were done for NJ 406 bearing power loss for different rotating speeds, loads, oil levels, oil types, and oil temperatures. These were then compared with the predictions from above mentioned three models.

Load-independent losses: The load-independent losses are the losses because of lubricant and lubricant properties. A comparison between experimental data and existing model predictions for load-independent friction torque with changing oil

temperature and speed is presented in Figure 2.3.

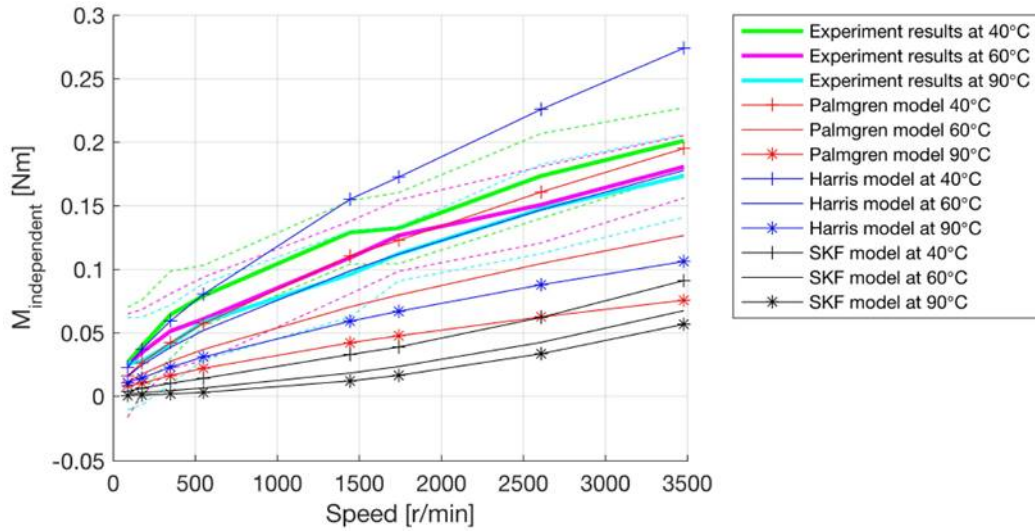


Figure 2.3: Effect of oil temperature on load independent friction torque (Tu, 2016)

The Harris model predictions are higher than SKF and Palmgren models at all temperature and speed limits as shown in Figure 2.3. The experimental observations are within the limits of predictions from the Harris model, while SKF and Palmgren models are less sensitive. The effect of oil level and speed on load-independent friction torque is shown in Figure 2.4.

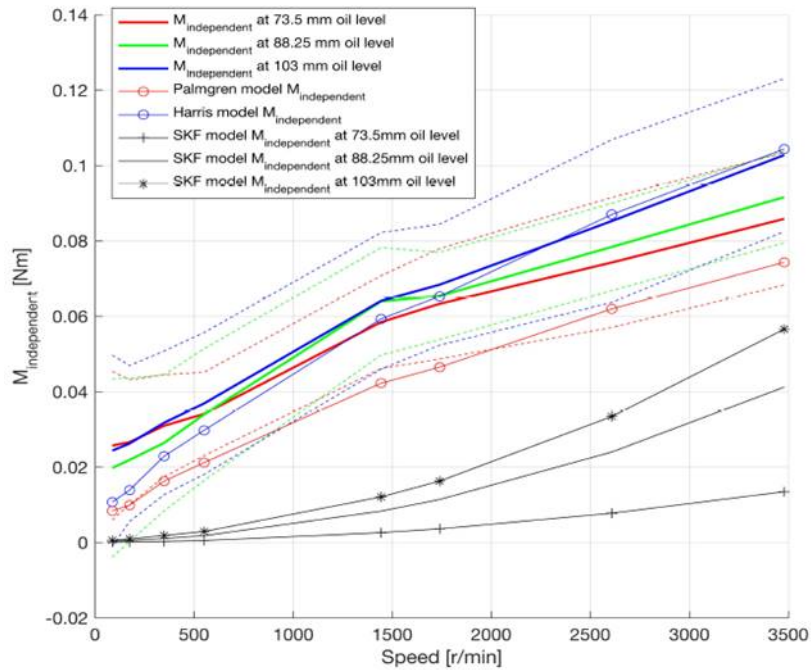


Figure 2.4: Effect of oil level on load independent friction torque (Tu, 2016)

Although the predictions from the Harris models are high, the experimental values closely match Harris model predictions. However, the effect of oil level change can be noticed only in the SKF model. When different oil types are used, the load-independent friction torque will change due to changes in oil viscosities. This is presented in Figure 2.5.

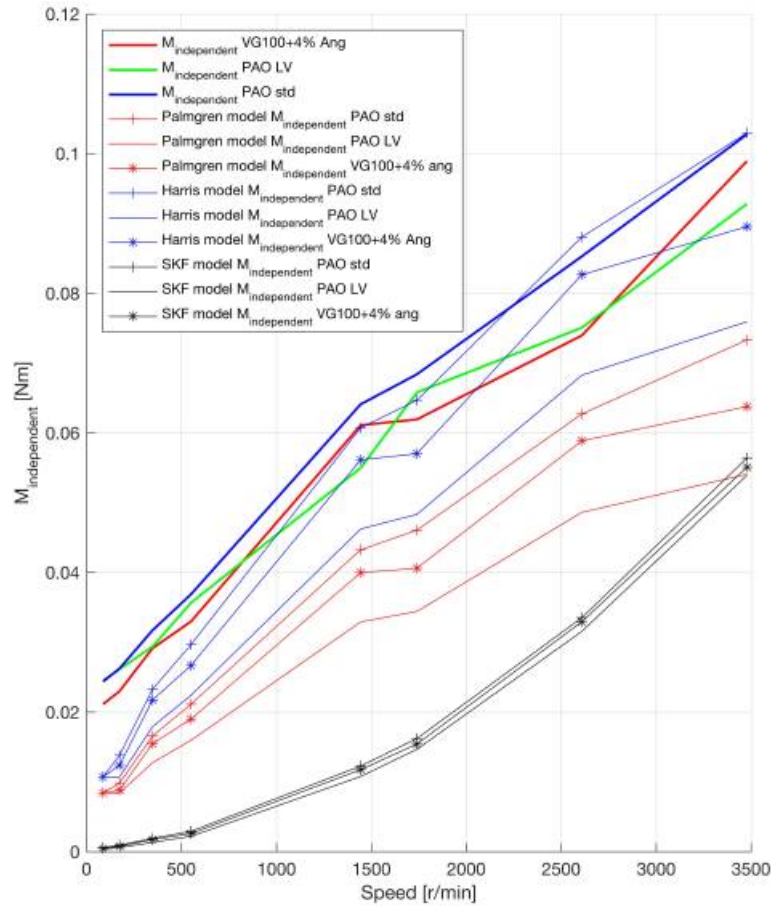


Figure 2.5: Effect of oil type on load independent friction torque (Tu, 2016)

In line with the effect of oil temperature and oil level, the load-independent friction torque for oil types is well predicted by the Harris model, which is close to experimental data. Palmgren and SKF models underpredict the friction torque when compared to experimental data.

Load-dependent losses: Similar to load-independent frictional loss analysis as presented in the previous section, this section presents an estimation of load-dependent frictional torque from the Harris, Palmgren, and SKF models along with their comparison with experimental results. The experimental data and predictions from the models for load-dependent friction torque at different oil levels are presented in Fig-

ure 2.6.

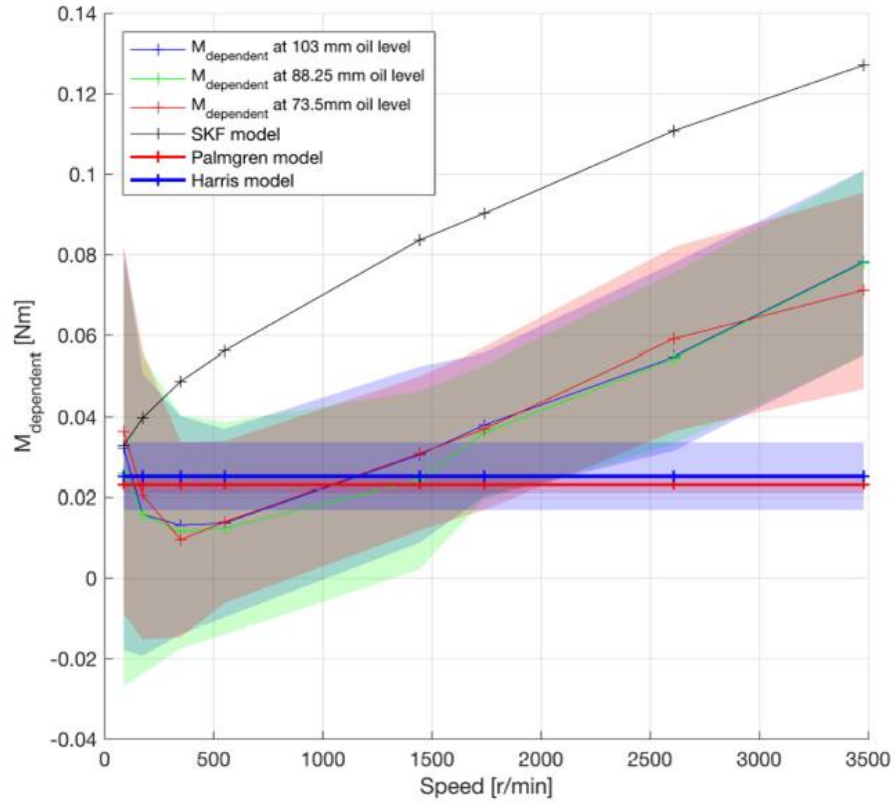


Figure 2.6: Effect of oil level on load-dependent friction torque (Tu, 2016)

None of the models shows a change in load-dependent friction torque with respect to changes in oil level. The SKF model overpredicts the friction torque while Harris and Palmgren models underpredict. However, the experimental data for friction torque at low bearing speeds match Harris and Palmgren's model predictions.

Similar behaviour for load-dependent friction torque for different oil types is presented in Figure 2.7. The only change can be seen in the predictions of the SKF model, where, with the change in oil type and, ultimately, oil viscosity, the predictions vary. However, the predictions of the SKF model are still on the higher side compared to the experimental measurements and predictions from Harris and Palmgren models.

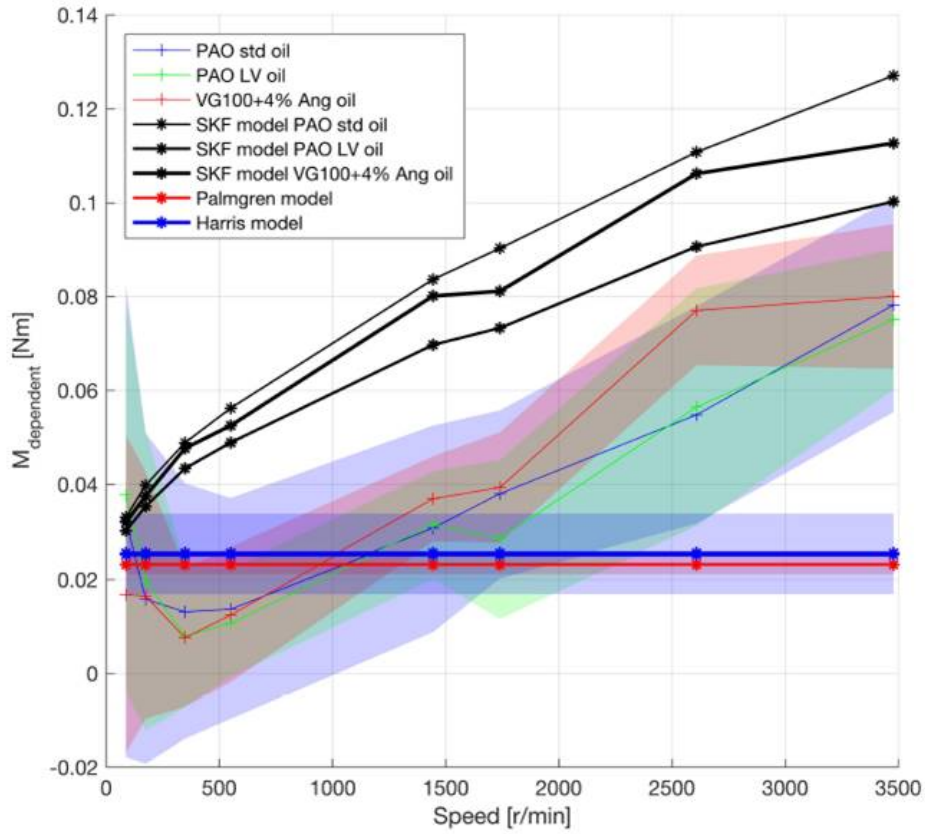


Figure 2.7: Effect of oil type on load-dependent friction torque (Tu, 2016)

Although Harris and Palmgren's models underpredict the friction torque for higher speeds, the predictions at lower bearing speeds can be seen closely matching experimental results.

The load-dependent friction torque should change with varying loads, and the same has been presented in Figure 2.8. The experimental measurements have been compared with SKF, Harris, and Palmgren models for different bearing loads and speeds.

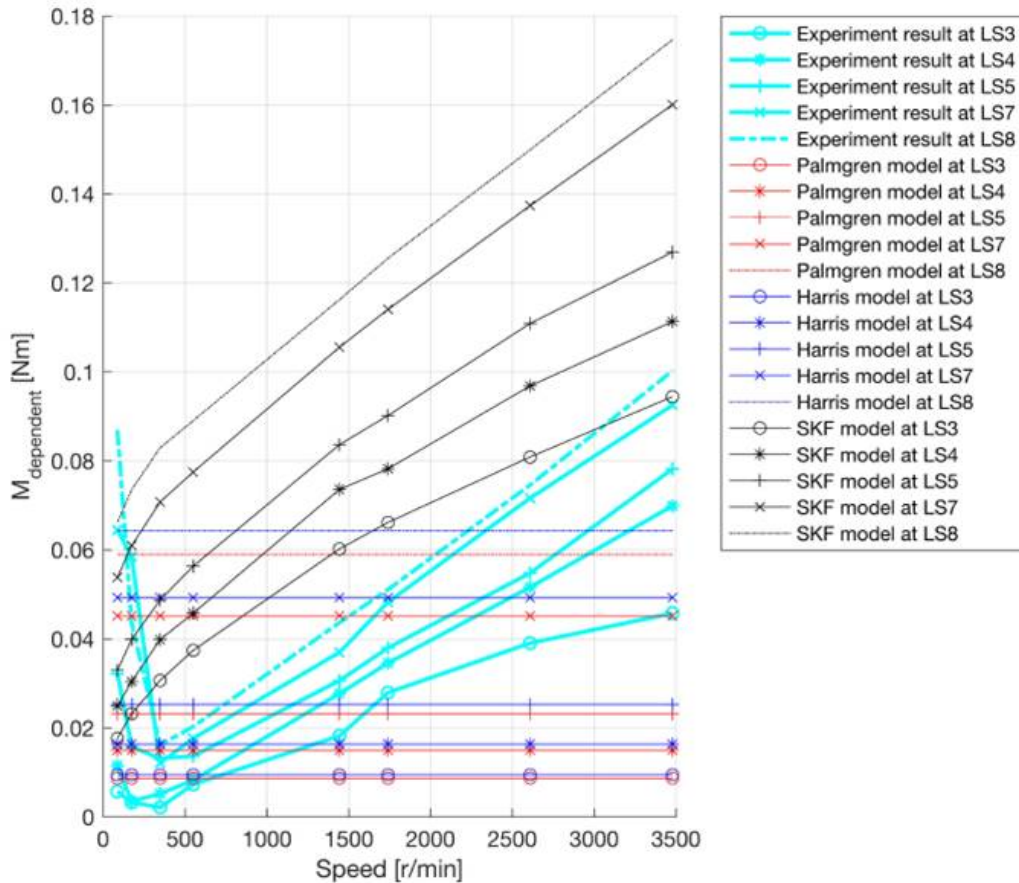


Figure 2.8: Effect of different loads on load-dependent friction torque (Tu, 2016)

Though the SKF model predictions follow the experimental data, it slightly over-predicts. In the case of the Harris and Palmgren models, the predictions change with varying loads but do not show any change with respect to bearing speeds. Harris and Palmgren’s model predictions are closer to the experimental results at lower bearing speeds.

Ball bearing

This section presents an analysis of the model predictions of total frictional torque for ball bearings and a comparison with the experimental results. Gradu (2000) presented an experimental evaluation of frictional torque for ball bearings used for transmission shaft.

The bearing used for analysis is 7305, an angular contact ball bearing. Generally, this type of bearing is used in a twin screw compressor to take the axial load. Two cases are analysed by Gradu (2000) with different transmission torques. For Case 1,

where the transfer shaft is transmitting a torque of 100 Nm, the radial load acting on the floating bearing is 3500 N, the axial load is 1000 N, and for the fixed bearing, the radial load is 4250 N, and the axial load is 3500 N. For Case 2, where the torque transmission is 200 Nm, the floating bearing experiences a radial load of 7000 N with an axial load of 2000 N, while the fixed bearing experiences a radial load of 8500 N and an axial load of 7000 N. Total frictional torque is the summation of individual frictional torques of floating and fixed bearings. The oil viscosity considered for calculation is $38 \text{ mm}^2/\text{s}$. The experimental observations presented by Gradu (2000) are shown in Figure 2.9 while the SKF and Harris models predictions for the same bearing and operating conditions are presented in Figure 2.10.

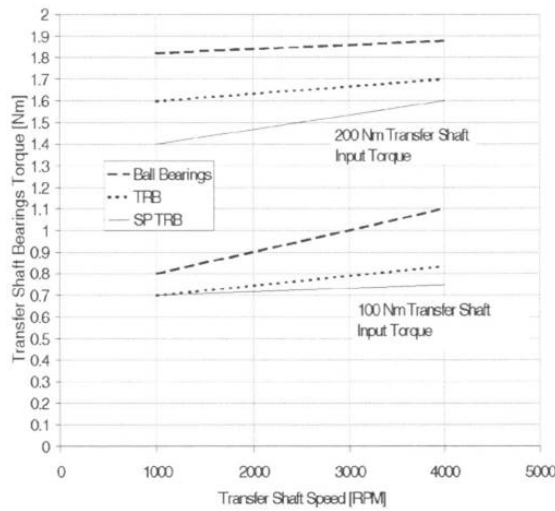


Figure 2.9: Frictional torque of ball bearing from experimental data at different loads (Gradu, 2000)

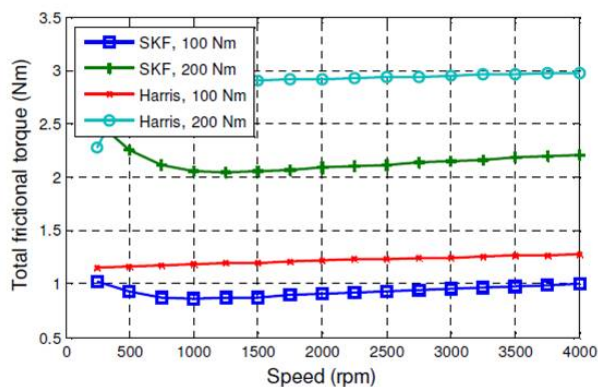


Figure 2.10: Frictional torque of ball bearing from the output of existing models at different loads

Upon comparison of ball bearings results at low torque application, 100 Nm, both SKF and Harris models predictions are closer to the experimental data. At higher torque, 200 Nm, SKF, and Harris models slightly overpredict the friction torque than the experimental results.

2.2.3.5 PDSim bearing model

A bearing's frictional loss prediction model developed by researchers at Purdue University is studied. PDSim is a generalised modelling platform to predict the performance of positive displacement compressors and expanders. The researchers proposed the possibility of predicting the mechanical efficiency of the positive displacement machines. The method considered for predicting the mechanical loss in PDSim is shown in Figure 2.11.

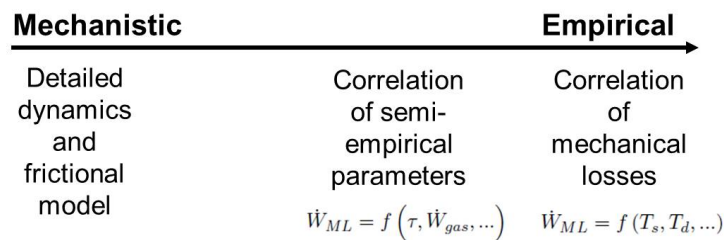


Figure 2.11: PDSim Bearing frictional loss methods (Bell et al., 2020)

It is presented in the paper by Bell et al. (2020) about the possibility of using the empirical relationship to correlate mechanical power to gas compression power. The relationship is given in Liu et al. (2010), which is based on the available experimental results. The difference between the shaft power prediction by the model without any consideration of the mechanical losses and heat transfer and experimentally measured shaft power is assumed to be the mechanical loss.

The same paper presents a section on frictional losses of the bearings. The families of the bearings considered are journal bearings and slider bearings. The schematics of the journal and slider bearing are shown in Figure 2.12.

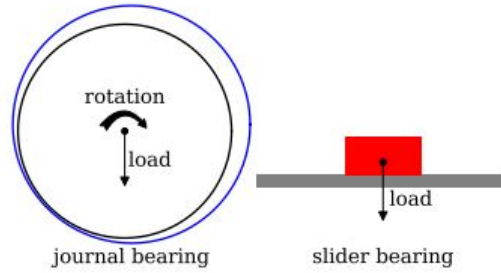


Figure 2.12: Schematics of journal and slider bearings (Bell et al., 2020)

The paper presents different methods of prediction of bearing frictional loss. One of them is by using Reynold’s equation and solving it numerically. The other methods include approximation methods suggested by Hamrock et al. (2004), Schiffmann (2014), numerical solutions suggested by Raimondi and Boyd (1958) and analytical solution by Sommerfeld given in Hamrock et al. (2004).

2.2.4 Radial Shaft Seal Power Loss

The radial shaft seal forms an integral part of the screw compressors, which prevents oil leakage from the compressors. As the lip of the stationary seal tightly sits on the rotating shaft, it creates friction and ultimately power loss. A very thin film of lubricant separates the shaft seal ring and the shaft. The temperature at the contact area between the shaft and the shaft seal rises because of the shear strain and fluid friction. This contact temperature changes the stiffness of the seal material which in turn affects the contact pressure, friction, and wear.

To predict this combined behaviour of contact temperature, friction, and wear, a comprehensive simulation model is developed by Frölich et al. (2014). The authors have developed a finite element approach for the simulation of contact pressure at different wear states. For the calculation of contact temperature, a semi-analytical approach is developed while an empirical approach is used for the determination of friction. Experiments were carried out to validate the friction torque predictions from the model. Frölich et al. (2014) have set up a parametric axisymmetric finite element model using the ABAQUS Python scripting interface. Until the required wear state of the seal is reached, the calculations are iterated with time increments. Three simulation steps are performed for each time step. In the first step, the

mechanical geometry of the shaft seal and the shaft is updated using ALE Adaptive Mesh Constraint by moving contact nodes in the direction of the contact normal. Additional boundary conditions at the outer nodes of the seal ring and inner nodes of the shaft are updated. The second simulation step is a coupled temperature-displacement step. The temperature distribution in the seal ring and the shaft is determined. In the third and last step of the simulation, the assembly of the shaft and seal are simulated from which the contact pressure distribution is calculated. These steps are followed for each time step.

The contact temperature which strongly influences the elastic properties of the shaft seal is calculated using an empirical approach which is based on a large number of experiments. The friction torque is constituted of a non-viscous fraction at zero speed and a velocity-dependent fraction.

$$T = T_0 + T_\eta = \mu_0 F_r \frac{d}{2} + \eta(\nu) \frac{b}{\Sigma R_p} \left(\frac{d}{2}\right)^3 \frac{(2\pi)^2}{60} n \quad (2.1)$$

Here, T is the total friction torque, T_0 is the initial friction torque, T_η is the viscous part of the friction torque, μ_0 is the boundary friction coefficient, F_r is the radial force, d is the shaft diameter, η is the dynamic fluid film viscosity, ν is the contact temperature, b is the contact width, ΣR_p is the sum of the surface roughness R_p of the shaft and seal lip, and n is the rotational speed of the shaft.

In a PhD study by Engelke (2011), the influence of elastomer-lubricant combinations on the operating performance of radial shaft seals is studied. The experiments were carried out to understand the effects of oil viscosity, radial contact force, and the seal material. Based on the experimental measurements, a calculation model is developed to predict the shaft seal friction torque which is the sum of friction moment and viscous component.

The total shaft seal friction torque (M_{total}) can be determined by

$$M_{total} = M_0 + M_\eta \quad (2.2)$$

M_0 is defined as the product of the limit coefficient of friction (μ_0), the radial force

(F_{rad}) and the test shaft radius (r_a).

$$M_0 = \mu_0 \cdot F_{rad} \cdot r_a \quad (2.3)$$

The speed-dependent friction torque (M_η) can be determined by

$$M_\eta = \tau \cdot A \cdot r_a = \frac{\eta(\theta) \cdot b \cdot r_a \cdot 2 \cdot \pi}{h} \cdot r_a \cdot \Delta v \quad (2.4)$$

The radial force acting on the seal lip can be calculated using the following equation.

$$Fr = Fr_{mean} \pi d \quad (2.5)$$

here, Fr is the radial force [N], Fr_{mean} is the mean relative radial force [N/m], d is the shaft diameter [m]. The experimental measurements for radial forces for different seal materials are presented in Table 2.1 (Engelke, 2011).

Table 2.1: Relative radial shaft seal force for different materials

Measurement at nominal diameter 60 mm	FKM-A	FKM-B	FKM-X	NBR
Relative radial force with spring [N/m]	118.3	75	103.5	145.9
Relative radial force without spring [N/m]	57.3	50.4	56.8	74.9

The oil dynamic viscosity which is a function of oil temperature can be derived using the following equation.

$$\eta = Ae^{B/(T_{oil}-C)} \quad (2.6)$$

where, A, B and C are constants defined respectively for different viscosity grades of oil (Knežević et al., 2006).

The total friction torque can be calculated using Equation 2.1. Out of a few input variables, the values of shaft diameter, speed, and surface roughness are known while the relative radial force can be selected from Table 2.1. The seal width can be determined by the digital microscope while the unknown coefficient of friction can be empirically determined. The assumptions on the sealing contact temperature and

coefficient of friction can be made based on experimental data.

A stepwise calculation of the shaft seal power loss in a flowchart is presented in Figure 2.13 (Engelke, 2011).

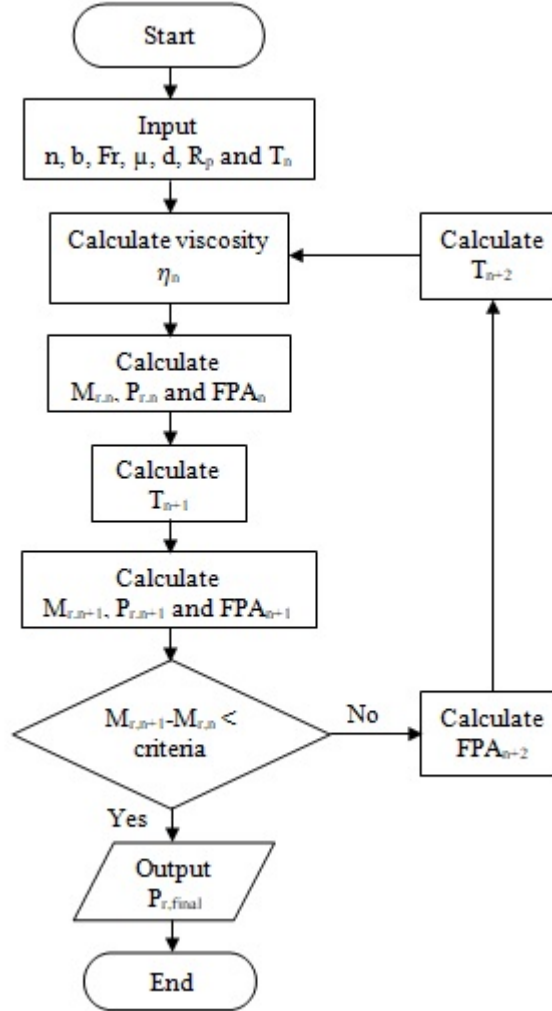


Figure 2.13: Flow chart of iteration for seal frictional moment calculation

As can be seen from the flowchart, it is an iterative procedure. The values of friction coefficient, the radial force on the seal, seal-shaft contact surface width, shaft diameter, shaft surface roughness, and rotating speed are used as input parameters. As a good approximation, the value of friction coefficient can be considered as 0.30 for a wide range of oils and elastomers (Frölich et al., 2014).

With an assumption of contact temperature, ϑ , the initial value of frictional torque is calculated. For the next time step, this contact temperature is raised by 16 K for 1 W/mm² sealing contact area. This value is experimentally validated by Engelke (2011). Upon calculation of the next time step friction torque with an

updated value of contact temperature and oil viscosity for it, the difference between the two latest friction torque values is calculated. This value is then compared with the convergence criteria, which can be of the order of 1×10^{-5} .

Engelke (2011) used a seal of $60 \times 75 \times 8$ mm size during the testing. Different types of seal materials; FKM-A, FKM-B, NBR, and FKM-X; from different manufacturers were used for the testing. Five different types of oil, two polyalphaolefins (PAO), and three polyglycols (PG) are used with a viscosity grade of ISO VG 220. A test facility with a force sensor, a mandrel and a ring holder was developed for the measurement of radial force.

It is observed that with the increase in temperature, the radial force on the seal decreases for almost all seal types that were analysed. The FKM material seals exhibit lower radial forces as compared to the NBR material seals. Polyglycol-based oils generate temperatures and frictional moments slightly higher than polyalphaolefin-based oils. The base oil composition and the additives have only a slight influence on the temperature and friction torque in the sealing contact, while the viscosity of the fluid used has a significant influence. Due to splashing and heat dissipation from the sealing contact area, the oil level strongly influences the frictional loss of the seal. The auxiliary or protective lips on the seals tend to increase the seal friction torque. For the same radial force and seal material, the oil viscosity is the major contributor to frictional loss. However, the radial force or the contact pressure at the sealing area also influences considerably.

2.2.5 Oil Drag Loss

The introduction of oil injection can have a significant impact on the thermal efficiency of the compressor. Achieving the highest mass flow rate and compression efficiency requires careful optimization of factors such as oil viscosity, injection position, temperature, and uniform distribution within the compression chamber. These optimal levels are influenced by operational conditions like tip speed and pressure ratio. Nevertheless, excessive oil injection can result in unfavourable frictional and momentum losses, ultimately leading to an increase in power consumption, as outlined by Deipenwisch and Kauder (1999).

2.2.5.1 Analytical Models

Deipenwisch and Kauder (1999)

Among the initial investigations in this field, Deipenwisch and Kauder (1999) conducted a study focusing on power losses attributed to the presence of oil within the working chamber of a screw compressor. This research paper illuminates two primary mechanisms accountable for these power losses, namely shear losses and momentum losses.

$$\dot{\phi}_{AR} = \dot{\phi}_{B,Oil} + \dot{\phi}_R + \dot{\phi}_l \quad (2.7)$$

where $\dot{\phi}_{AR}$ is the power loss in the working chamber [W], $\dot{\phi}_{B,Oil}$ is the power loss because of the acceleration of oil [W], $\dot{\phi}_R$ is the power loss because of friction or shear [W] and $\dot{\phi}_l$ is the power loss because of momentum loss [W].

Power losses by acceleration: The dissipation of power occurs due to the acceleration of oil at the injection port. It is assumed that the oil is accelerated from zero velocity at the inlet to match the rotor's velocity at the injection point. However, it's worth noting that the power losses calculated using the following equation tend to overestimate the actual losses. This is primarily because the kinetic energy of the oil before injection is not accounted for in the calculation. Additionally, it should be acknowledged that only a portion of the injected oil will actually reach the rotor's speed, leading to a reduction in the actual power loss figure.

$$\dot{\phi}_{B,Oil} = \frac{1}{2} \rho_{oil} \dot{V}_{oil} u_{MR}^2 \quad (2.8)$$

here, ρ_{oil} is oil density in [kg/m³], \dot{V}_{oil} is the volumetric flow of the oil at injection point [m³/s] and u_{MR} is the male rotor tip speed [m/s].

Power losses in the clearances caused by hydraulic friction: When estimating power losses within the clearances, the calculation assumes that the clearance volume is completely occupied by oil. The authors draw a comparison between the flow within these clearances and the lubricant flow found in the clearances of journal bearings. To formulate the equation, the authors adopt the concept of Couette flow for describing the oil flow through the clearances. As a result, they put forward the

following equation to model this phenomenon:

$$\dot{\phi}_R = \frac{A_{sp}\eta_{oil}v_{rel}^2}{h_{sp}} + \frac{\Delta p A_{sp} v_{rel}}{2} \quad (2.9)$$

In this context, the variables have specific meanings: A_{sp} represents the area of the clearance that has been exceeded, calculated as the product of the width and length of the clearance area [m²]. η_{oil} corresponds to the dynamic viscosity of the oil [Pa.s], v_{rel} signifies the relative velocity of the oil flow [m/s], h_{sp} stands for the height of the clearance [m], and Δp denotes the pressure difference across the clearances [Pa]. Notably, it is estimated that the power losses resulting from friction due to pressure drop account for approximately 10-15% of the total frictional power losses.

Momentum losses caused by the acceleration of the oil in the clearances: The oil film that develops on the inner surfaces of the housing and the rotor experiences periodic acceleration by the rotor's tips and subsequently decelerates as the rotor tooth passes. This flow within the clearance can be likened to the time-dependent evolution of a hydraulic friction layer between a wall that undergoes sudden motion and another wall that remains stationary. The estimation of momentum losses in this context can be expressed using the following equation

$$\dot{\phi}_l = \frac{8}{3} \frac{A_{sp}\eta_{oil}v_{rel}^2}{Z^2 h_{sp}} \quad (2.10)$$

where Z is the Couette flow parameter, a quotient of the thickness of the layer carried by the friction and clearance height.

The experimental validation of this predictive model reveals an average disparity of approximately 8% across various operational speeds, pressure ratios, and oil volume flow rates. It's important to note that the model assumes the flow within the clearances to be purely Couette flow (viscous-driven). However, in practical scenarios, the flow within the clearances comprises a combination of both Couette and Poiseuille flow (pressure-driven). This, coupled with potential measurement inaccuracies, could account for the observed variance between the predicted and experimental outcomes.

Gräßer and Brümmer (2014)

In their work, Gräßer and Brümmer (2014) introduced an analytical model that addresses the incompressible single-phase flow of auxiliary or lubricating fluid through the clearances within screw machines, including expanders and compressors. This analytical model is rooted in the concept of superposed Couette-Poiseuille flow, which encompasses both laminar and turbulent flow processes. By leveraging this model, the authors aim to provide insights into the complex flow dynamics occurring within the clearances of screw machines, facilitating a deeper understanding of their operational behaviour.

The analytical framework developed by Gräßer and Brümmer (2014) encompasses the study of static, incompressible fluid flow occurring between parallel walls that are set in motion. Subsequently, this model is extended to encompass the intricate geometrical features found within the front and housing clearances of screw machines. These complex clearances are defined by a finite number of wall elements, interconnected either in a series or parallel configuration.

Within this analytical context, the assumption of laminar, two-dimensional flow is made. This assumption is supported by the premise that the transverse velocity component C_y is significantly smaller than the axial velocity C_x . Furthermore, a constant pressure gradient dp/dx and uniform wall velocity C are postulated at one side of the clearance.

By applying the principles of differential conservation equations for both mass and momentum, the resulting flow velocity within this defined system can be derived. This process serves to explain the flow behaviour under the specified conditions, offering valuable insights into the dynamic interaction between laminar and turbulent flow phenomena.

A notable aspect of this modelling approach is the introduction of a sharp transition from laminar to turbulent flow. This transition is characterized by critical Reynolds numbers, which are contingent upon operational parameters and the specific geometrical attributes of the flow environment.

The comprehensive scope of this modelling effort is visually illustrated in Figure 2.14, which outlines the key components and considerations involved in the analysis.

Through the incorporation of these elements, the analytical model seeks to enhance understanding of the intricate flow patterns occurring within the clearances of screw machines, shedding light on the complex interplay between laminar and turbulent flow dynamics.

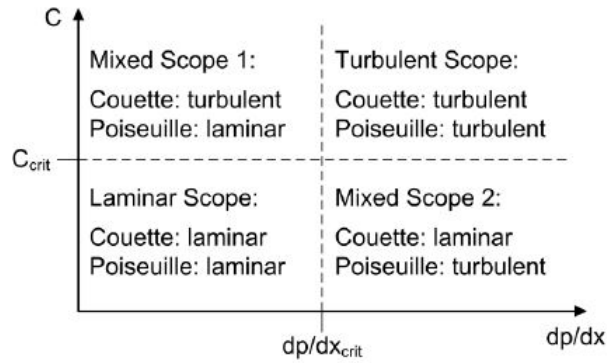


Figure 2.14: Scopes of modelling

The study involves an examination of flows with mixed characteristics, where turbulence dominates in one partial flow while another partial flow is treated as laminar due to the unsuitability of the turbulent model for low partial Reynolds numbers. The authors acknowledge potential uncertainties in the model, noting that laminar flow is typically overshadowed by turbulent flow in mixed scenarios. Consequently, they develop a comprehensive model to accurately assess laminar and turbulent Couette-Poiseuille flow between parallel walls. This innovative model is subsequently put to the test through a comparative analysis of analytical results and numerical simulations.

Furthermore, the investigation delves into the intriguing interplay between power losses induced by friction on the rotor's surface and their effects, particularly within radial and axial clearances. The study contends that friction might actually drive the rotor within these clearances, a phenomenon contingent upon the cancellation of Couette flow by Poiseuille flow. Notably, the study reveals that the necessary pressure differentials are notably lower for male rotor housing clearances compared to male rotor front clearances. While these aspects are explored in detail, the study refrains from offering an analysis of drag arising in the interlobe clearance, leaving room for potential future exploration and insights.

Gräßer and Brümmer (2015)

Expanding upon their analytical model, the authors delve into a comprehensive evaluation of the dual effects resulting from improved sealing of clearances in screw expanders. While the primary goal of clearance sealing is performance enhancement, it unavoidably brings about elevated frictional losses. Employing the advanced multi-chamber model-based simulation tool, KaSim, developed by the Chair of Fluidics, the study delves into the upper limits of sealing potential using water and oil as sealants. This computational approach provides an understanding of how sealing impacts performance and frictional losses within the context of screw expanders.

The internal isentropic efficiency of the screw expander is defined by

$$\eta_{i,s} = \frac{P_i}{\dot{m}(h_I - h_{O,s})} \quad (2.11)$$

here, h_I is the inlet enthalpy while $h_{O,s}$ is the outlet isentropic enthalpy. While hydraulic isentropic efficiency is defined by

$$\eta_{hyd,s} = \frac{|P_i| - P_c}{\dot{m}w_s} \quad (2.12)$$

In this context, $\eta_{hyd,s}$ represents the hydraulic isentropic efficiency, P_c denotes the hydraulic power associated with sealed clearances, and signifies the specific isentropic work. The analysis yields noteworthy insights. At low circumferential speeds, the internal isentropic efficiency witnesses improvement with enhanced sealing of the clearances. Conversely, the amplified sealing brings about additional frictional power in screw expanders, albeit negligible at low circumferential speeds. When it comes to dry-running expanders operating at low circumferential speeds, improved sealing results in higher hydraulic efficiency compared to internal isentropic efficiency. However, this pattern shifts at higher circumferential speeds, favouring dry screw expanders. To gain a holistic understanding of the optimal balance between hydraulic and internal isentropic efficiencies, the authors propose the development of a comprehensive model. This model could encompass various factors, such as the influence of oil surge and cooling of the working fluid.

Gräßer and Brümmer (2016)

The paper by Gräßer and Brümmer (2016) offers a theoretical examination of the correlation between clearance sealing and frictional loss for both liquid-flooded and dry screw expanders, specifically focusing on radial and axial clearances. The authors delve into the impact of water and oil on the interplay between clearance sealing, frictional losses, and the overall performance of screw expanders. Through a comprehensive thermodynamic analysis, the study reveals that the performance of the screw expander experiences minimal alteration due to variations in liquid water injection temperature. However, it is worth noting that the modelling of oil necessitates a consideration of temperature-dependent dynamic viscosity, underscoring the nuanced nature of the relationship between fluid properties and performance outcomes.

The investigation's findings demonstrate that the thermodynamic performance of the screw expander is significantly affected by the clearances between the interlobe and housing. Moreover, there exists a moderate impact on the performance from high-pressure front clearance and blow-hole. On the other hand, the low-pressure front clearance exerts a minimal influence on the performance. A comparison between water-flooded and dry operating screw expanders reveals that the former exhibit superior efficiency at both low and high circumferential speeds. Conversely, oil-injected screw expanders prove more advantageous at low circumferential speeds, while dry screw expanders excel at high circumferential speeds. It is worth noting that the hydraulic efficiency of the screw expander is minimally affected by water injection temperature, while it exhibits significant variation based on oil injection temperature.

The authors assert that certain facets of liquid-injected screw machines have not been fully addressed in this study. Given the pronounced impact of interlobe clearance on thermodynamic performance, the authors contend that its inclusion in the analysis is warranted. Additionally, the study anticipates potential additional losses in front and housing clearances due to oil surge. Furthermore, the investigation aims to incorporate multiphase expansion and the heat exchange between gas and liquid phases as integral components of the study.

2.2.5.2 Computational Models

Gräßer and Brümmer (2014)

The authors compared the analytical and computational models using ANSYS CFX. For model evaluation, water at 25°C was compared with numeric simulation. A 2D flow model used a structured mesh (1201x149x2 cells) was generated. Inlet/outlet static pressure, wall velocities provided boundary conditions. The Model described turbulence, including mass flow and wall shear stress. For turbulent Couette flow, mass flows are identical, wall shear stress differs by 12%. In turbulent Poiseuille flow, mass flow differs by 12%, wall shear stress by 3%. Authors concluded that this is within the acceptable level of variation.

The authors found significant impact of male rotor housing clearance geometry on results. Hence, crucial to study liquid distribution in screw machines for insights into chamber-clearance complexities.

Vasuthevan and Brümmer (2018)

Vasuthevan and Brümmer (2018) presented a Computational Fluid Dynamics (CFD) simulation model aimed at analysing the multiphase flow in a screw compressor to understand the hydraulic loss mechanism. This study focuses on investigating the influence of two key factors: the quantity of injected oil and the rotational speed of the rotors. To accomplish this, a 2D representation of a rectangular contour was simulated.

The results of their simulation analysis led the authors to draw several important conclusions. Firstly, they found that the hydraulic loss experiences an increase with both the tip speed and the oil injection flow rate. Additionally, the relationship between hydraulic loss and the rate of oil flow is determined to be linearly proportional. In contrast, the hydraulic loss displays a proportionality to the square of the tip speed.

2.2.5.3 Experimental Investigation

Basha et al. (2018)

In a study conducted by Basha et al. (2018) , a series of experimental investigations were undertaken to comprehensively comprehend the impact of oil injection on the performance of a twin-screw compressor. The compressor under examination was appropriately sized for a 22 kW power input. Throughout the experimentation process, various parameters were meticulously analysed, including the mass flow rate of the working fluid, shaft speed, injection position, and the temperature of the injected oil.

The findings of the study reveal a significant insight. Specifically, at discharge pressures of 6.5 and 8.5 bar, a noteworthy trend emerges: the consumption of shaft power exhibits an augmentation with an increase in the rate of oil injection. This observation implies that the rise in shaft power consumption could be attributed to an amplification in drag loss.

He et al. (2018)

In a separate experimental exploration, He et al. (2018) delved into the characteristics of a 75 kW compressor equipped with a male rotor measuring 178.5 mm. This investigation aimed to notice the influence of oil flow rate on distinct parameters, including volumetric efficiency, adiabatic efficiency, and specific power consumption.

Notably, the results of this study unveil intriguing patterns. While the volumetric efficiency exhibits a continuous rise in direct correlation with the oil injection flow rate, the specific power consumption remains remarkably consistent within the same range of oil flow rates. A comprehensive examination of these effects relative to the oil flow rate highlights a distinct trend: as the oil flow rate increases, so does the consumption of shaft power.

It's important to acknowledge that, despite the availability of several computational studies, a concise analytical model for predicting oil drag loss in screw compressors has yet to be developed. The analytical approach offers certain advantages over numerical methods, including significantly shorter calculation times and a clearer visualization of the underlying physical principles that govern flow processes. More-

over, the current body of literature on drag loss lacks a quantified assessment of drag loss across various clearance pathways within the compression chamber; typically, such quantification is approximated.

2.3 Power Transmission Loss

2.3.1 Gear Drive

The basic principles of the design of gears are given in a book on Gears and Gear drives by Jelaska (2012). The book presented a method to estimate the power loss in gear drives which is divided into four categories: meshing loss, idle running loss, seal loss, and bearing loss.

2.3.1.1 Power loss in mesh, under load, for a single gear pair

The power loss in mesh, under load, for a single gear pair for a cylindrical gear drive is obtained by the following equation.

$$P_{ZP} = \mu_{mZ} P H_V \quad (2.13)$$

where, μ_{mZ} is the mean coefficient of friction in mesh, P is transmitted power [kW], and H_V is the factor of power losses in the mesh. The mean coefficient of friction in the mesh is approximately equal to the coefficient of friction in the pitch point.

$$\mu_{mZ} \approx \mu_c = 0.12 \times \sqrt[4]{\frac{w_{Bt} R_a}{\eta_{oil} v_{\Sigma C} \rho_{cn}}} \quad (2.14)$$

where, w_{Bt} is the specific tooth load in transverse plane [N/m], R_a is the arithmetic mean roughness of meshed teeth [μm], $R_a = (R_{a1} + R_{a2})/2$, η_{oil} is the dynamic viscosity of oil at operating temperature [mPa.s], $v_{\Sigma C}$ is the sum of the peripheral speeds in the pitch point [m/s] and ρ_{cn} is the equivalent radius of meshed profiles curvature in the pitch point in the normal plane [mm]. The specific load in the transverse plane w_{Bt} is calculated by the following equation

$$w_{Bt} = K_A K_V K_{B\alpha} K_{B\beta} K_{B\gamma} \frac{F_t}{b} \quad (2.15)$$

where, K_A is application factor, K_V is internal dynamic factor, $K_{B\alpha}$ is the transverse load factor, $K_{B\beta}$ is the face width factor, $K_{B\gamma}$ is helix angle factor, F_t is reference circle peripheral force [N] and b is face width [mm]. The value of the application factor can be taken from the following table.

Table 2.2: Rough values of factor K_A application (Jelaska, 2012)

Driving machine loads	Driven machine loads			
	Uniform	Moderate impact	Mean impact	High impact
Uniform: electro-motors, steam and gas turbines of uniform speed and low torques	1.00	1.25	1.50	1.75
Moderate impact: steam and gas turbines, hydro-motors, electro-motors of high and variable torque	1.10	1.35	1.60	1.85
Mean impact: multi-cylindrical internal combustion engines	1.25	1.50	1.75	2.00
High impact: single-cylindrical internal combustion engines	1.50	1.75	2.00	2.25 and more

The basic equation for determining dynamic factor is as follows

$$K_V = 1 + f_F k_v \quad (2.16)$$

The correction factor, f_F required for the dynamic factor calculation, is obtained from the following table. The table shows correction factor values for different accuracy grades by ISO and specific loading $K_A F_t / b$. Here, F_t is reference circle peripheral force [N] and b is gear width [mm].

Table 2.3: Correction factor (Jelaska, 2012)

Accuracy grade by ISO	$K_A F_t / b$ (N/mm)							
	≤ 100	200	350	500	800	1200	1500	2000
3	1.96	1.29	1.0	0.88	0.78	0.73	0.70	0.68
4	2.21	1.36	1.0	0.85	0.73	0.66	0.62	0.60
5	2.56	1.47	1.0	0.81	0.65	0.56	0.52	0.48
6	2.82	1.55	1.0	0.78	0.59	0.48	0.44	0.39
7	3.03	1.61	1.0	0.76	0.54	0.42	0.37	0.33
8	3.19	1.66	1.0	0.74	0.51	0.38	0.33	0.28
9	3.27	1.68	1.0	0.73	0.49	0.36	0.30	0.25
10	3.35	1.70	1.0	0.72	0.47	0.33	0.28	0.22
11	3.39	1.72	1.0	0.71	0.46	0.32	0.27	0.21
12	3.43	1.73	1.0	0.71	0.45	0.31	0.25	0.20

The value of vibration factor k_v is dependent on gear ratio (u), peripheral speed (v) [m/s] and number of teeth z_1 . Its value can be obtained for different gear qualities from the following figure.

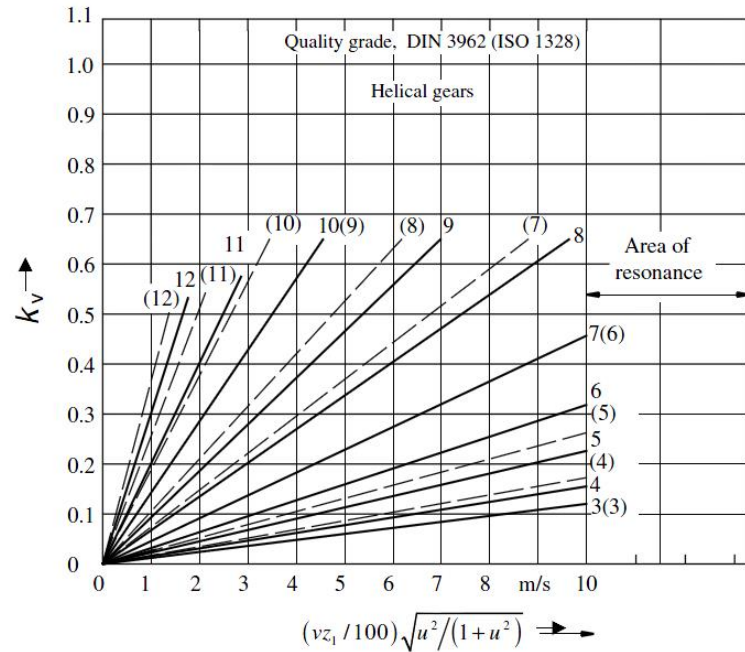


Figure 2.15: Vibration factor (Jelaska, 2012)

The sum of peripheral speeds in the pitch point is equal to

$$v_{\Sigma c} = 2\nu \tan \alpha_w \cos \alpha_t \quad (2.17)$$

The equivalent radius of meshed profiles curvature at pitch point C in the normal plane

$$\rho_{cn} = a \frac{u}{(u+1)^2} \frac{\sin \alpha_w}{\cos \beta_b} \quad (2.18)$$

The dynamic viscosity of the oil at operating temperature is determined by the equation:

$$\eta_{oil} = 0.1282 \eta_{50}^{\frac{174}{\vartheta_{oil}+95}} - 0.198 \frac{298}{e^{\vartheta_{oil}+95}} \quad (2.19)$$

where η_{50} is the dynamic viscosity of oil at operating temperature of 50°C and ϑ_{oil} is the operating temperature of oil [°C]. The following equation determines the factor of power loss in the mesh

$$H_V = \pi \left(\frac{1}{z_1} + \frac{1}{z_2} \right) \frac{1}{\cos \beta_b} (1 + \epsilon_1^2 + \epsilon_2^2 - \epsilon_\alpha) \quad (2.20)$$

2.3.1.2 Power loss in idle motion

Bath lubrication

When gears rotate in idle motion, they still contribute to power loss even if they are transmitting minimal torque. The hydraulic moment of power loss when gears are bath lubricated,

$$T_H = C_{Sp} C_1 e^{C_2 \left(\frac{v}{v_{t0}} \right)} \quad (2.21)$$

here, v is the reference circle peripheral speed of dived gear [m/s], v_{t0} is a constant with value 10 m/s. The factors C_{Sp} , C_1 and C_2 indicate the effect of oil spraying, gear width and depth of diving in the oil bath, respectively, on the idle motion power loss. If the gears engage with each other from the oil bath side, the value of factor C_{Sp} is set to '1'. If the gears are disengaging on the oil bath side, then C_{Sp} is calculated using the following formula

$$C_{Sp} = \left(\frac{4e_{max}}{3h_c} \right)^{1.5} \frac{2h_c}{l_h} \quad (2.22)$$

where, e_{max} is the maximum of two values e_1 and e_2 of the diving depth of mated gears, h_c is the height of the pitch point over the deepest dive point, and l_h is the hydraulic length of the gear drive housing.

$$l_h = \frac{4A_K}{O} \quad (2.23)$$

where A_K is the inside surface of the gear drive housing near the wheel gear and O is the perimeter of that surface. The hydraulic length of the housing is commonly in the range $l_h = (500 \dots 1000 \dots 1300)$ mm, or $l_h = (1.0 \text{ to } 2.0)d_{a2}$. Factors C_1 and C_2 are determined by the following equations

$$C_1 = 0.063 \left(\frac{e_1 + e_2}{e_0} \right) + 0.0128 \left(\frac{b}{b_0} \right)^3 \quad (2.24)$$

$$C_2 = \frac{e_1 + e_2}{80e_0} + 0.2 \quad (2.25)$$

where, e_1 and e_2 are depths of diving of the pinion and wheel and $e_2=b_0=10$ mm. Total power loss in idle motion is

$$P_{Z0} = \sum_{i=1}^k T_{Hi} \frac{\pi n_i}{30} \quad (2.26)$$

where, k is the total number of gear pairs in a drive.

Spray lubrication

The hydraulic moment of power loss for spray lubrication for starting side of the gear mesh

$$T_H = 1.67 \times 10^{-6} \rho_{oil} Q_e d (v - v_s) + 32 \times 10^{-9} \rho_{oil} d_w^{1.5} \nu_{oil}^{0.065} m_n^{0.18} b^{0.15} v^{1.5} \left(\frac{Q_e}{Q_{e0}} \right)^{0.1} + 0.1 \quad (2.27)$$

Similarly, for the end side of the gear mesh, the hydraulic moment of power loss is

$$T_H = 8.33 \times 10^{-6} \rho_{oil} Q_e d_w (v + v_s) \quad (2.28)$$

here, ν_{oil} is the kinematic viscosity of oil [mm^2/s], ρ_{oil} is the lubricant density [kg/dm^3], Q_e is the quantity of lubricant sprayed [dm^3/min], $Q_{e0}=2 \text{ dm}^3/\text{min}$, v is the reference circle peripheral speed [m/s], d_w is the pitch diameter of dived gear [mm], and v_s is the speed of sprayed lubricant [m/s].

The total power loss in the mesh is equal to the sum of power loss in the mesh under load and power loss in idle motion.

$$P_Z = P_{ZP} + P_{Z0} \quad (2.29)$$

The results and parametric analysis of this method proposed by Jelaska (2012) are presented in the next chapter.

2.3.2 Belt Drive

Bertini et al. (2014) presented a closed-form analytical model for the power loss in rubber V-belt. The frictional losses are grouped into three contributions: frictional sliding, belt hysteresis, and belt engagement/disengagement. The results of the model are validated with experimental measurements.

A test apparatus to investigate the heat generated in V-belts is presented by Káta and Szabó (2015). Based on the measurements, a calculation method is proposed to estimate the damping coefficient, temperature rise-pulley diameter, and temperature rise-pulley frequency relationship.

2.4 Electric Motors and Frequency Converter Losses

A book by Hughes and Drury (2019) provides the basics of electric motors, power electronics, types of electric motors, and variable frequency operation. El-Ibiary (2003) has proposed a method to predict electric motor efficiency. The author claims an accuracy level of 99% by validating predicted results with the test results. The study can calculate the motor output power by using proposed equations and referring to IEEE Standard. The method includes the measurement of input values of voltage, current, power, stator resistance, and motor shaft speed.

The literature states that the motor's efficiency (E) and power factor increase

with the increase in percentage full rated load. This implies that the motor should be run at full rated load instead of at its part load. Also, the motor's power factor improves with the increase in motor speed, which in turn helps to increase the motor efficiency. This phenomenon is explained by the relative magnitudes of input voltage (V) and the motor's efficiency (E). As the input voltage increases, that means the speed of the motor increases, but the magnitudes of current and resistance remain the same, which keeps resistance loss (I^2R) the same and hence the efficiency of the motor increases. The inherent variable losses of the motor, like stator and rotor (I^2R) losses, stray load loss, friction, and windage losses can be reduced by reducing the line current of the motor. These losses are proportional to the product of the square of the line's current and resistance.

Mehltretter (2014) demonstrated that the compressor systems, which are appropriately sized based on demand profile and operating with a master controller, provide the most efficient operation. Multiple compressor systems should be used with master controllers and variable speed controllers to achieve the best possible efficiency from the plant.

Sophisticated software for designing and optimising variable speed drives is proposed by Sirovỳ et al. (2011). The software is developed for high-power pumps to assist designers in developing pump characteristics to operate optimally. The authors expressed that due to several converter topologies and different power devices, it is impossible to propose a general mathematical model of the converter providing high-accuracy results. So it is suggested to obtain the manufacturer's required information on frequency converter efficiency.

Bell et al. (2020) presented that PDSim uses three different models for the performance prediction of single-phase induction motors. The first model is where the motor's efficiency is considered constant. In the second model the motor's efficiency is calculated as a function of torque and slip velocity while in the third model, it is calculated as a semi-deterministic model that includes heat and friction losses.

The Sankey diagram of the power flow of a single-phase induction motor is shown in Figure 2.16. Total power loss through the motor is the sum of power loss through the stator, rotor, core, windings, and stray losses.

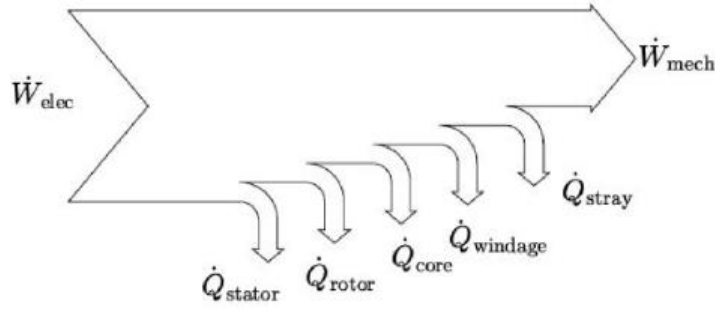


Figure 2.16: Power flow of single-phase induction motor (Bell et al., 2020)

The PDSim model accepts the parameters like motor torque, efficiency, and speed as input from the users and plots them to generate a performance map. These parameters are interpolated within the program to predict motor performance.

2.5 Summary

In the face of ever-increasing demand, designing energy-efficient machinery poses a substantial challenge for engineers. The initial imperative towards achieving this objective involves identifying the components through which power loss occurs and subsequently quantifying these losses.

Existing mathematical models within the literature aimed at predicting the performance of screw compressors have been meticulously examined. However, the methodologies for calculating power losses in these models have often relied on approximations or empirical correlations. This approach tends to overlook the individual contributions of specific components to the overall power loss. If the distinct roles of these components in power loss, coupled with their behaviour under diverse operational conditions, are comprehended, the design process can be strategically tailored to mitigate these losses. Armed with this knowledge during the design phase, the need for prototype development and the associated time and cost of testing validation can be substantially curtailed.

Moreover, the current literature predominantly centres on the analysis of individual screw compressors, leaving a notable research gap concerning the comprehensive examination of screw compressor systems as integrated packages. This broader perspective should encompass aspects like the drive motor, gearbox, bearings, and other

pertinent components. The development of a method that accounts for the impact of these elements on the holistic system performance and their parametric interactions is imperative.

For the purpose of these studies, a 55 kW, oil-injected, twin-screw air compressor unit manufactured by Kirloskar Pneumatic Company Limited, India, and powered by an electric motor has been selected as the subject of investigation. A visual representation of this compressor unit is provided in Figure 2.17.

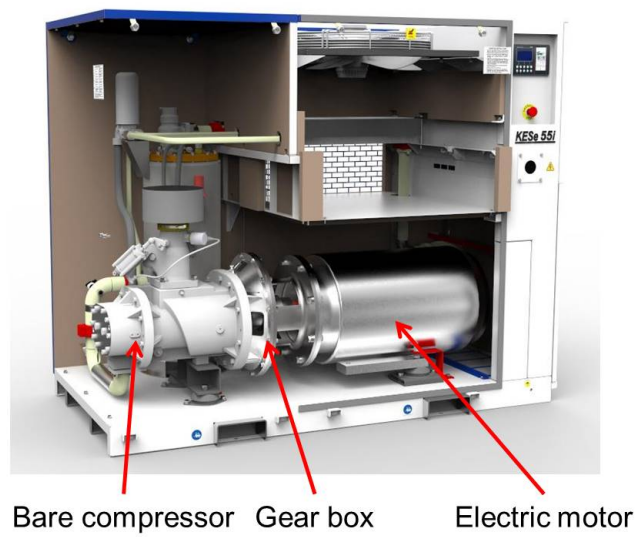


Figure 2.17: A 55 kW, air screw compressor unit of Kirloskar Pneumatic Company Limited

Chapter 3

Research Aims

In addition to the meticulous individual design of the components comprising the packaged screw compressor, achieving optimal integration of these parts and predicting performance at the system level across diverse operating conditions is of paramount importance. Within the context of an electrically driven screw compressor system, the elements that contribute to power loss have been identified through an extensive literature review. Researchers have made noteworthy strides in predicting power loss arising from specific components. However, there exists a noticeable gap in terms of a unified methodology capable of predicting the cumulative power loss across the entire system.

To address this gap, it becomes imperative to develop an integrated approach that encapsulates the intricate interactions and cumulative impact of various components on the overall power loss within the system. Such an approach would significantly advance the comprehension of system-level behaviour and subsequently empower designers to make informed decisions, fostering the creation of more energy-efficient and optimally performing screw compressor systems.

The overall performance of a packaged screw compressor system depends upon the following parameters:

- Rotor profile and configuration
- Housing and port design
- Part load control system

- Lubrication system
- Type of drive
- Range of operating conditions
- Maintenance requirements

3.1 Aim of Research

This study aims to develop a method to predict the mechanical loss of the individual elements of the compressor. Upon identification and quantification of the mechanical loss, overall system performance can be predicted for wide operating conditions.

3.2 Methods Used

The research aims can be achieved by the following methods mentioned below

- Carry out a literature survey of all known publications related to screw compressor design and operation.
- Identify and quantify the mechanical loss of individual elements of the screw compressor.
- Investigate available methods and/or develop new methods that will accurately predict the mechanical loss of the compressor.
- Prediction of total mechanical loss and investigate how various features of the compressor system influence the system performance.
- Validate predictions by using results of experimental investigation of the selected compressor configuration.

3.3 Expected Contribution

The study presented in this thesis is expected to be an extension of the available software tools for the performance prediction of screw compressors. The major contribution can be realised in the following ways.

- Identifying and quantifying different power loss contributing elements within the screw compressor.
- Development of a power loss prediction model for different sizes of oil-flooded screw compressors and different operating conditions.
- Improvement in power loss prediction of the available performance prediction programs can be achieved using developed correlations.
- The effect of different geometries of components like rotors, bearings, and seals on the power loss can be analysed independently, which is not possible with the available performance prediction programs.
- With the accurate prediction of power loss at the design level, effective utilisation of time and finances can be realised during the development of the prototype, testing, and validation.

Therefore, it can be interpreted that the developed methods can be readily adopted in performance prediction programs.

Chapter 4

Development of Power Loss Model

4.1 Introduction

This chapter is dedicated to outlining the methods that have been either adopted or developed to estimate the mechanical losses associated with each individual element of the compressor. A thorough investigation has been conducted into various methods existing within the literature for the prediction of power losses in gears, bearings, and shaft seals. These methods have been meticulously assessed for their suitability within the operational range of the compressor. The outcomes of these methods have been systematically compared against available experimental measurements to validate their efficacy.

The central emphasis of this chapter revolves around presenting power loss estimation models specifically addressing key elements like bearings and the drag loss attributed to oil. Through a comprehensive exploration of these elements, this chapter contributes to the broader understanding of mechanical losses within the context of the studied compressor system.

For the prediction of power loss in electric motors and frequency converters, Sirov y et al. (2011) has noted that due to the several converter topologies and diverse power devices in use, proposing a universal method is deemed unfeasible. The complexity coming from these variations necessitates a case-specific approach tailored to the specific characteristics and configurations of electric motors and frequency converters.

4.2 Bearing Power Loss

The number of compressors which are designed for the range of input power from 15 to 160 kW, under the research collaboration (section 1.6) have only rolling element bearings. The most frequently used methods for estimating power loss in rolling element bearings are SKF, Harris and Palmgren. The governing equations for predicting power loss in rolling element bearings are based on empirical correlations.

4.2.1 SKF model

This model is developed by SKF which considers tribological phenomena that occur in the lubricating film between the rolling elements, raceways and cages. The model is derived from computational models developed by SKF. The bearing frictional power loss can be calculated using the following equation

$$P_{loss} = 1.05 \times 10^{-4} M n \quad (4.1)$$

where, P_{loss} is the bearing frictional power loss [W], M is the total frictional moment [Nmm] and n is the rotational speed [rpm].

The total frictional moment in a rolling bearing consists of four elements: the rolling frictional moment, the sliding frictional moment, the frictional moment from seal/s and the frictional moment from drag losses, churning and splashing. It is defined as follows

$$M = M_{rr} + M_{sl} + M_{seal} + M_{drag} \quad (4.2)$$

where M_{rr} is the rolling frictional moment [Nmm] which signifies high-speed starvation of bearing and inlet shear heating of the lubricating oil, M_{sl} is sliding frictional moment [Nmm] which signifies the effect of the quality of lubrication on the bearing, M_{seal} is the frictional moment of seals [Nmm] where seals do not allow the pre-filled grease of the bearing to leak out, M_{drag} is the frictional moment of drag losses, churning, splashing of lubricant etc. [Nmm].

4.2.1.1 Rolling frictional moment

The rolling frictional moment is calculated using the following equation

$$M_{rr} = \phi_{ish} \phi_{rs} G_{rr} (\nu n)^{0.6} \quad (4.3)$$

where, ϕ_{ish} is inlet shear heating reduction factor, ϕ_{rs} is kinematic replenishment/starvation reduction factor, G_{rr} is variable which depends on bearing type, dimension and loads acting on it, ν is the actual operating viscosity of oil or the base oil of the grease [mm^2/s].

The inlet shear heating reduction factor represents the frictional loss because of the shearing in the lubricant as shown in Figure 4.1. This shearing effect is caused by the heating, which lowers the lubricant viscosity and reduces the film thickness.

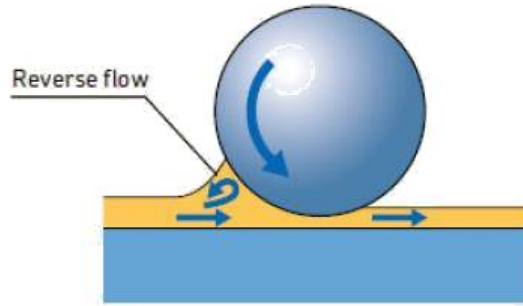


Figure 4.1: Shearing of lubricant (SKF, 2018)

It can be defined as follows

$$\phi_{ish} = \frac{1}{1 + 1.84 \times 10^{-9} (nd_m)^{1.28} \nu^{0.64}} \quad (4.4)$$

where d_m is the bearing mean diameter, an arithmetic mean of bearing bore diameter and bearing outer diameter [mm]. The kinematic replenishment/starvation reduction factor defines the replenishment/starvation of the bearing raceways. The lubricant may not get replenished in bearing raceways because of the lubricant viscosity or high speeds, which will lead to starvation and ultimately rise in temperatures because of

reduced lubricant film thickness. It is estimated using the following equation

$$\phi_{rs} = \frac{1}{e^{K_{rs}\nu n(d+D)}\sqrt{\frac{K_Z}{2(D-d)}}} \quad (4.5)$$

where K_{rs} is the replenishment/starvation constant and K_Z is the geometric constant based on bearing type.

$K_{rs} = 3 \times 10^{-8}$ for low-level oil bath and oil jet lubrication

$K_{rs} = 6 \times 10^{-8}$ for grease lubrication.

The value of K_Z can be taken from the following table.

Table 4.1: Geometric constants K_Z and K_L (SKF, 2018)

Geometric constants K_Z and K_L		
Bearing type	Geometric constants	
	K_Z	K_L
Deep groove ball bearings – single and double row	3,1	–
Angular contact ball bearings – single row	4,4	–
– double row	3,1	–
– four-point contact	3,1	–
Self-aligning ball bearings	4,8	–
Cylindrical roller bearings – with a cage	5,1	0,65
– full complement	6,2	0,7
Tapered roller bearings	6	0,7
Spherical roller bearings	5,5	0,8
CARB toroidal roller bearings – with a cage	5,3	0,8
– full complement	6	0,75
Thrust ball bearings	3,8	–
Cylindrical roller thrust bearings	4,4	0,43
Spherical roller thrust bearings	5,6	0,58 ¹⁾

¹⁾ Only for single mounted bearings

4.2.1.2 Sliding frictional moment

The sliding frictional moment can be estimated using the following equation

$$M_{sl} = G_{sl}\mu_{sl} \quad (4.6)$$

where, G_{sl} is a variable given in Table 4.2 which depends on bearing type, geometry and loads while μ_{sl} is the sliding friction coefficient. The sliding friction coefficient can be calculated as

$$\mu_{sl} = \phi_{bl}\mu_{bl} + (1 - \phi_{bl})\mu_{EHL} \quad (4.7)$$

where ϕ_{bl} is the weighting factor for the sliding friction coefficient defined in the following equation

$$\phi_{bl} = \frac{1}{e^{2.6 \times 10^{-8}(n\nu)^{1.4}d_m}} \quad (4.8)$$

μ_{bl} is the coefficient depending on the additive package in the lubricant. Generally, it is taken as 0.15. μ_{EHL} is the sliding friction coefficient in full-film conditions. Its value for cylindrical roller bearing is 0.02, while for tapered roller bearing, it is 0.002.

Table 4.2: Geometric constants G_{rr} and G_{sl} (SKF, 2018)

Geometric and load dependent variables for rolling and sliding frictional moments – radial bearings		
Bearing type	Rolling frictional variable G_{rr}	Sliding frictional variable G_{sl}
Deep groove ball bearings	when $F_a = 0$ $G_{rr} = R_1 d_m^{1,96} F_r^{0,54}$	when $F_a = 0$ $G_{sl} = S_1 d_m^{-0,26} F_r^{5/3}$
	when $F_a > 0$ $G_{rr} = R_1 d_m^{1,96} \left(F_r + \frac{R_2}{\sin \alpha_f} F_a \right)^{0,54}$	when $F_a > 0$ $G_{sl} = S_1 d_m^{-0,145} \left(F_r^5 + \frac{S_2 d_m^{1,5}}{\sin \alpha_f} F_a^4 \right)^{1/3}$
	$\alpha_f = 24,6 (F_d/C_0)^{0,24} [^\circ]$	
Angular contact ball bearings ¹⁾	$G_{rr} = R_1 d_m^{1,97} [F_r + F_g + R_2 F_a]^{0,54}$ $F_g = R_3 d_m^4 n^2$	$G_{sl} = S_1 d_m^{0,26} [(F_r + F_g)^{4/3} + S_2 F_a^{4/3}]$ $F_g = S_3 d_m^4 n^2$
Four-point contact ball bearings	$G_{rr} = R_1 d_m^{1,97} [F_r + F_g + R_2 F_a]^{0,54}$ $F_g = R_3 d_m^4 n^2$	$G_{sl} = S_1 d_m^{0,26} [(F_r + F_g)^{4/3} + S_2 F_a^{4/3}]$ $F_g = S_3 d_m^4 n^2$
Self-aligning ball bearings	$G_{rr} = R_1 d_m^2 [F_r + F_g + R_2 F_a]^{0,54}$ $F_g = R_3 d_m^{3,5} n^2$	$G_{sl} = S_1 d_m^{-0,12} [(F_r + F_g)^{4/3} + S_2 F_a^{4/3}]$ $F_g = S_3 d_m^{3,5} n^2$
Cylindrical roller bearings	$G_{rr} = R_1 d_m^{2,41} F_r^{0,31}$	$G_{sl} = S_1 d_m^{0,9} F_a + S_2 d_m F_r$
Tapered roller bearings ¹⁾	$G_{rr} = R_1 d_m^{2,38} (F_r + R_2 Y F_a)^{0,31}$	$G_{sl} = S_1 d_m^{0,82} (F_r + S_2 Y F_a)$
For the axial load factor Y for single row bearings → product tables		
Spherical roller bearings	$G_{rr,e} = R_1 d_m^{1,85} (F_r + R_2 F_a)^{0,54}$	$G_{sl,e} = S_1 d_m^{0,25} (F_r^4 + S_2 F_a^4)^{1/3}$
	$G_{rr,l} = R_3 d_m^{2,3} (F_r + R_4 F_a)^{0,31}$	$G_{sl,l} = S_3 d_m^{0,94} (F_r^3 + S_4 F_a^3)^{1/3}$
	when $G_{rr,e} < G_{rr,l}$	when $G_{sl,e} < G_{sl,l}$
	$G_{rr} = G_{rr,e}$	$G_{sl} = G_{sl,e}$
	otherwise	otherwise
	$G_{rr} = G_{rr,l}$	$G_{sl} = G_{sl,l}$
CARB toroidal roller bearings	when $F_r < (R_2^{1,85} d_m^{0,78} / R_1^{1,85})^{2,35}$	when $F_r < (S_2 d_m^{1,24} / S_1)^{1,5}$
	$G_{rr} = R_1 d_m^{1,97} F_r^{0,54}$	$G_{sl} = S_1 d_m^{-0,19} F_r^{5/3}$
	otherwise	otherwise
	$G_{rr} = R_2 d_m^{2,37} F_r^{0,31}$	$G_{sl} = S_2 d_m^{1,05} F_r$

The values of geometric constants R and S for respective bearings are given in the SKF (2018).

4.2.1.3 Drag loss

The drag loss caused by the rotation of bearings inside an oil bath can influence the total frictional moment. The drag loss does not get influenced only by bearing speed, oil viscosity and oil level but also by the size and shape of the reservoir. The drag

loss in oil bath lubrication for ball bearings can be calculated as follows

$$M_{drag} = 0.4V_M K_{ball} d_m^5 n^2 + 1.093 \times 10^{-7} n^2 d_m^3 \left(\frac{nd_m^2 f t}{\nu} \right)^{-1.379} R_s \quad (4.9)$$

For roller bearing, the same can be estimated as follows

$$M_{drag} = 4V_M K_{roll} C_w B d_m^4 n^2 + 1.093 \times 10^{-7} n^2 d_m^3 \left(\frac{nd_m^2 f t}{\nu} \right)^{-1.379} R_s \quad (4.10)$$

The constants for the ball and roller bearings are defined below

$$K_{ball} = \frac{i_{rw} K_Z (d + D)}{D - d} 10^{-12} \quad (4.11)$$

$$K_{roll} = \frac{K_L K_Z (d + D)}{D - d} 10^{-12} \quad (4.12)$$

The value of the drag loss factor can be obtained from Figure 4.2.

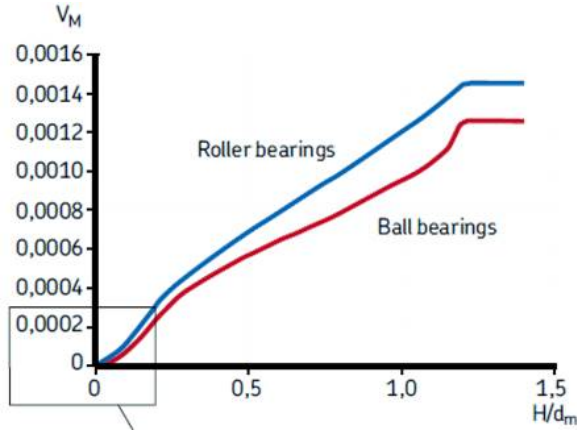


Figure 4.2: Drag loss factor (SKF, 2018)

where, B is the bearing width [mm], i_{rw} is the number of ball rows. The measurement of oil level H inside the bearing is shown in Figure 4.3. It is measured from the lowest contact point between the outer ring raceway and the rolling element.

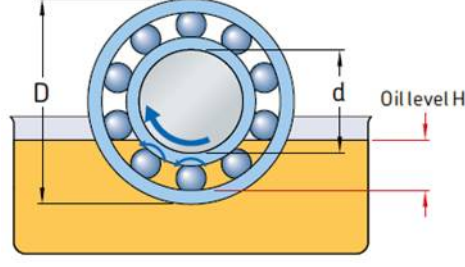


Figure 4.3: Bearing oil level (SKF, 2018)

The variable and functions are defined as follows

$$C_w = 2.789 \times 10^{-10} l_D^3 - 2.786 \times 10^{-4} l_D^2 + 0.0195 l_D + 0.6439 \quad (4.13)$$

$$l_D = 5 \frac{K_L B}{d_m} \quad (4.14)$$

$$f(t) = \begin{cases} \sin(0.5t) & \text{for } 0 \leq t \leq \pi \\ 1 & \text{for } \pi \leq t \leq 2\pi \end{cases} \quad (4.15)$$

$$R_s = 0.36 d_m^2 (t - \sin t) f_A \quad (4.16)$$

$$t = 2 \cos^{-1} \left(\frac{0.6 d_m - H}{0.6 d_m} \right) \text{ when } H > 1.2 d_m, \text{ use } H = 1.2 d_m \quad (4.17)$$

$$f_A = 0.05 \frac{K_Z (D + d)}{D - d} \quad (4.18)$$

4.2.2 Harris model

This model is developed by Harris and Kotzalas (2007) and presents an empirical model developed after extensive laboratory testing of different sizes of the bearings and the load acting on them. During the laboratory testing, the loads varied from light to heavy, while the shaft speed varied from slow to moderate. Various lubricants and lubrication methods were used during the tests to understand the effect of lubricant thermo-physical properties. The authors categorised total frictional moment into three components; one due to applied load, one due to viscous lubricant friction and another due to roller-end ring flange sliding friction.

4.2.2.1 Torque due to applied load

The torque due to the applied load is defined using the following equation

$$M_t = f_1 F_\beta d_m \quad (4.19)$$

where f_1 is a factor depending on the bearing design and relative bearing load, F_β is a factor which depends on the magnitude and direction of the applied load and d_m is the arithmetic mean of bearing inner and outer diameters [mm]. The value of f_1 for the ball bearing is calculated using the following equation

$$f_1 = Z \left(\frac{F_s}{C_s} \right)^y \quad (4.20)$$

where F_s is the static equivalent load [N] and C_s is the basic static load rating [N]. The following table gives appropriate values of Z and y .

Table 4.3: Values of Z and y (Harris and Kotzalas, 2007)

Ball bearing type	Nominal contact angle [°]	Z	y
Radial deep groove	0	0.0004-0.0006	0.55
Angular contact	30-40	0.001	0.33
Thrust	90	0.0008	0.33
Double row, self-aligning	10	0.0003	0.40

In the case of roller bearing, the values of f_1 can be obtained from Table 4.4.

Table 4.4: f_1 for cylindrical roller bearings (Harris and Kotzalas, 2007)

Roller bearing type	f_1
Radial cylindrical with cage	0.0002-0.0004
Radial cylindrical, full complement	0.00055
Thrust cylindrical	0.0015

The value of F_β depends on the magnitude and direction of the applied load. It

may be expressed in equation form as follows.

$$F_\beta = \begin{cases} \max(0.9F_a \cot \alpha - 0.1F_r, F_r) & \text{for ball bearings} \\ 3F_a - 0.1F_r & \text{for deep groove ball bearings} \\ F_a & \text{for thrust bearings} \\ \max(0.8F_a \cot \alpha, F_r) & \text{for cylindrical roller bearings} \end{cases} \quad (4.21)$$

4.2.2.2 Torque due to viscous lubricant friction

For the lubricated bearings, when lubricant occupies the free space between rolling elements and raceways, it creates resistance to the motion generating a frictional loss. This resistance is a function of the type of lubricant and its thermo-physical properties, lubricant level, speed and temperature of operation.

$$M_v = \begin{cases} 10^{-7} f_o (\nu_o n)^{2/3} d_m^3 & \text{if } \nu_o n \geq 2000 \\ 160 \times 10^{-7} f_o d_m^3 & \text{if } \nu_o n < 2000 \end{cases} \quad (4.22)$$

f_o is a factor depending on the type of bearing, and method of lubrication, while ν_o is the kinematic viscosity of lubricant [cSt]. The f_o for ball bearings can be obtained from Table 4.5 while for roller bearings, it can be obtained from Table 4.6.

Table 4.5: Values of f_o for ball bearing type and lubrication (Harris and Kotzalas, 2007)

Ball bearing type	Grease	Oil mist	Oil bath	Oil bath (vertical shaft) or oil jet
Deep-groove ball	0.7-2	1	2	4
Self-aligning ball	1.5-2	0.7-1	1.5-2	3-4
Thrust ball	2	1.7	3.3	6.6

Table 4.6: Values of f_o for cylindrical roller bearing type and lubrication (Harris and Kotzalas, 2007)

Bearing type	Grease	Oil mist	Oil bath	Oil bath (vertical shaft) or oil jet
Cylindrical roller with cage	0.6-1	1.5-2.8	2.2-4	2.2-4
Cylindrical roller full complement	5-10	-	5-10	-
Thrust cylindrical roller	9	-	3.5	8

4.2.2.3 Torque due to roller end-roller flange sliding friction

A few designs of cylindrical roller bearings have flanges either on the inner ring or on the outer ring. When these bearings are subjected to axial load in addition to radial load, they carry thrust load and frictional torque between roller end-ring flange sliding as given below

$$M_f = f_f F_a d_m \quad (4.23)$$

The value of f_f depends on the type of cylindrical roller bearing, lubricant and lubrication method and can be obtained from Table 4.7.

Table 4.7: Values of f_f for cylindrical roller bearings (Harris and Kotzalas, 2007)

Bearing type	Grease lubrication	Oil lubrication
With cage, optimum design	0.003	0.002
With cage, other designs	0.009	0.006
Full complement, single-row	0.006	0.003
Full complement, double-row	0.015	0.009

Total friction torque

An estimate of total friction torque is given as the sum of all frictional moments, which can be expressed as follows

$$M = \begin{cases} M_l + M_v & \text{for ball bearings} \\ M_l + M_v + M_f & \text{for roller bearings} \end{cases} \quad (4.24)$$

4.2.3 Palmgren model

The model proposed by Palmgren is based on an empirical approach which is developed after laboratory testing of different bearing types and sizes. Similar to the Harris model, the Palmgren model categorizes frictional torque into two parts, load-independent friction torque and load-dependent friction torque.

The load-independent friction torque M_o , when lubricated by oil, is shown in the following equation

$$M_o = \begin{cases} 1.5572 \times 10^{-6} f_o p d_m^3 & \text{if } \frac{\eta\omega}{p} < 2 \times 10^{-6} \\ 9.81 \times 10^{-3} f_o p d_m^3 \left(\frac{\eta\omega}{p}\right)^{2/3} & \text{if } \frac{\eta\omega}{p} \geq 2 \times 10^{-6} \end{cases} \quad (4.25)$$

When using grease lubrication, the load-independent friction torque can be calculated by

$$M_o = 9.81 \times 10^{-11} f_o (\nu\eta)^{2/3} d_m^3 \quad \text{if } \nu\eta \geq 2000 \quad (4.26)$$

While the load-dependent friction torque is given as follows

$$M_l = 0.0098 f_1 g_1 P_0 d_m \quad (4.27)$$

$$g_1 P_0 = 0.8 F_a \cot \alpha \geq F_r \quad (4.28)$$

The total friction torque is a sum of load-independent and load-dependent friction

torques as defined above and is given as

$$M = M_o + M_t \quad (4.29)$$

4.2.4 Comparison of predictions from SKF, Harris and Palmgren model

The section 2.2.3.4 presented power loss predictions of SKF, Harris and Palmgren models and their comparison with experimental results for roller as well ball bearings. Overall, analysing the results and comparison indicates, that for load-independent and load-dependent friction torque, the Harris model predictions fit well the experimental data for load-independent friction torque. However, none of the models, SKF, Harris, and Palmgren, best fit the load-dependent friction torque predictions except for low speeds, where Harris and Palmgren models' predictions are closer to the experimental data.

Three sizes of oil-injected, twin-screw compressors which are designed for 15-30 kW (size 1), 37-55 kW (size 2) and 75-160 kW (size 3) with "N" rotor profile, 4/5 lobe combination and L/D=1.55 are considered for the analysis. The male rotor diameters of size 1, size 2 and size 3 are 98 mm, 141 mm and 231 mm respectively. The comparison of bearing power loss for a pressure ratio of 8.5 for the bearings used in these compressors is presented in Table 4.8, 4.9 and 4.10. The bearing loads are obtained from SCORPATH (Stosic, 2005).

Table 4.8: Size 1: Bearing power loss predictions at 3,500 rpm

Location	Bearing	SKF	Harris	Palmgren
Male-Radial-Suction	NU 205 ECP	11	86	11
Female-Radial-Suction	NU 203 ECP	4	20	4
Male-Radial-Discharge	NU 205 ECP	13	88	13
Female-Radial-Discharge	NU 205 ECP	10	31	9
Male-Axial-Discharge	7305 BEP	30	779	18
Female-Axial-Discharge	7205 BEP	17	232	9
Total power loss [W]		86	1236	64

Table 4.9: Size 2: Bearing power loss predictions at 3,000 rpm

Location	Bearing	SKF	Harris	Palmgren
Male-Radial-Suction	NU 307 ECP	29	219	28
Female-Radial-Suction	NU 2304 ECP	10	46	7
Male-Radial-Discharge	NU 2207 ECP	37	207	28
Female-Radial-Discharge	NU 2207 ECP	28	78	21
Male-Axial-Discharge	7407 BEP	78	1876	50
Female-Axial-Discharge	7207 BEP	42	525	21
Total power loss [W]		223	2950	156

Table 4.10: Size 3: Bearing power loss predictions at 3,000 rpm

Location	Bearing	SKF	Harris	Palmgren
Male-Radial-Suction	NU 213 ECP	125	1006	117
Female-Radial-Suction	NU 1009 ECP	32	203	31
Male-Radial-Discharge	NU 211 ECP	99	846	96
Female-Radial-Discharge	NU 211 ECP	74	298	75
Male-Axial-Discharge	7311 BECBP	321	8317	132
Female-Axial-Discharge	7211 BEP	184	2243	75
Total power loss [W]		835	12912	527

From the above comparison and experimental results presented in the literature, it is understood that the SKF and Palmgren models underestimate the bearing power loss. So it can be concluded that within the acceptable range from the experimental results, the Harris model can be used for roller and ball bearing friction torque predictions.

4.3 Oil Drag Loss

Oil injection into a compressor serves three primary purposes: cooling the compressed gas, sealing clearances, and providing lubrication to the rotors and bearings. The introduction of oil yields notable isothermal efficiency due to the cooling effect it imparts. However, the benefits of cooling are counteracted by frictional losses attributed to bearings, shaft seals, and oil drag, all of which collectively contribute to a considerable reduction in the overall adiabatic efficiency.

Within the context of a twin-screw compressor, three distinct clearances play a pivotal role in the shearing of oil: radial clearance, interlobe clearance, and axial clearance. The radial clearance materializes between the outer diameter of the rotors and the housing bore diameter within which the rotors rotate. In contrast, the interlobe clearance emerges between the lobes of two inter-meshing rotors. At the high-pressure discharge end of the compressor, the axial clearance is maintained

between the side end faces of the rotor and the housing. A visual representation of these diverse clearances, all of which contribute to oil shearing within the twin-screw compressor, is depicted in Figure 4.4.

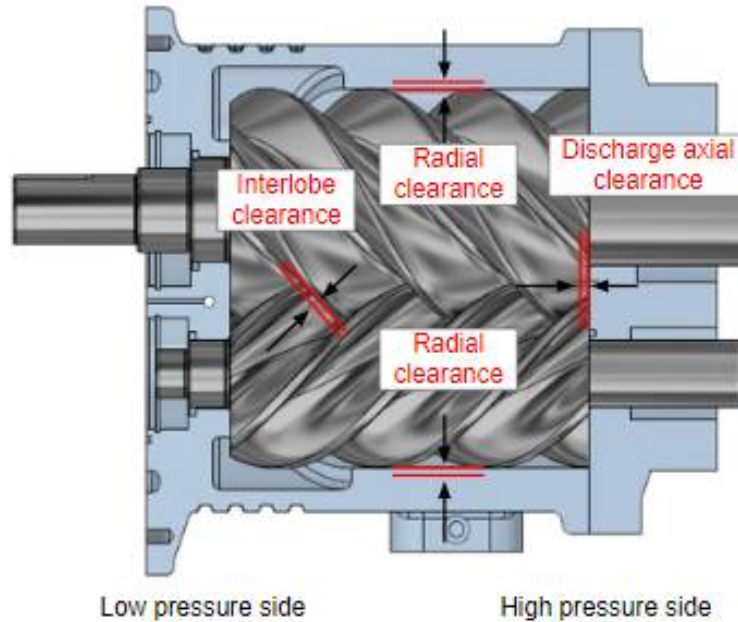


Figure 4.4: Different clearances within the screw compressor

In the context of these clearances, the interaction of oil takes place, resulting in shear forces between the distinct gaps as described earlier. This phenomenon of shearing leads to drag, a significant contributor to power loss. Hence, quantifying this drag becomes imperative to achieve a more precise performance projection. This section outlines an analytical model formulated to predict the drag loss attributed to the presence of oil.

The optimization of clearances is pivotal to achieve heightened efficiency. Nevertheless, the extent of tightening is constrained by the machining tolerances and the necessity for facile assembly. Within these clearances, the flow of oil experiences drag forces, arising from both inertia and pressure-induced flow effects. The inertia force, engendered by the rotational motion of the rotors, is transferred to the adjacent layers of fluid. Concurrently, the progression of the rotors generates a differential pressure force, exerted on the fluid residing within the clearances. It's worth noting that this pressure-induced force acts in opposition to the direction of the inertial force.

During the exploration of differential analysis in fluid dynamics, the flow domain within the clearances of screw compressors can be likened to a combined Couette and Poiseuille flow phenomena (Cengel and Cimbala, 2013). Consequently, a composite Couette-Poiseuille model has been adopted for the purpose of modelling the oil flow within these clearances. The velocity profiles, illustrating the characteristics of Couette flow that symbolize inertial forces and Poiseuille flow that incorporate pressure-induced flow, are depicted as the initial two curves in Figure 4.5.

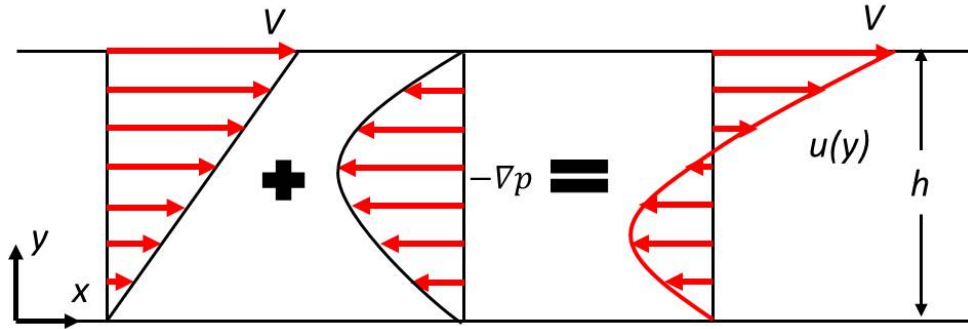


Figure 4.5: Couette-Poiseuille velocity profile

At an ordinate value of zero on the abscissa, a stationary boundary is representative of either the housing or the relative position of the rotor. Conversely, at an ordinate value of h , the abscissa corresponds to a boundary associated with the motion of the rotor. The culmination of these characteristics gives rise to a composite velocity profile for the combined flow, which is depicted by the rightmost curve denoted as $u(y)$.

The analytical method presents several advantages in contrast to numerical techniques, notably encompassing significantly reduced computation times and a clearer visualisation of the underlying physical principles that govern flow processes. Furthermore, the existing literature landscape concerning drag loss inadequately addresses the quantified evaluation of drag loss traversing diverse clearance pathways within the compression chamber. This evaluation is typically rendered as an approximation. Additionally, employing minimal geometric and operational inputs specific to the compressor, an insightful comprehension of the impact of drag loss can be foreseen via a simplified analytical approach.

Considering the quantifiable influence of drag loss upon the comprehensive per-

formance of a screw compressor, an approximative analytical model addressing drag loss emerges as a valuable method for broader-level investigation. This analytical framework, in conjunction with parametric analysis outcomes, equips designers with first-hand insights, thereby facilitating the meticulous optimization of compressor designs.

The Navier-Stokes equations can be precisely solved through analytical techniques, under the condition of several key assumptions. The analytical model is formulated based on the following underlying assumptions:

- The planar representation of Couette-Poiseuille flow is considered.
- The flow is steady with the radial clearance gaps completely filled with oil.
- The fluid is incompressible and Newtonian with constant properties.
- Absence of flow in the y and z directions.

The rationale behind adopting the assumption of a planar representation for radial flow is rooted in the significant difference in scale between the curvature radius of the housing and the maintained clearances. Specifically, the housing's curvature radius is orders of magnitude larger than the clearances. Additionally, due to the comparatively elevated viscosity of the oil and the characteristic dimensions (clearances) on the micrometer scale, the flow within the clearance gaps invariably remains laminar. As a result, this analytical model is most applicable to fluids with high viscosity, such as oil, while being limited in its use for other types of fluids.

In the process of modelling drag loss, the initiation of the effective shearing length for oil is taken into account starting from the injection point. This, coupled with the complete filling of the clearance gaps, provides a rationale for assuming the absence of interaction between the leakage flows of air and oil in the clearance gaps. Notably, due to the higher density of oil compared to air, the centrifugal force exerted on the oil by the rotating rotors is more pronounced. An illustrative numerical investigation conducted by Basha et al. (2018) provides insight into this phenomenon. The study presents a depiction of the oil volume fraction on a cross-sectional plane within the twin-screw compressor upon injection. The findings affirm that the clearance gaps

between the rotor tip and the inner diameter of the housing are entirely occupied by oil, as illustrated in Figure 4.6.

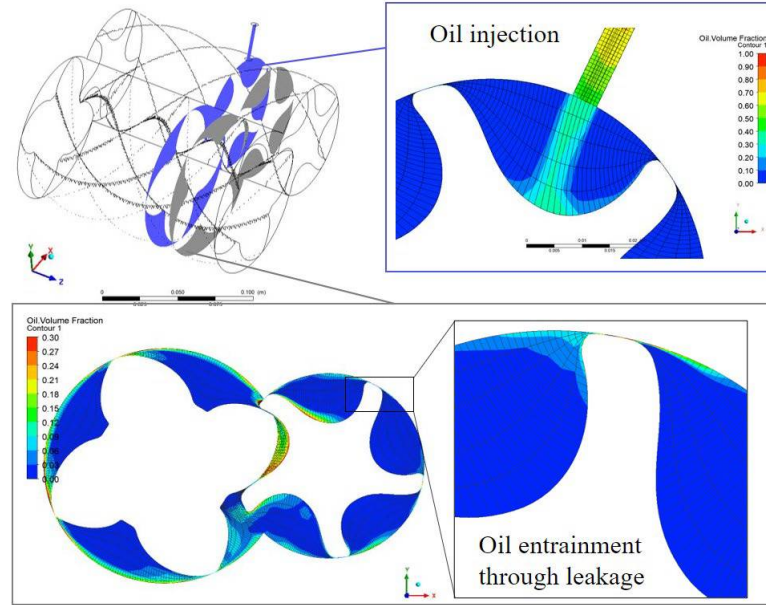


Figure 4.6: Oil volume fraction on a cross-sectional plane in the twin-screw compressor at injection (Basha et al., 2018)

A crucial assumption supporting the analysis is the complete filling of the radial clearance gap with oil. However, a departure from this assumption is modelled on the discharge axial side, where the clearance gap is defined as a function of the oil-to-gas mass ratio. This distinctive approach allows in capturing the real-world behaviour, wherein adjustments in oil flow rate introduce considerable variations in the compressor’s performance, specifically in terms of drag losses.

By factoring in the oil-to-gas mass ratio and its influence on the clearance gap on the discharge axial side, the analysis becomes more attuned to the dynamic interaction between oil flow and the resultant drag losses. This level of detail contributes to a more accurate representation of the compressor’s behaviour, especially as it pertains to the intricate relationship between oil distribution and drag loss.

The conservation of mass equation reduces to the following form

$$\frac{\partial u}{\partial x} + \frac{\partial v}{\partial y} + \frac{\partial w}{\partial z} = 0 \quad \longrightarrow \quad \frac{\partial u}{\partial x} = 0 \quad (4.30)$$

Similarly, the momentum equation takes the below form

$$\rho \left(\frac{\partial u}{\partial t} + u \frac{\partial u}{\partial x} + v \frac{\partial u}{\partial y} + w \frac{\partial u}{\partial z} \right) = -\frac{\partial p}{\partial x} + \rho g_x + \mu \left(\frac{\partial^2 u}{\partial x^2} + \frac{\partial^2 u}{\partial y^2} + \frac{\partial^2 u}{\partial z^2} \right) \quad (4.31)$$

$$\frac{d^2 u}{dy^2} = \frac{1}{\mu} \frac{dp}{dx} \quad (4.32)$$

Using the conservation laws for mass and momentum, the velocity profile takes the following form

$$u = \frac{1}{2\mu} \frac{dp}{dx} y^2 + C_1 y + C_2 \quad (4.33)$$

After applying boundary conditions at the rotor tip and inner housing surfaces, the velocity profile takes the following form

$$u = \frac{Vy}{h} + \frac{1}{2\mu} \frac{dp}{dx} (y^2 - hy) \quad (4.34)$$

After substituting this velocity profile in the shear stress equation, the shear stress can be calculated as

$$\tau = \mu \frac{du}{dy} \quad \longrightarrow \quad \tau = \frac{\mu V}{h} + \frac{h}{2} \frac{dp}{dx} \quad (4.35)$$

The determination of pressure gradient, essential for the calculation of shear stress, is derived from a chamber model that is numerically solved as documented in Stosic (2005). This model provides the necessary pressure gradient information. For each rotation angle of the rotor, the pressure variation is computed, and this value is subsequently divided by the discretised length of the clearance gap, which is equally divided.

In order to verify and validate the model, the pressure variation is recorded for various discharge pressure ratings. This comparison helps ensure that the model aligns well with experimental data, thereby confirming its accuracy and reliability in capturing the pressure gradients essential for shear stress calculations.

Ultimately, the torque required to overcome the shear stress and power loss is given by

$$T = \tau Ar \quad (4.36)$$

To compute the shear flow region within the radial clearance, the analysis involves

the product of the top land width of the rotors, the lead, and the number of lobes. This particular shear flow region within the radial clearance is visually depicted in Figure 4.7, highlighted as the area along the outer diameter of the female rotor.

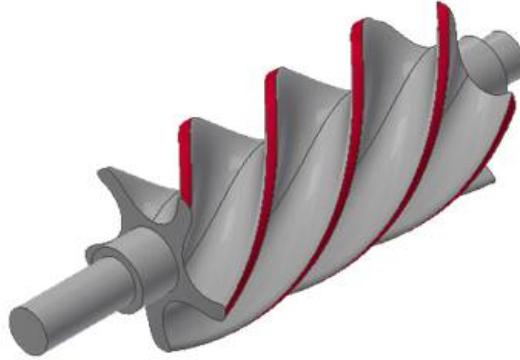


Figure 4.7: Shear flow region for radial clearance

Given the radial alteration in velocity boundary conditions along the high-pressure side axial clearance, the calculation of shear stress and frictional torque involves the consideration of two distinct areas: the tip velocity at the pitch circle radius and the circular region encompassing the pitch circle of the rotor. Due to the non-symmetric profile of the rotor on its end face, the circular area encompassing the pitch circle is designated as the shear flow region. This specific region for shearing within the axial clearance is clearly identified by the highlighted annular area on the rotor's end face, as visually depicted in Figure 4.8.

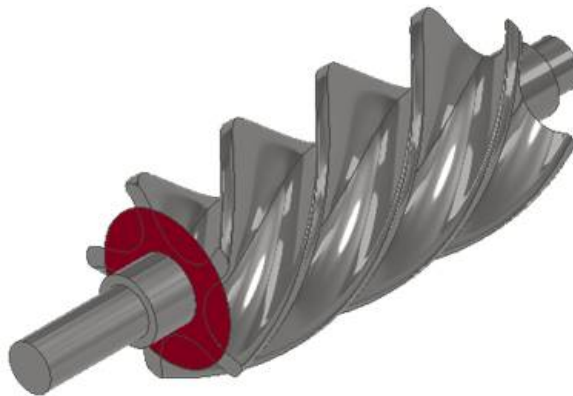


Figure 4.8: Shear flow region for axial clearance

To establish the shear flow region pertinent to the interlobe clearance, the zone subjected to shear stress is defined by the product of the sealing line length and the clearance length. The sealing line length, a key parameter, is illustrated in Figure

4.9, while the clearance length, equivalent to the width of the top land of the rotor, is depicted in Figure 4.7. The calculation of the sealing line length is accomplished by plotting the locus of contact points between the male and female rotors throughout one complete revolution. Subsequently, the arc length of this locus is computed numerically and can be obtained using the SCORPATH software (Stosic, 2005).

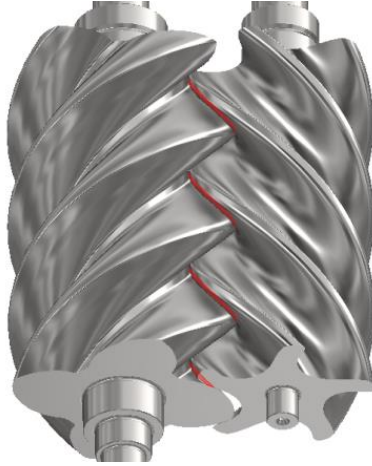


Figure 4.9: Shear flow region for interlobe clearance

The shaft power can be calculated from the obtained shear stress and shaft speed using the following equation

$$P = \frac{2\pi NT}{60} \quad (4.37)$$

The outcomes derived from this model, along with the subsequent parametric analysis, shed light on the influence of various factors on drag loss. These factors include compressor sizes, rotational speeds, pressure ratios, oil viscosities, and clearance sizes. The presentation and examination of these predictions and parametric analyses constitute the content of the forthcoming chapter.

4.4 Summary

Within this specific chapter, a comprehensive study of power loss prediction models is introduced, each tailored to the unique components of an oil-flooded twin-screw compressor. The components identified as pivotal contributors to power loss encompass rolling element bearings, shaft seals, oil drag loss, and gears.

The forecast of bearing power loss is approached through an evaluation of method-

ologies advocated by SKF (SKF, 2018), Harris (Harris and Kotzalas, 2007), and Palmgren (Tu, 2016). The predictions generated by these methods, specifically addressing roller and ball bearings, are aligned with empirical findings from existing literature. The implementation of these prediction methods is executed through MATLAB (2022), with comprehensive programming details furnished in Appendices A, B, and C. It is noteworthy that these bearing power loss projections span compressors of varying sizes, designed for power ratings ranging from 15 to 160 kW. A meticulous comparison of these predictions against experimental observations of total shaft power reveals that the Harris model, when coupled with power loss projections for shaft seals and oil drag, closely aligns with experimental data. A comprehensive exposition of this comparison is presented in Chapter 6, thus advocating for the adoption of the Harris model for rolling element-bearing power loss prediction.

For the drag loss estimation, an amalgamated Couette-Poiseuille flow model is formulated utilizing analytical techniques (Abdan et al., 2022). This model facilitates the deconstruction of drag loss contributions stemming from distinct clearance pathways, encompassing axial, radial, and interlobe clearances. Moreover, it accommodates parametric analysis aimed at uncovering the influences of compressor size, tip speed, and pressure ratio. The computational framework, established within the scope of MATLAB (2022), is outlined in Appendix E.

Adhering to the principles outlined in Chapter 2, the computation of shaft seal power loss amalgamates a semi-analytical method, empirical equations, and empirical measurements, as advanced by Frölich et al. (2014) and Engelke (2011). A detailed breakdown of the calculation steps pertinent to this method is expounded upon in Appendix D. Simultaneously, the determination of power loss attributed to gears adheres to the methodology prescribed by Jelaska (2012), as elaborated upon in Chapter 2. This method inherently differentiates between power loss during loaded operation and power loss during idle gear motion. Notable factors influencing gear power loss encompass transmitted power and loads, gear ratio, mean coefficient of friction, lubrication type and level, and lubricant properties.

Chapter 5

Case Studies and Parametric Analysis

5.1 Introduction

Building upon the methods presented in the preceding chapter, this section encompasses the calculation of the comprehensive mechanical power loss within the oil-injected, twin-screw compressor. The totality of mechanical power loss encapsulates the combined effects of power loss through bearings, the radial shaft seal, oil drag, and gears. Furthermore, this chapter delves into a parametric analysis, exploring the influence of specific geometric and operational parameters on the magnitude of mechanical loss. This exploration enhances comprehension of how variations in these parameters impact the overall mechanical power loss within the compressor system.

5.2 Case Study on Bearing Power Loss

5.2.1 Oil injected compressor

Three sizes of oil-injected, twin-screw compressors which are designed for 15-30 kW (size 1), 37-55 kW (size 2) and 75-160 kW (size 3) with “N” rotor profile, 4/5 lobe combination and $L/D=1.55$ are considered for the analysis. The male rotor diameters of size 1, size 2 and size 3 are 98 mm, 141 mm and 231 mm respectively.

As concluded in the previous chapter, the Harris model is better suited to calcu-

late power loss through the bearings. Table 5.1 lists the rolling element bearings used in the compressors mentioned above with their location of use. The radial and axial loads generated during compression are obtained from the SCORPATH software package.

Table 5.1: Bearings used in screw compressors

Location	size 1	size 2	size 3
Male-Radial-Suction	NU 205 ECP	NU 307 ECP	NU 213 ECP
Female-Radial-Suction	NU 203 ECP	NU 2304 ECP	NU 1009 ECP
Male-Radial-Discharge	NU 205 ECP	NU 2207 ECP	NU 211 ECP
Female-Radial-Discharge	NU 205 ECP	NU 2207 ECP	NU 211 ECP
Male-Axial-Discharge	7305 BEP	7407 BEP	7311 BECBP
Female-Axial-Discharge	7205 BEP	7207 BEP	7211 BEP

5.2.1.1 Type and magnitude of the load

The different types of load and their magnitude acting on different bearings positioned inside the oil-injected, twin-screw air compressor of size 2 for a pressure ratio of 8.5 and 30 m/s speed of male rotor speed are shown in Figure 5.1.

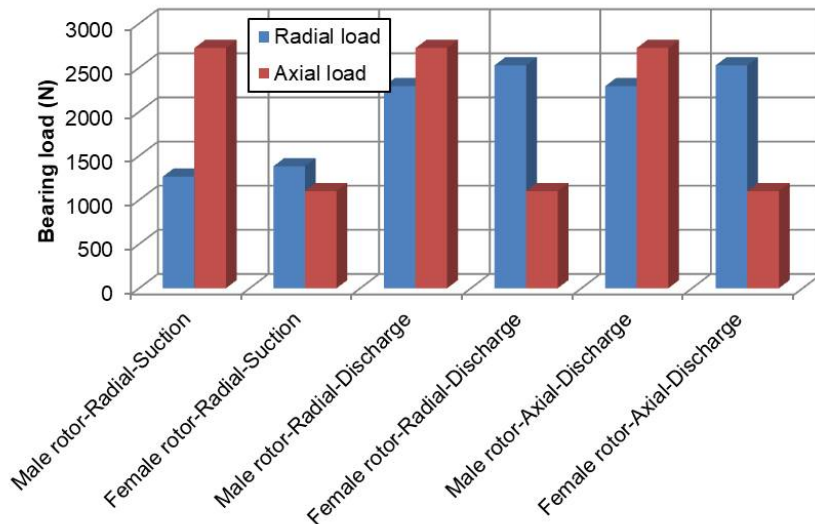


Figure 5.1: Type and magnitude of the load on different bearings

The cylindrical roller bearings take only radial load, while axial bearings take only axial load. The frictional power loss in these bearings for the above-mentioned operating and load conditions is presented in Figure 5.2.

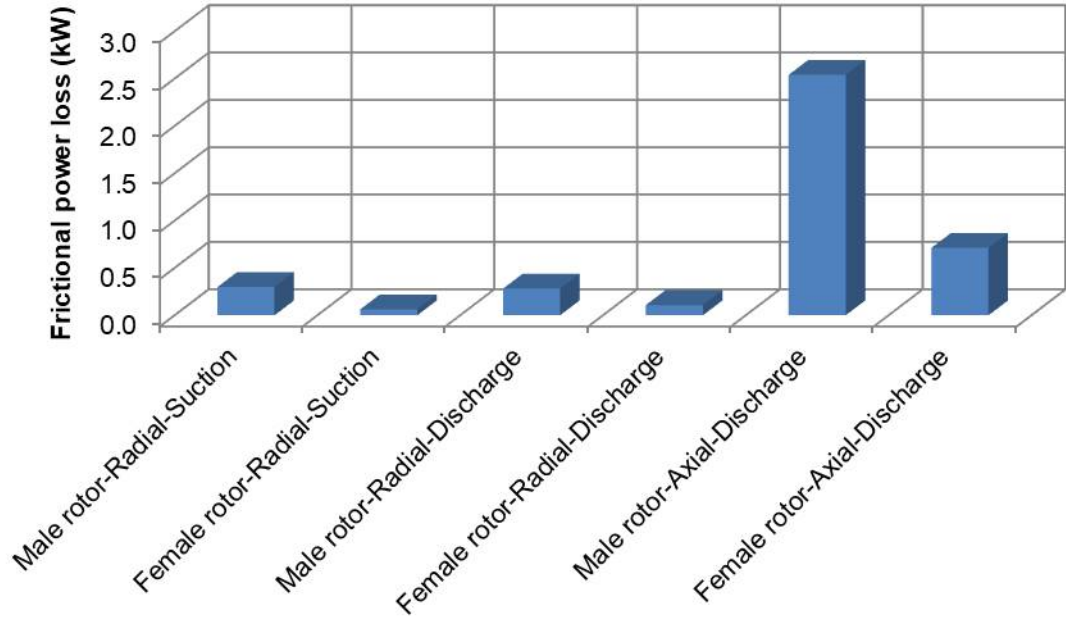


Figure 5.2: Frictional power loss in bearings

Compared to the radial bearings, the axial bearings show higher frictional power loss.

5.2.1.2 Effect of pressure ratio and shaft speed

The effect of pressure ratio on bearing power loss with respect to speed is shown in Figure 5.3. The calculations are done for the size 2 compressor.

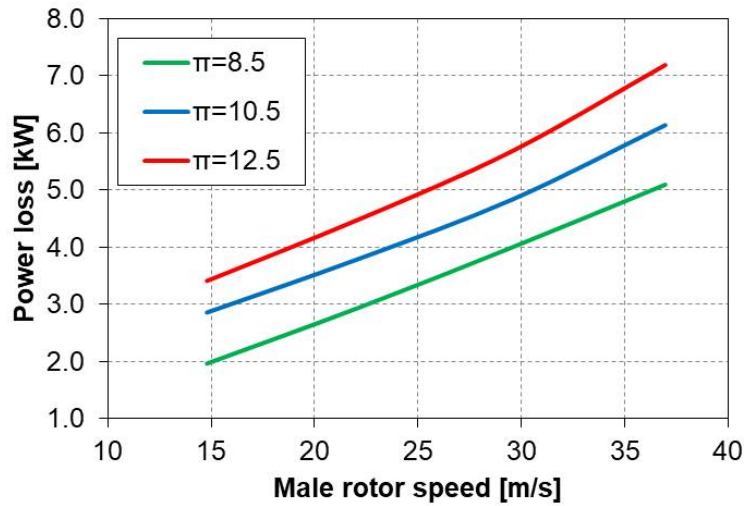


Figure 5.3: Effect of pressure ratio and speed on bearing power loss

It is seen that the total frictional power loss of the compressor bearings increases almost linearly with the pressure ratio and the speed of the bearings.

5.2.1.3 Effect of size and load

The effect of pressure ratio and shaft speed on bearing power loss for different sizes of compressor bearings is shown in Figure 5.4. With the increase in the size of the bearing, shaft speed and compression pressure ratio, the power loss in the bearings increases.

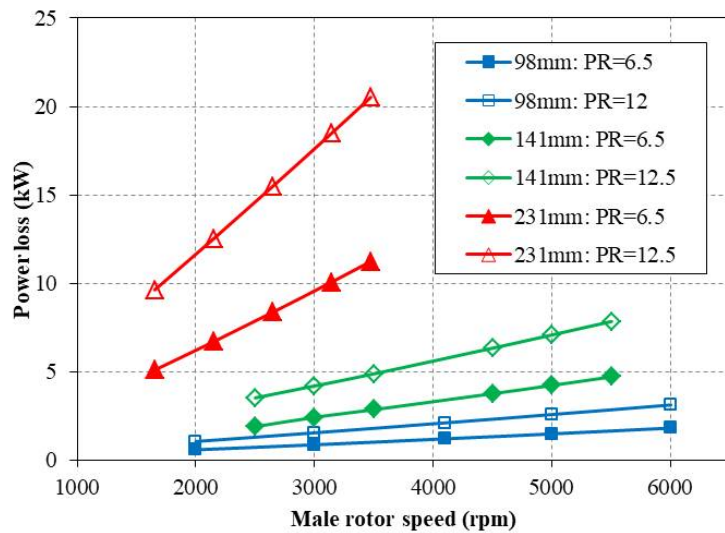


Figure 5.4: Oil injected bearings power loss

With the increase in the size of the compressor and ultimately the bearings,

the power loss increases because of larger frictional surface areas. The frictional power loss due to increased pressure ratio or loads on bearings shows a significant contribution to the bigger size compressors than the smaller size compressors.

5.3 Case Study on Radial Shaft Seal Power Loss

Using the method proposed in the previous chapter, the parametric analysis is carried out to understand the effects of radial force, shaft diameter, shaft surface roughness, shaft speed and oil temperature. A shaft seal with nitrile rubber (NBR) material exerts a mean radial force of 145.9 N/m while the FKM material seal exerts a mean radial force of 100 N/m (Engelke, 2011). A shaft/seal-inner diameter of 75 mm, a rotational speed of 3000 rpm, a surface roughness of 1.6 micrometres and a contact temperature of 333 K is considered for the calculation.

5.3.1 Effect of shaft speed

The seal frictional power loss increases linearly with respect to the shaft speed as shown in Figure 5.5. Since the radial force exerted by the nitrile rubber is more, it contributes more to power loss than the FKM seal.

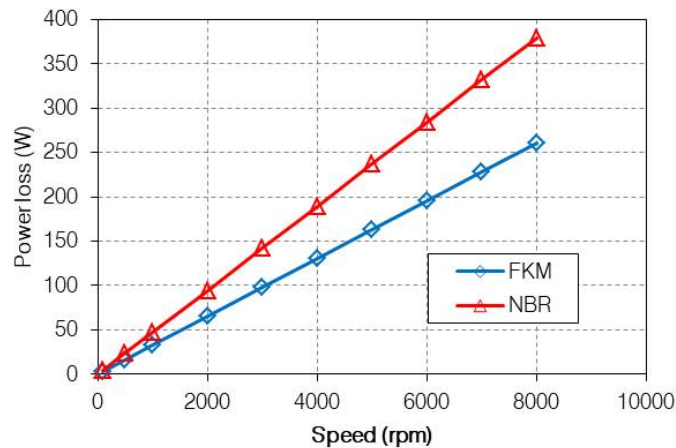


Figure 5.5: Seal power loss v/s shaft speed

5.3.2 Effect of shaft diameter

The shaft size is directly proportional to the radial force exerted by the seal. As the shaft size increases, the seal frictional power loss increases, as shown in Figure 5.6.

The increase in frictional power loss is a non-linear curve.

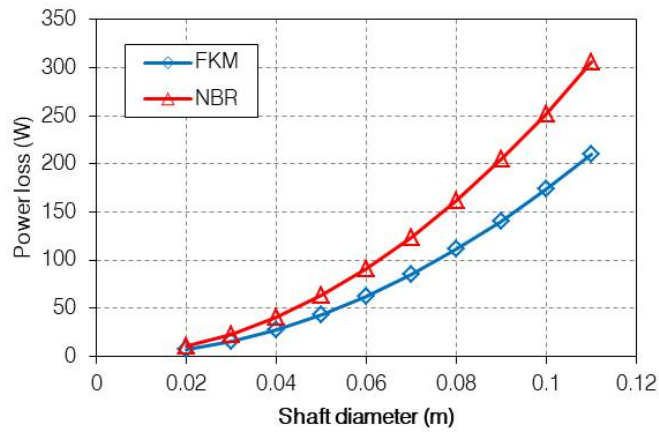


Figure 5.6: Seal power loss v/s shaft diameter

5.3.3 Effect of surface roughness

The effect of shaft surface roughness on the frictional power loss of the seal is shown in Figure 5.7. The frictional power loss does not change much with respect to shaft surface roughness. However, it does affect the seal's performance. Higher shaft surface roughness creates more passages for oil to escape, resulting in oil leakage through the seal.

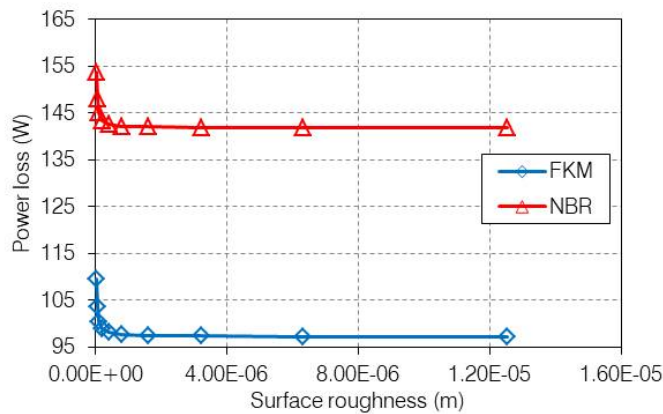


Figure 5.7: Seal power loss v/s shaft surface roughness

5.3.4 Effect of oil temperature

The effect of oil temperature on the seal's frictional power loss is presented in Figure 5.8.

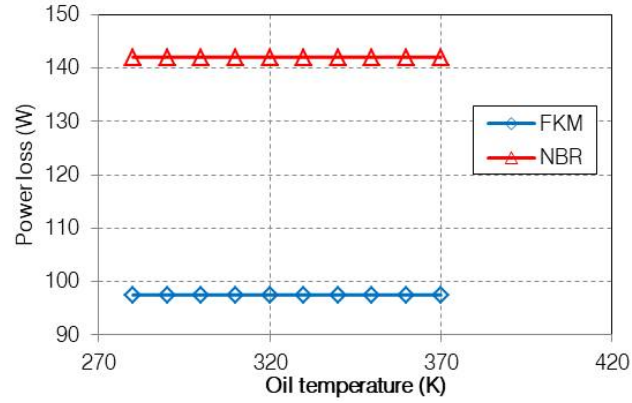


Figure 5.8: Seal power loss v/s oil temperature

No effect of oil temperature on the seal’s frictional power loss in the operating range from 270 K to 370 K is seen.

5.4 Case Study on Oil Drag Loss

5.4.1 Effect of compressor size

This section presents the outcomes derived from the analytical model for drag loss pertaining to the three distinct compressor sizes. The impact of speed variations on each component of drag loss is vividly illustrated in Figure 5.9 (a), (b), and (c) for compressors of size 1, 2, and 3, respectively, when operating at a pressure ratio of 8.5. This graphical representation provides a tangible insight into the behaviour of drag loss components in response to changes in operating speeds for the specified compressor sizes.

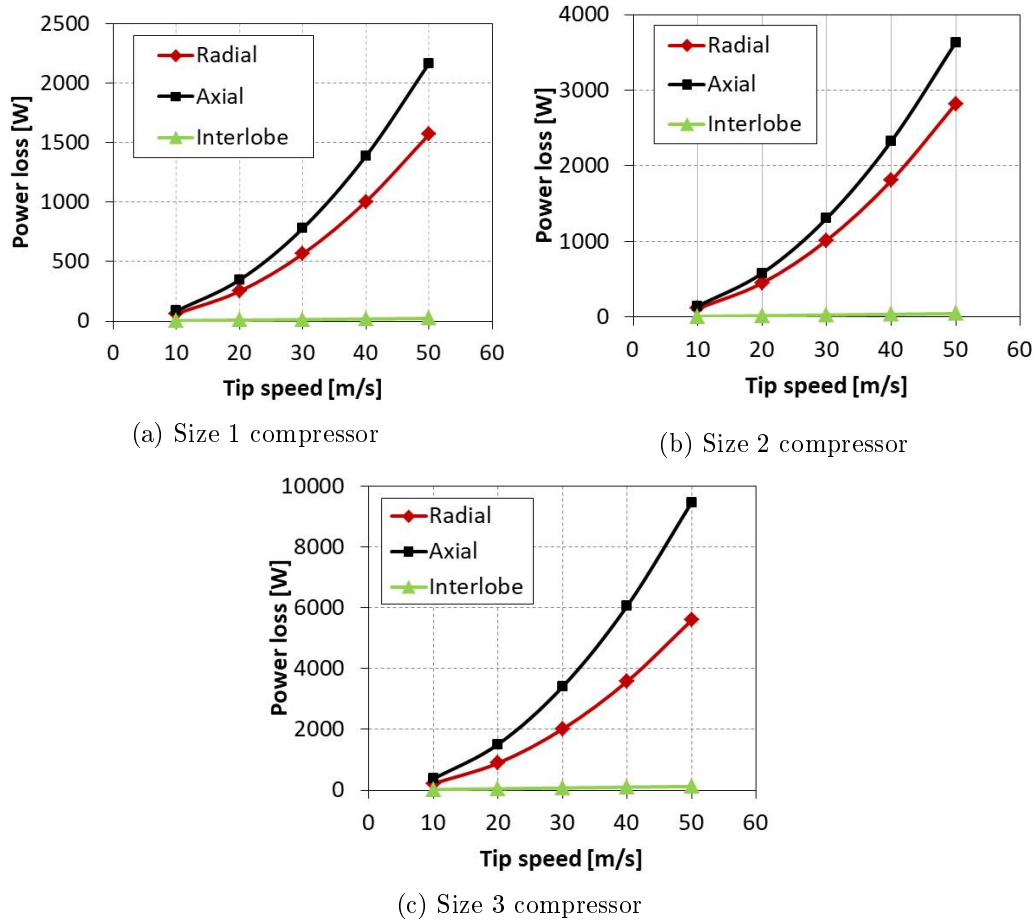


Figure 5.9: The effect of different sizes of the screw compressor on drag loss elements with respect to speed

In the context of all three compressors, a consistent trend emerges where the axial drag loss component accounts for approximately 55% of the total drag loss. The radial drag loss element contributes to around 43%, while the drag originating from the interlobe clearance remains notably low, hovering around 1-2%. This distribution underscores the significant influence of axial and radial clearances in driving drag loss within the compressor system.

This pronounced axial and radial contributions to drag loss can be attributed to several factors. Primarily, the axial and radial clearances at the discharge end and larger shear area experiences heightened shear flow regions along with substantial pressure gradients. These characteristics create an environment conducive to elevated drag loss in comparison to the interlobe clearance. This phenomenon aligns well with empirical observations that underscore the substantial effect of the axial and radial gaps on the volumetric flow rate of the compressor.

5.4.2 Effect of pressure ratio

A comprehensive parametric analysis was conducted to ascertain the impact of pressure ratio (π), oil viscosity, and clearance values on each constituent element comprising the total drag loss. For the size 2 compressor, drag loss was evaluated for operation at pressure ratios of 8.5, and 12.5 across a range of speeds. The corresponding effects are graphically presented for each individual drag loss element in Figure 5.10 (a), (b), and (c).

The results reveal distinctive trends: the radial and axial components of drag loss exhibit a non-linear increase with speed, while the interlobe element displays a linear rise with speed. This differential behaviour underscores the complex interactions of various parameters on the distinct components of drag loss.

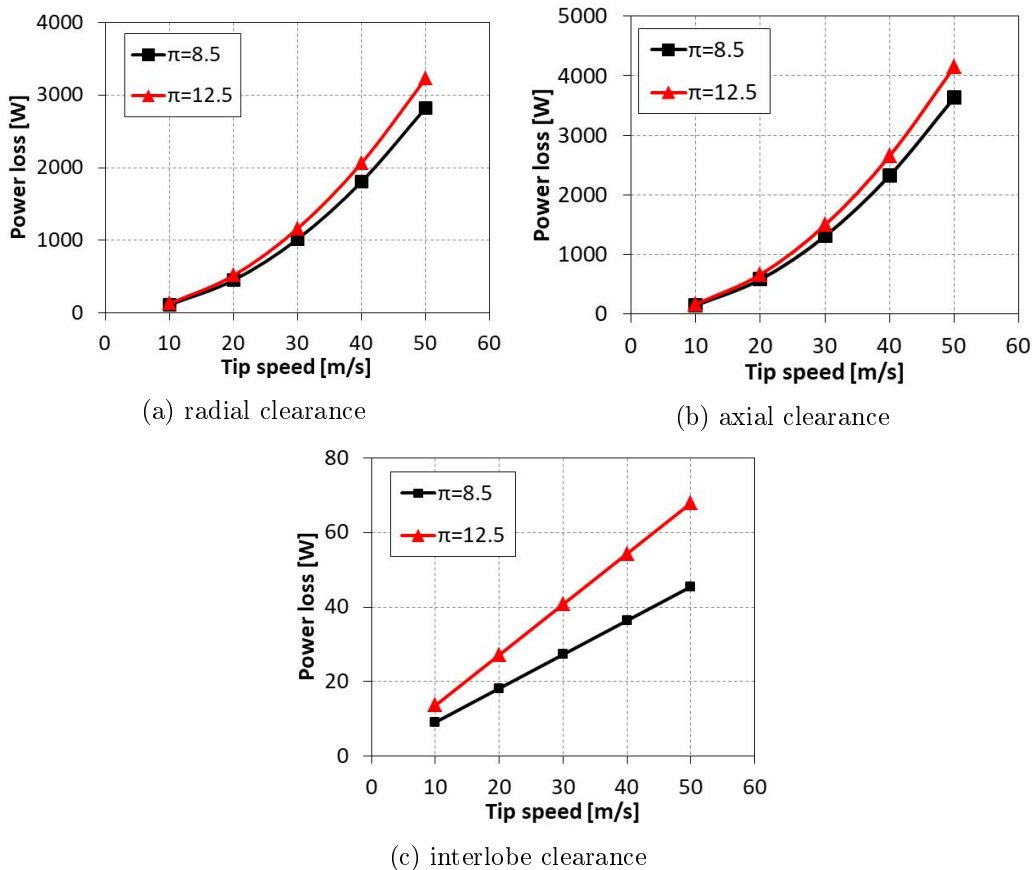


Figure 5.10: Effect of pressure ratio on drag loss with respect to speed for size 2 compressor

Additionally, it is evident that the pressure ratio exerts a modest influence on the radial and axial drag loss elements. This manifests in an approximately 14% increase

in drag loss when the pressure ratio transitions from 8.5 to 12.5. However, for the same alteration in pressure ratio, the interlobe drag loss element demonstrates a much more pronounced response, resulting in a 33% escalation in drag loss. This disparity in the impact of pressure ratio on different drag loss components underscores the varying sensitivities of these elements to operational changes.

5.4.3 Effect of oil viscosity

The analysis confirms that oil with higher viscosity imparts greater resistance to the flow, resulting in elevated losses. The findings clearly demonstrate that the total drag loss escalates in tandem with an increase in oil viscosity, as depicted in Figure 5.11. This alignment with practical behaviour reinforces the understanding that higher oil viscosity indeed leads to heightened drag loss.

It is notable that the percentage increase in drag loss is more pronounced for larger compressors. This observation underscores the fact that the influence of oil viscosity on drag loss is more pronounced in larger compressor systems, potentially due to the more intricate flow dynamics and greater clearance volumes inherent to larger configurations.

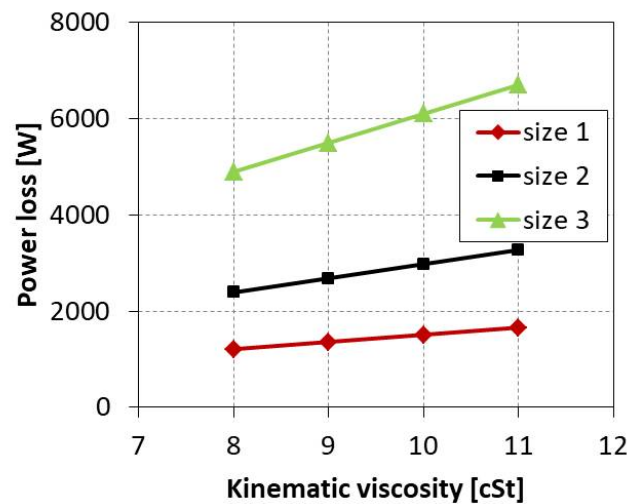


Figure 5.11: Effect of oil viscosity on drag loss for different sizes of compressors and pressure ratio 8.5

The selection of distinct clearances tailored to the varying sizes of the compressors leads to divergent leakage areas available for oil shearing. This variation in clearance dimensions directly influences the magnitude of drag losses incurred. This

phenomenon is noticeably illustrated in Figure 5.11, where it becomes evident that larger compressor sizes maintain larger leakage areas, consequently resulting in higher drag losses compared to smaller compressor sizes.

This trend highlights the intricate relationship between clearance design, leakage areas, and drag loss, ultimately contributing to the performance disparities observed across compressors of varying sizes.

5.4.4 Effect of various clearances

The effect of various clearances on the drag loss in the radial, axial and interlobe elements for the size 2 compressor is shown in Figure 5.12 (a), (b), and (c), respectively, when operating at a pressure ratio of 8.5.

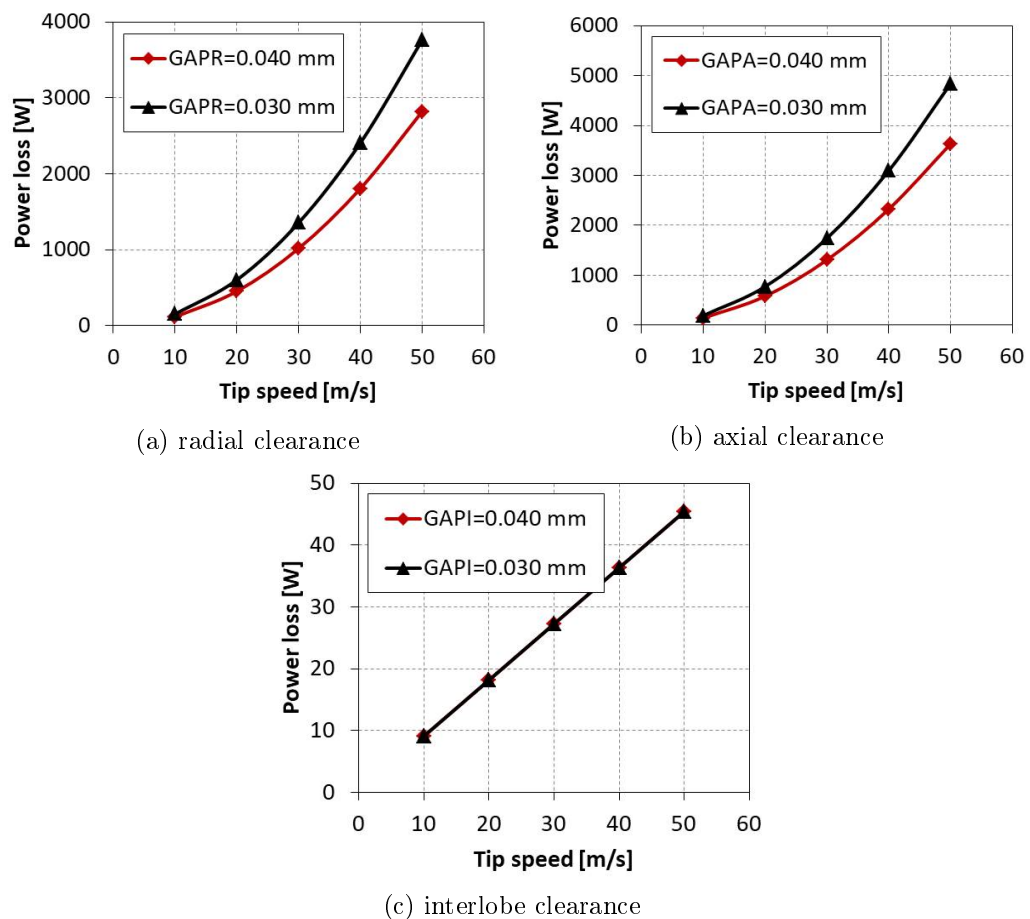


Figure 5.12: Effect of various clearances on drag loss at pressure ratio 8.5 with speed for size 2 compressor

The alterations in clearance dimensions exert a more pronounced impact on the radial and axial drag loss components compared to the interlobe element. Specifically,

the radial and axial elements display a substantial decrease in drag loss, amounting to nearly 25%, when the respective clearances are augmented from 0.030 mm to 0.040 mm. In contrast, the impact on the interlobe drag loss element is comparatively marginal when its clearance increases from 0.030 mm to 0.040 mm.

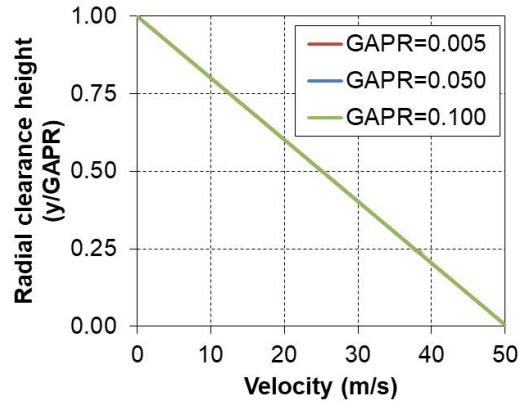
This discrepancy underscores the differential sensitivity of these drag loss components to changes in clearance dimensions. It further emphasizes the significance of meticulous clearance design in managing and optimizing drag losses within the compressor system.

5.4.5 Comparison of Couette and Poiseuille flow in clearance

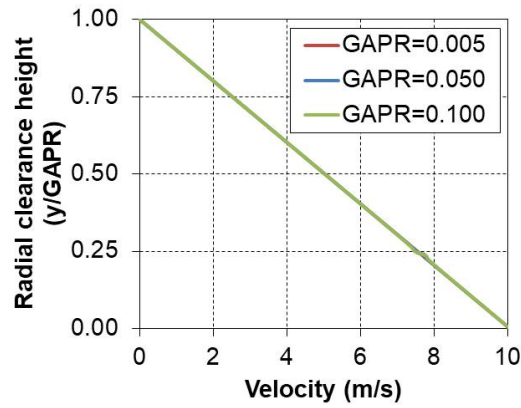
5.4.5.1 Effect of tip speed and radial clearance

This section is dedicated to describe the influence of tip speeds, radial clearances, and pressure ratios on the velocity profile within the radial clearance.

In Figure 5.13, the x-axis corresponds to the male rotor tip speed, while the y-axis depicts the normalized radial clearance. The x-axis value at $y/\text{GAPR}=0$ corresponds to the male rotor tip speed, while the x-axis value at $y/\text{GAPR}=1$ corresponds to the housing surface. This graphical representation facilitates a visual understanding of the alterations in velocity distribution across varying tip speeds and radial clearances, lending insights into the interplay between Couette and Poiseuille flows.



(a) Tip speed 50 m/s



(b) Tip speed 10 m/s

Figure 5.13: Effect of tip speed and radial clearance on drag loss

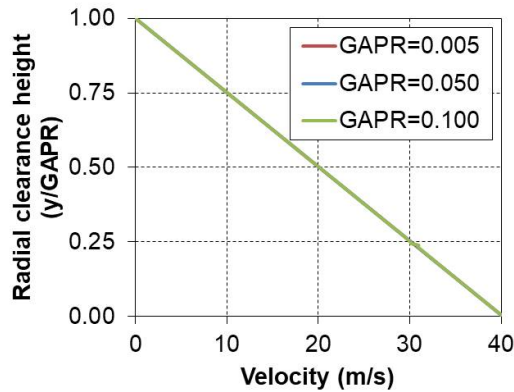
In the context of a tip speed of 50 m/s and a pressure ratio of 8.5, as depicted in Figure 5.13 (a), the impact of radial clearance gap variation appears negligible. Similarly, when the tip speed is reduced to 10 m/s, maintaining the same pressure ratio of 8.5, the radial clearance does not exhibit the signs of Poiseuille flow effects, as illustrated in Figure 5.13 (b). Consequently, the prevailing flow dynamics are predominantly characterized by the Couette type of flow.

This observation underscores the pivotal role that tip speed plays in shaping the flow behaviour within the radial clearance, and subsequently, the dominance of either Couette or Poiseuille flow dynamics.

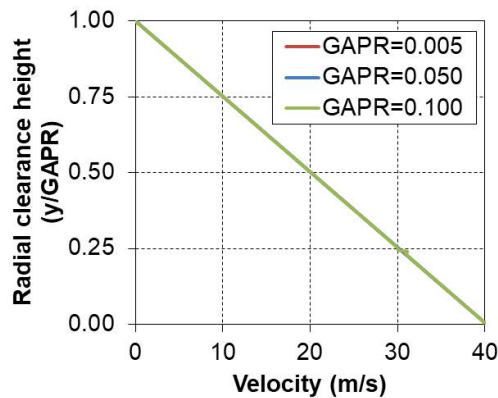
5.4.5.2 Effect of pressure ratio and radial clearance

Similar to the effect of tip speed as presented in the previous section, the effect of pressure ratio and radial clearance for a constant tip speed of 40 m/s is shown in

Figure 5.14. The effect of PR=8.5 and different radial clearances are shown in Figure 5.14 (a), while the effect of PR=12.5 is presented in Figure 5.14 (b).



(a) Pressure ratio 8.5



(b) Pressure ratio 12.5

Figure 5.14: Effect of pressure ratio and radial clearance on drag loss

For both pressure ratio values and different radial clearances, the velocity profile does not change much, and again it closely follows the Couette type.

5.5 Case Study on Gear Power Loss

A helical gear pair with a gear ratio of 2.23 and centre distance of 125 mm, helix angle with 12° , pressure angle 20° and a module of 2.5 mm is considered for the evaluation. The effect of input power upon the power loss during the idle motion and power loss during the gear mesh under load is as shown in Figure 5.15. The power loss in idle motion is mainly a function of peripheral speed, the position of the gears in oil and the direction of rotation of mating gears. Since the input power does not affect any of the parameters mentioned above, the power loss in idle motion for

different input powers remains constant.

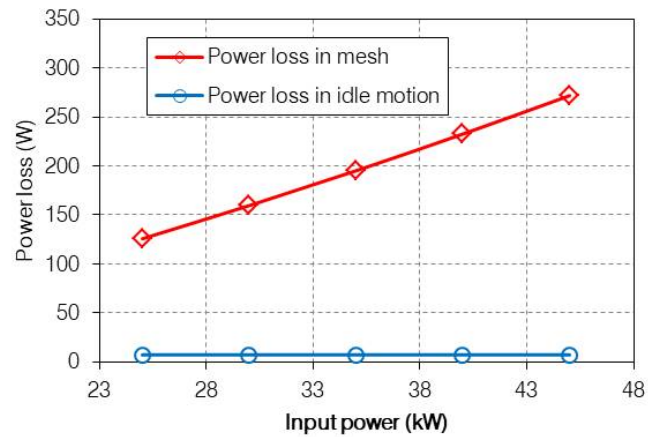


Figure 5.15: Power loss v/s input power

The power loss in the mesh is a function of the gear ratio as well and the effect of it is presented in Figure 5.16. The power loss during mesh under load increases as the gear ratio increases. The reason behind this is the increase in gear ratio, the contact ratio between mating gears increases which causes an increase in the power loss. The helical gear specification mentioned above with the power input of 24 kW is used for the calculation.

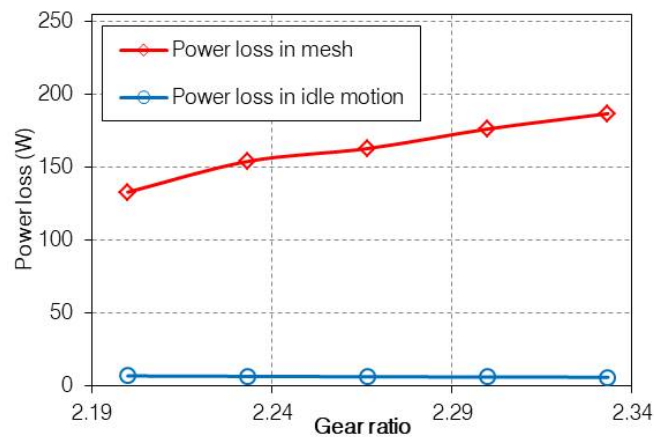


Figure 5.16: Power loss v/s gear ratio

The transmission efficiency decreases with the increase in gear ratio as presented in Figure 5.17. As the gear ratio increases, the efficiency drops because of the increased power loss for the gears in mesh under load.

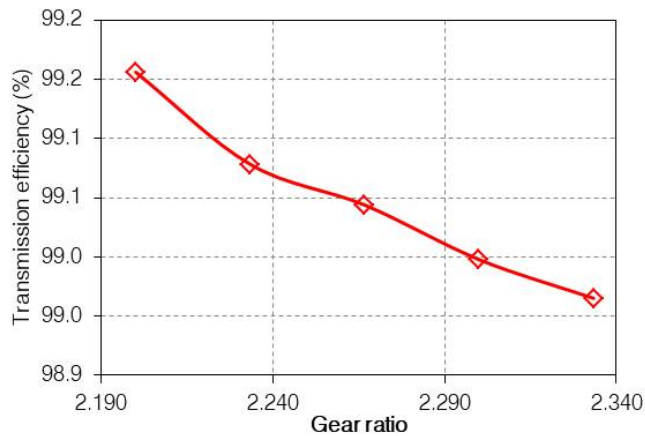


Figure 5.17: Transmission efficiency v/s gear ratio

The parametric study shows that total power loss increases with the increase in input speed, gear ratio and input power.

5.6 Contribution of each Element to Power Loss

The elements that contribute to the total power loss and the extent of their respective contributions constitute critical information during the compressor selection or design process. This data empowers engineers to make informed decisions regarding the optimization of the compressor system. Specifically, knowing the individual contributions of bearings, seals, and oil drag to the total power loss is pivotal in achieving an efficient design.

Figure 5.18 illuminates the individual contributions to power loss made by bearings, seals, and oil drag in the context of a size 2 compressor operating at a pressure ratio of 8.5. This graphical representation provides a tangible insight into the relative significance of each component's contribution, thereby aiding in making judicious decisions during the compressor design or selection phase.

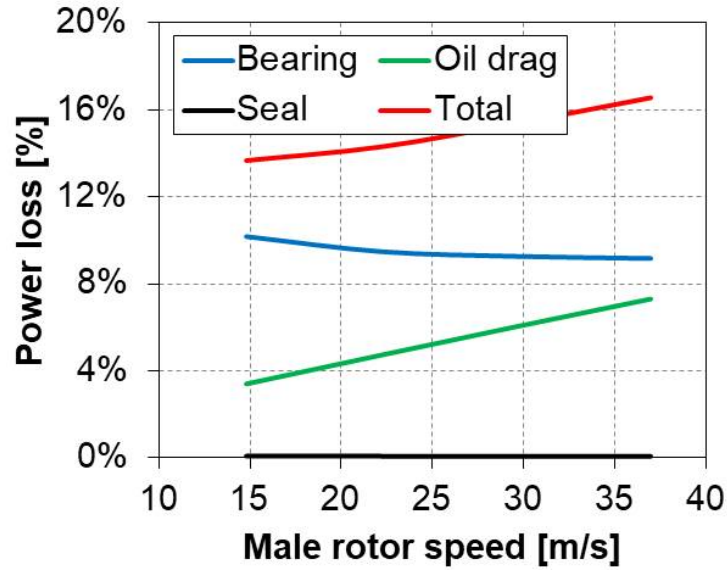


Figure 5.18: Contribution of each element of power loss

Notably, the contribution to power loss by rolling bearings emerges as the most substantial among the three considered elements. However, as operational speed increases, the contribution of drag loss undergoes a rapid escalation. While the bearing power loss contribution might appear to diminish in relative terms, it's important to highlight that the absolute value of bearing power loss experiences an increase in correspondence with speed and pressure ratio alterations. This trend is distinctly depicted in Figure 5.3, providing a comprehensive visual understanding of the interplay between these parameters and their impact on bearing power loss.

5.7 Summary

This chapter serves as a comprehensive exposition of detailed case studies and in-depth parametric analyses, all centred around the context of oil-injected, twin-screw air compressors. The focal point of these investigations is to discover the intricate interplay between various operational factors and the resulting power loss.

Spanning across a range of compressor sizes, pressure ratios, and rotational speeds, the case studies delve into a meticulous analysis of all elements contributing to power loss. These elements include bearings, shaft seals, oil drag, and gears. The comprehensive examination takes into account the varying impact of these parame-

ters on frictional power loss.

The scope of these analyses encompasses tip speeds up to 40 m/s, with pressure ratios reaching a maximum of 12.5. Additionally, the viscosity of the oil used for these evaluations is set at 68 cSt at 40°C, a parameter that further enriches the comprehensiveness and applicability of the study's findings.

- The axial load carrying angular contact ball bearings contribute more significantly to the frictional power loss than the radial load carrying cylindrical roller bearings.
- With the increase in pressure ratio and shaft speed, the bearing frictional power loss increases almost linearly.
- Bigger sizes of compressors exhibit higher bearing frictional losses than their small counterparts, while the loss due to increased pressure is more significant in bigger compressors.
- Increased shaft speed shows a linear increase in shaft seal power loss while the increased shaft diameter shows an exponential rise in shaft seal power loss.
- However, the surface roughness and oil temperature do not show a significant effect on the shaft seal power loss.
- Oil drag loss in the discharge axial clearance gap is nearly 55% of the total drag loss, and nearly 43% in the radial clearance, while drag loss occurring in the interlobe clearance is very low.
- As the pressure ratio increases, the percentage increase in the interlobe element of the drag loss is higher than in the other two elements.
- As the oil viscosity is increased, the total drag loss in larger compressors increases more rapidly than in smaller compressors.
- As the clearances are increased, the radial and axial elements of the drag loss are reduced significantly than the interlobe element of the drag loss.
- Within the specified limits of compressor size, tip speed and pressure ratio, the Couette flow always dominates Poiseuille flow, and the velocity profile in radial

clearance almost maintains the Couette dominant shape with almost no effect of radial clearance, pressure ratio and tip speed.

- The gear power loss increases with input power, speed and gear ratio.
- For a direct-drive (without gears), oil-flooded compressor, bearings are the biggest contributor to power loss, 8-10% of total shaft power, while oil drag loss dominates after a certain tip speed (~ 40 m/s) and can contribute up to 12% of total shaft power.
- The shaft seal power loss is negligible.

Chapter 6

Experimental Validation and Discussions

6.1 Introduction

This chapter presents the experimental validation of the drag loss model presented in Chapter 4 and total shaft power consumption for different sizes of the compressors operating at different operating conditions. Towards the later part of this Chapter, a regression analysis is performed to derive correlations for the estimation of mechanical power loss from the bearing, shaft seal and oil drag. These correlations can be readily used in commercial performance prediction programs.

6.2 Experimental Validation of Drag Loss Predictions

6.2.1 Drag loss model

To experimentally validate the developed analytical model for oil drag loss, the top land area on the outer diameter of the screw rotor is modified, which substantially influences the drag loss. As presented in the previous section, the drag loss in interlobe clearance does not contribute much to the power loss. Also, the axial clearance shear flow region changes could demand substantial manufacturing changes and possibly affect the other performance parameters. So changes are made only in the shear flow region of the radial clearance while designing different screw rotor profiles.

6.2.1.1 Rotor profiles designed for different levels of drag losses

A patented ‘N’ rotor profile (Stosic, 1996) is taken as a reference profile as shown in Figure 6.1 (a). Based on this profile, three screw rotor profiles are modified and designed, ‘beta-1’, ‘beta-2’ and ‘beta-3’. The characteristic of the ‘beta-1’ profile is that it provides a slanting tip on the female rotor top land. It is generated by providing a slant on the female rotor of the N-profile. The slant is provided from the leading edge of the profile to the trailing edge such that the minimum radial clearance is maintained at the leading edge of the profile, as shown in Figure 6.1 (b). With this change, it is anticipated that the shearing of the oil in the radial clearance will reduce and, ultimately, the drag loss. The ‘beta-2’ profile provides a longer top land width than the ‘N’ screw rotor profile and is expected to contribute to higher drag loss. It is shown in Figure 6.1 (c). While the ‘beta-3’ profile has a similar slant provided in ‘beta-1’ but on a ‘beta-2’ profile. The schematic representation of ‘N’, ‘beta-1’, ‘beta-2’ and ‘beta-3’ female rotor top lands is shown in Figure 6.1.

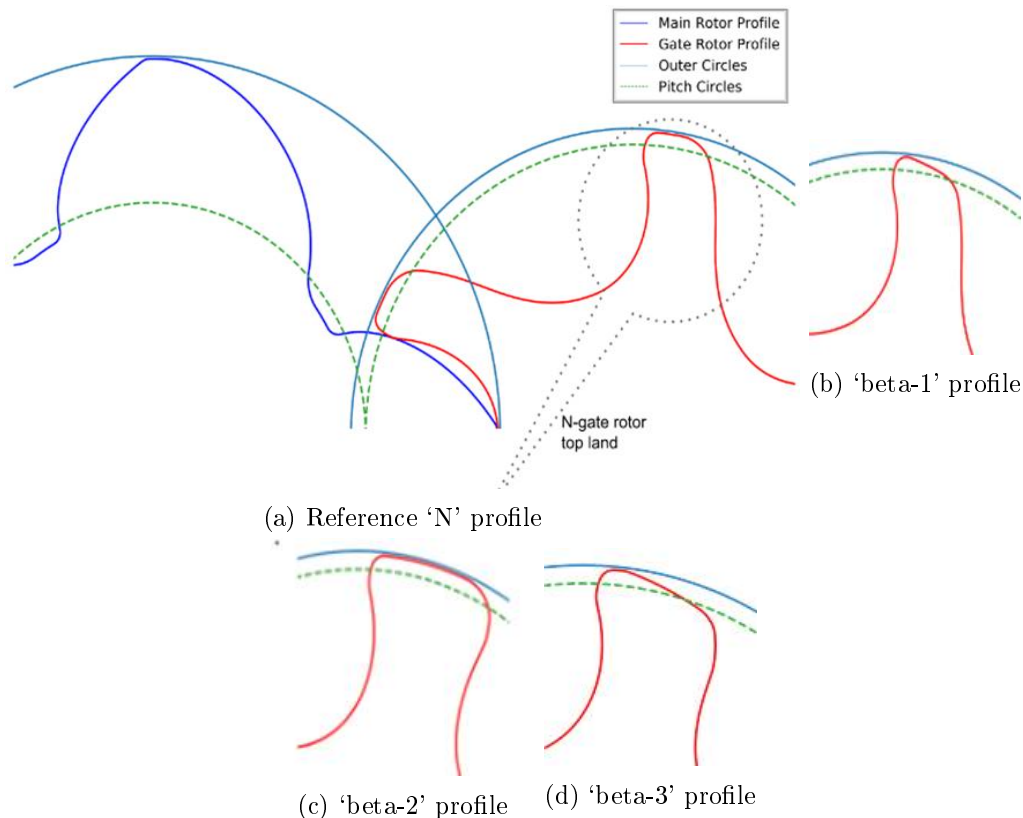


Figure 6.1: Schematic representation of slanting female rotor top land in ‘beta-1’, ‘beta-2’ and ‘beta-3’ profiles compared to the flat land on ‘N’ profile

The marked red portion on top of each female rotor depicts the area of minimum radial clearance where oil film shears, as shown in Figure 6.2.

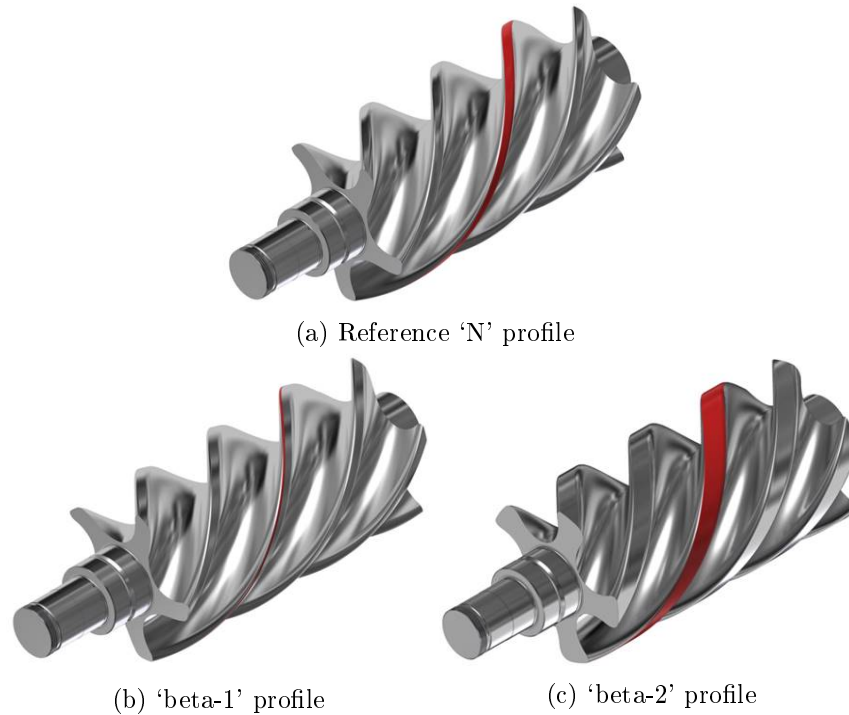


Figure 6.2: Schematic representation of 'N', 'beta-1' and 'beta-2' female rotor top lands where oil film shears in the radial gap

As indicated in the previous section, with the increase in tip speed, the contribution of the oil drag loss increases and can be more than that of the bearing power loss. So the experiments were carried out at relatively higher tip speeds to amplify the effects caused by oil drag.

6.2.1.2 Experimental measurements

An oil-flooded, twin-screw, air compressor (size 2 compressor) packaged unit with an electric motor of 55 x 1.2 kW rating along with a speed-increasing gear drive, was used for the experimentation and is shown in Figure 6.3.



Figure 6.3: A Kirloskar 55 kW oil-flooded, twin-screw, air compressor package

The profile geometric characteristics of the above-mentioned rotor profiles and clearances that were maintained during assembly are mentioned in Table 6.1.

Table 6.1: Profile geometric characteristics and assembly clearances

Parameter	N	beta-1	beta-2	beta-3
GAPI [mm]	0.040	0.040	0.040	0.040
GAPA [mm]	0.060	0.060	0.060	0.060
GAPR [mm]	0.040	0.040	0.040	0.040
Interlobe leakage area [mm ²]	24.185	24.191	27.461	27.366
Female rotor top land width [mm]	14.0	14.0	24.0	24.0

Here, GAPI stands for interlobe clearance, GAPA stands for axial clearance on the compressor's high-pressure side, and GAPR stands for radial clearance.

The rotors are manufactured on precision grinding machines with a profile accuracy of ± 7 micrometres. The photographs of manufactured rotors with the profiles that are mentioned earlier are shown in Figure 6.4.



(a) Actual 'beta-1' profile



(b) Actual 'beta-2' profile



(c) Actual 'beta-3' profile

Figure 6.4: Actual photographs of rotors with the tweaked profiles 'beta-1', 'beta-2' and 'beta-3'

These rotors were assembled in the same bare compressor housing, one after the other, and were operated at a package discharge pressure of 7 bar gauge. An electric motor drove the compressor through a gearbox with the male rotor rotating at a constant tip speed of 37.3 m/s. The female rotor side was provided with a single-point oil injection in the bare compressor housing. The oil with a density of 860 kg/m³ and viscosity of 68 cSt at 40°C was used. A representative schematic of the air and oil flow through the compressor package is shown in Figure 6.5.

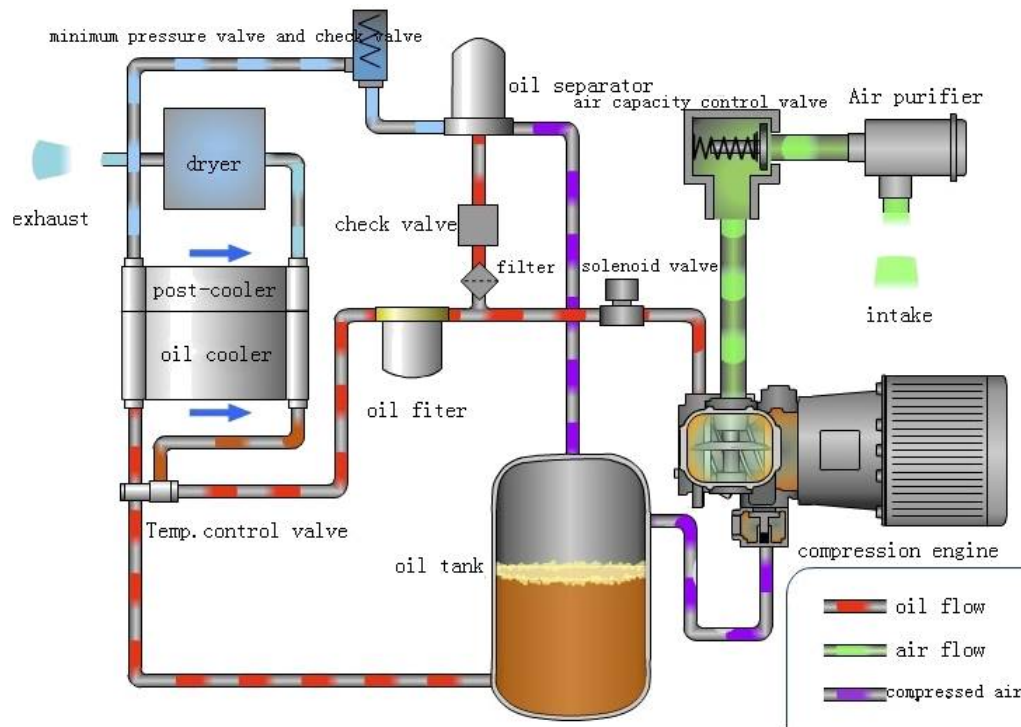


Figure 6.5: Schematic of air and oil flow through the compressor package (Prasanna, 2023)

The oil is circulated within the package through the pressure differential created by the compressor discharge pressures and pressure drop in the oil return line. This is also affected by the position at which the oil is injected into the compressor. Since the same compressor housing and the same operating pressures were maintained during the testing, the oil flow rate for all three rotor profiles can be considered constant. The air volume flow rate is measured using a differential manometer at the discharge end of the compressor package and is normalised to the suction conditions.

6.2.1.3 Summary

In the context of experimental shaft power measurement, the total recorded shaft power is composed of the adiabatic power and the aggregate mechanical power loss. This comprehensive mechanical power loss encompasses losses attributed to oil drag, bearings, shaft seals, and gears. Importantly, since the experiments utilize the same compressor with identical bearings, shaft seals, and gears, and are conducted under constant operating conditions, the power losses associated with bearings, shaft seals, and gears are deemed consistent. This reasoning is grounded in the constancy of

geometry and operating conditions, which in turn maintain consistent load factors.

For the calculation of bearing power loss predictions, the Harris model (Harris and Kotzalas, 2007) is employed, yielding a calculated power loss of 5.74 kW. Meanwhile, the shaft seal power loss is predicted utilizing methods proposed by Frölich et al. (2014) and Engelke (2011), resulting in a calculated shaft seal power loss of 0.05 kW.

Furthermore, employing the superimposed Couette-Poiseuille method outlined in the preceding section for the calculation of drag loss, the results for drag loss at distinct clearance elements for ‘N’, ‘beta-1’, ‘beta-2’, and ‘beta-3’ are presented in Table 6.2.

Table 6.2: Drag loss prediction for ‘N’, ‘beta-1’, ‘beta-2’ and ‘beta-3’

Sr.No.	Power loss [kW]	‘N’	‘beta-1’	‘beta-2’	‘beta-3’
(A)	Bearing + seal	5.79	5.79	5.79	5.79
(B.1)	Drag loss in radial clearance	1.85	0.27	3.03	0.43
(B.2)	Drag loss in high pressure axial clearance	1.40	1.40	1.40	1.40
(B.3)	Drag loss in interlobe clearance	0.03	0.3	0.07	0.07
(B)	Total drag loss	3.28	1.71	4.49	1.89

The computation of total shaft power consumption involves several components. The total power loss is summed with the adiabatic power, taking into account a reasonable assumption of 2% power loss attributed to the driving gears. The adiabatic power necessary for air compression is influenced by parameters such as the adiabatic index, suction pressure, pressure ratio, and suction volume flow rate. For this calculation, an adiabatic index of 1.4 is utilized for air. The suction pressure, measured during the experiments, is 0.95 bar, while the discharge pressure is held constant at 8.31 bar. Under these conditions, and with an operating tip speed of 37.3 m/s, the suction volume flow rate is determined to be 9.12 m³/min. Using the SCORPATH program (Stosic, 2005), the adiabatic power is predicted to be 43.25 kW.

By integrating the aforementioned elements, the total shaft power consumption is calculated, yielding a comprehensive and representative measure of the compressor's power usage. The predictions are given in Table 6.3.

Table 6.3: Flow and shaft power predictions for 'N', 'beta-1', 'beta-2' and 'beta-3'

Sr.No.	Predictions	'N'	'beta-1'	'beta-2'	'beta-3'
(A)	FAD [m ³ /min]	9.12	9.12	9.71	9.43
	% change in FAD with respect to 'N'	-	0.00%	6.53%	3.40%
(B)	Compressor shaft power [kW] (adiabatic power + power loss in bearings, seal, drag loss and gears)	53.37	51.76	57.48	53.45
	% change in shaft power with respect to 'N'	-	-1.51%	7.41%	5.27%

The results obtained for the experimental measurement of suction volume flow rate (FAD) and the compressor shaft power are presented in Table 6.4.

Table 6.4: Experimental measurements for flow and shaft power for 'N', 'beta-1', 'beta-2' and 'beta-3'

Sr.No.	Experimental measurements	'N'	'beta-1'	'beta-2'	'beta-3'
(A)	FAD [m ³ /min]	8.75	8.82	9.10	9.16
	% change in FAD with respect to 'N'	-	0.87%	4.00%	4.71%
(B)	Compressor shaft power [kW]	55.33	54.89	61.52	59.25
	% change in shaft power with respect to 'N'	-	-0.80%	11.19%	7.08%

Given that the prediction does not accurately capture the variation in measured volume flow rates from 'N' to 'beta-1', 'beta-2', and 'beta-3', a correction is in-

roduced based on experimental measurements. This correction is applied to the adiabatic power in the total shaft power prediction. The procedure involves calculating the percentage change in measured suction volume flow rates for ‘beta-1’, ‘beta-2’, and ‘beta-3’ in relation to the ‘N’ rotor profile. Subsequently, this same percentage change is employed to adjust the shaft power prediction.

The comparison between the corrected prediction and the experimental shaft power measurements is then presented in Table 6.5. This approach enhances the alignment between predictions and actual measurements by accounting for the observed variations in volume flow rates across different rotor profiles.

Table 6.5: A comparison of prediction and measured shaft power ‘N’, ‘beta-1’, ‘beta-2’ and ‘beta-3’

Sr.No.	Normalised parameters	‘N’	‘beta-1’	‘beta-2’	‘beta-3’
(A)	Corrected prediction of shaft power [kW]	52.32	51.12	58.20	54.51
	% change in shaft power prediction with respect to ‘N’	-	-2.29%	11.24%	4.18%
(B)	Compressor shaft power measured [kW]	55.33	54.89	61.52	59.25
	% change in shaft power with respect to ‘N’	-	-0.80%	11.19%	7.08%

The comparison displayed in the aforementioned table demonstrates that the percentage change predictions for ‘beta-1’, ‘beta-2’, and ‘beta-3’ exhibit a reasonable agreement with the predictions, serving as an indication of the successful validation of the analytical model.

The unexpectedly heightened power increase was accompanied by audible rattling noise during testing. This noise serves as an indicator of a deficient gate rotor torque characteristic in the profile, a concern that was initially anticipated during the design phase. Notably, the calculated gate rotor torque for the ‘beta’ profiles was determined to be much greater than that of the ‘N’ profile under the tested conditions. Another potential contributor to the higher-than-expected power lies in the uniform discharge

port design, which was tailored for the ‘N’ profile. Since the bearing housing remains constant while only the rotors are replaced, this uniform discharge port design might not optimally accommodate the characteristics of the ‘beta’ profiles. This can be attributed to the thicker gate rotor lobes in the ‘beta’ profiles, leading to a distinct theoretical discharge port profile as compared to that of the ‘N’ rotors. Consequently, this difference could contribute to the elevated power readings in comparison to the ‘N’ profile. It is important to note that this limitation arises from the absence of distinct bearing housings for different rotor profiles in the experimental setup.

Moreover, even though the experiments did not simulate the influence of oil flow rate, it is conceivable that an augmentation in oil flow rate would correspondingly amplify drag loss. The rationale behind this projection lies in the fact that as oil is introduced into the clearance gaps within the compression chamber to enhance volumetric efficiency, it concurrently intensifies the shearing action of the oil. It is important to note that the formulated drag loss model presupposes complete filling of the radial clearance gaps with oil, along with partial filling of the axial clearance gaps. As a result, the model inherently encapsulates the potential for heightened drag power loss in response to increased oil flow rates.

6.2.2 Accuracy and Uncertainty Analysis

The accuracy of the speed, pressure and, temperature sensors used during the experimental measurement is presented in Table 6.6.

Table 6.6: Accuracy of instruments

Parameter	Instrument	Specifications
Compressor Speed, [N]	Digital tachometer, NCTM-1000, Metravi	Test Range: 2 to 99,9999 rpm, Accuracy: $\pm 0.05\%$ ± 1 digit
Temperature, [t]	RTD Pt-100, SIMPLEX Tempsens Instruments (I) Pvt. Ltd.	3-wire, DIN-43760, Class A, Temperature range: -30°C to 350°C , Accuracy: $\pm 0.15^{\circ}\text{C}$ at 0°C
Pressure, [p]	Pressure transmitter, MBS3000-2211-1, Danfoss	2-wire, 4-20 mA, Pressure range: 0 to 16 bar, Accuracy: $\pm 0.5\%$ FSD

Throughout the process of experimental measurements, multiple sets of readings were meticulously recorded for identical operating conditions. Specifically, three sets of readings were recorded for ‘N’ and ‘beta-1’, while five sets of readings were taken for ‘beta-2’ and ‘beta-3’. In order to comprehensively gauge the anticipated variation in the measurements, an uncertainty analysis for each instrument reading was undertaken. This analysis draws insights from methods outlined in EDUCBA (2022).

The uncertainty can be calculated by using the following formula

$$\text{Uncertainty (u)} = \sqrt{\frac{\sum(x_i - \mu)^2}{n \times (n - 1)}} \quad (6.1)$$

Table 6.7: Uncertainty Analysis of ‘N’ and ‘beta-1’ Measurements

Parameter	‘N’			‘beta-1’				
FAD [m ³ /min]	9.29	9.29	9.23	9.32	9.32	9.33	9.26	9.24
FAD Mean [m ³ /min](μ)	9.27			9.29				
FAD Uncertainty [m ³ /min] (u)	0.02			0.02				
Shaft power [kW]	54.97	55.02	54.90	54.62	54.79	54.91	54.45	54.32
Shaft power mean [kW] (μ)	54.96			54.62				
Shaft power uncertainty [kW] (u)	0.04			0.11				

Table 6.8: Uncertainty Analysis of ‘beta-2’ and ‘beta-3’ Measurements

Parameter	‘beta-2’				‘beta-3’			
FAD [m ³ /min]	9.23	9.30	9.43	9.41	9.28	9.31	9.31	9.36
FAD Mean [m ³ /min](μ)	9.34				9.32			
FAD Uncertainty [m ³ /min] (u)	0.05				0.02			
Shaft power [kW]	61.22	61.43	61.46	61.61	58.26	58.71	58.64	58.83
Shaft power mean [kW] (μ)	61.43				58.61			
Shaft power uncertainty [kW] (u)	0.08				0.12			

The outcomes of the uncertainty analysis reveal that the uncertainty in the measurement of FAD ranges from 0.18% to 0.5%, while for the measurement of shaft power, the uncertainty ranges from 0.07% to 0.21%. The total compressor package power measurement employed an energy meter accompanied by a current transformer (225/5A) possessing a 0.2 class accuracy. The accuracy of power measurement was indicated as $\pm 0.35\%$ according to Electricalvolt (2022). It’s noteworthy that the comparison results presented for shaft power in Table 5 significantly exceed the measurement uncertainty associated with shaft power.

6.3 Experimental Validation of Total Power Predictions

The prediction of total power loss is calculated using different loss prediction models presented in Chapter 4. The Harris model is used to predict the power loss in bearings, a method based on Frölich’s and Engelke’s work for shaft seal and a combined Couette-Poiseuille flow model for drag loss. The predictions are made for size 1 (98mm), size 2 (141mm) and size 3 (231mm) compressor sizes for 8.5 and 12.5 pressure ratios operating at different speeds. These compressors were tested under laboratory conditions in City, University of London and Howden Compressors.

6.3.1 Test rig

The City, University of London air compressor test rig is shown in Figure 6.6. The test rig was built to meet CAGI and PNEUROF test standards where the testing procedures are carried out according to ISO 1217. The tested compressor is driven by a variable-speed electric motor through a belt drive with a pulley. Oil is injected into the compressor from the main oil supply manifold. The inlet duct of the compressor takes air through the air intake filter at the top of the compressor. Air is then mixed with oil inside the compressor. After compression, the mixture of hot oil and compressed air is discharged through a pipe at the bottom of the compressor.

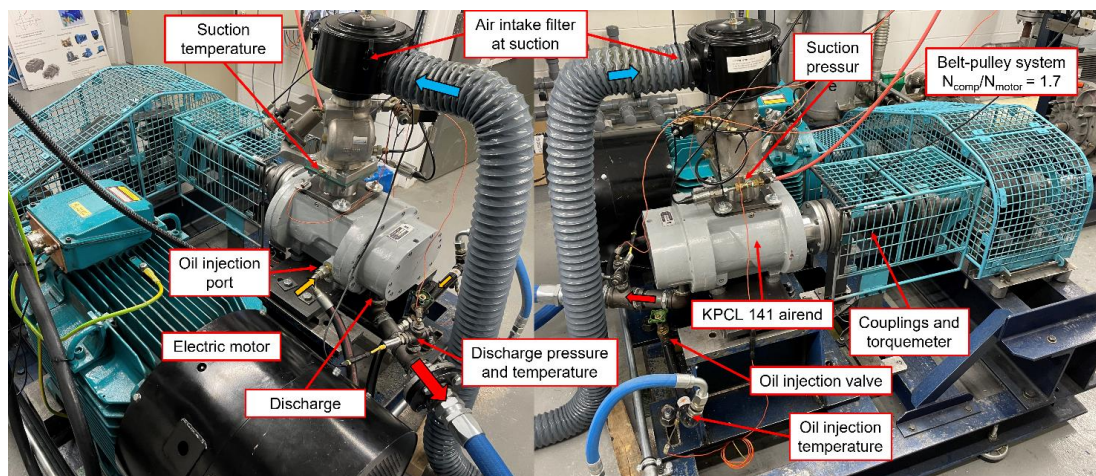


Figure 6.6: Compressor test rig – 141mm compressor

The discharged mixture of oil and air goes into a two-stage oil separator as presented in Figure 6.7. In the first stage, with the centrifugal oil separator, most of the oil is isolated from the compressed air. Oil is separated, water-cooled and re-injected into the compressor. A small amount of oil in the vapour form is then passed through the second stage separator where a filter extracts the remaining oil from air. The oil collected at the bottom of the second separator tank is not recirculated. It is occasionally removed, filtered and reused. The air leaves through a pipeline positioned at the top of the second oil separator. An orifice plate is positioned in the pipeline to measure the discharged air flow rate, and an electric ball valve is operated to regulate the discharge pressure and air flow rate. The pressure relief valve, located on top of the oil separator, is used as a safety measure for the test rig in the event of a build-up of excess pressure in the separator.

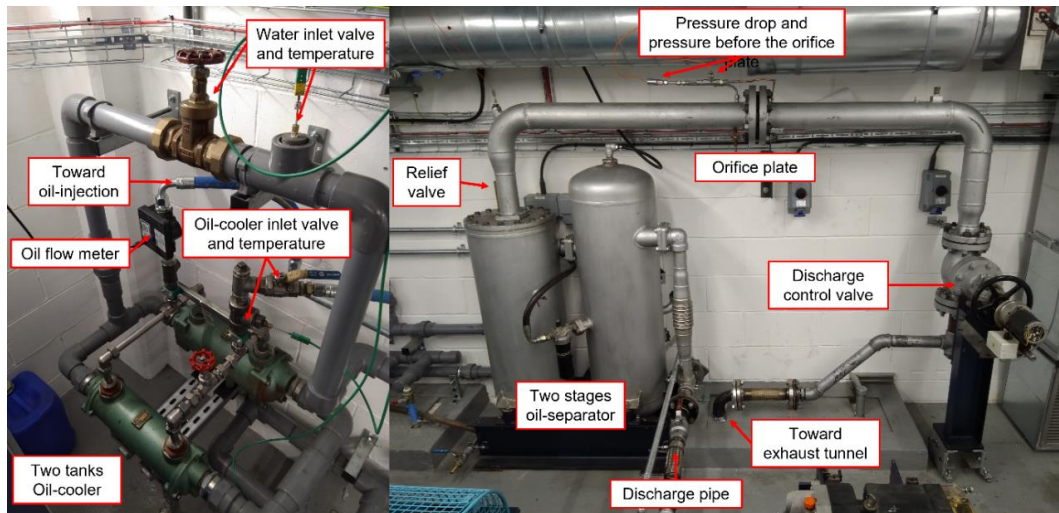


Figure 6.7: Compressor test rig - Auxiliary systems

6.3.2 Instrumentation and data acquisition

To calculate the performances of the tested compressor, several measurements are required in the form of suction and discharge pressures and temperatures, air flow rate, oil flow rate and power consumption. To ensure steady-state operating conditions, measured values are tracked in time until they stabilise. The schematic view of the test rig with all measured and calculated parameters is given in Figure 6.8. The equipment used for measurement is listed in Table 6.9.

The airflow rate is measured at the compressor discharge by use of an orifice plate according to ISO 5167-2. The orifice plate is sandwiched between two flanged pipes located between the exit of the second-stage oil separator and the discharge valve (Figure 6.7). The delivered volume flow is calculated based on the properties of air measured at the discharge (next to the orifice plate) and then normalize to inlet condition.

A data acquisition system has been used to acquire data from the transducers during the experiment. It consists of a National Instrument Compact-RIO (CRIO-9056 with an 8-slot chassis), running in FPGA (Field Programmable Gate Array) mode connected to a computer. The programming is carried out using LabVIEW from where the compressor power consumption, air flow rate, specific power and efficiencies (adiabatic and volumetric) are calculated.

The oil flow rate is calculated from the mass and energy balance of the compressor

and the oil cooler based on the measurements of temperatures of air, oil and air mixture, and oil and cooling water, as shown in the equation below. The calculated oil flow is found to be comparable with the measurements of oil flow from the oil rotameter installed on the rig.

$$m_{oil} = \frac{W_{shaft} - \dot{m}_{air} C_{p\ air} \times (T_2 - T_1)}{C_{p\ oil} \times (T_2 - T_{oil})} \quad (6.2)$$

With W_{shaft} is the main rotor shaft power; \dot{m}_{air} is the mass flow rate of air; $C_{p\ air,oil}$ the specific heat capacities of air and oil, respectively; $T_{1,2,oil}$ the suction, discharge and oil injection temperatures, respectively. Note T_{oil} is also noted T_{oe} .

Table 6.9: Measurement and instrumentation listing

Parameter	Instrument	Specifications
Compressor Speed [N]	Torquemeter Datum Electronics M425	Up to 8000 rpm
Compressor Torque [T]	Torquemeter Datum Electronics M425	Up to 250 Nm
Suction pressure [p1]	Pressure transducer, Druck UNIK5000 PTX-5022	0 to 3.5 bar(a), Accuracy= $\pm 0.2\%$ FS (± 0.007 bar)
Inlet temperature [T1]	Platinum Resistance Thermometer PT100	Range= -75°C to 350°C , Accuracy= $\pm 0.5^{\circ}\text{C}$
Discharge pressure [p2]	Pressure transducer, Druck UNIK5000 PTX-5022	Range=0-15 bar(a), Accuracy= $\pm 0.2\%$ FS (± 0.03 bar)
Discharge temperature [T2]	Platinum Resistance Thermometer PT100	Range= -75°C to 350°C , Accuracy= $\pm 0.5^{\circ}\text{C}$
Orifice plate inlet pressure [p3op]	Pressure transducer, Druck UNIK5000 PTX-5022	Range=0-15 bar(a), Accuracy= $\pm 0.2\%$ FS (± 0.03 bar)
Orifice plate inlet temperature, [T3op]	Platinum Resistance Thermometer PT100	Range= -75°C to 350°C , Accuracy= $\pm 0.5^{\circ}\text{C}$
Orifice plate differential pressure [dP]	Pressure transducer, wet/dry diff. Druck UNIK5000 PTX-5022	Range=0-50,000 Pa(g), Accuracy= $\pm 0.2\%$ FS (± 100 Pa)
Oil temperature at inlet cooler [Toi]	Range= -75°C to 350°C , Accuracy= $\pm 0.5^{\circ}\text{C}$	Range= -200°C to 1300°C , Accuracy= $\pm 2.2^{\circ}\text{C}$
Oil temperature at cooler outlet [Toe]	Platinum Resistance Thermometer PT100	Range= -75°C to 350°C , Accuracy= $\pm 0.5^{\circ}\text{C}$
Water temperature at cooler inlet and outlet [Twi, Twe]	K-type thermocouple	Range= -200°C to 1300°C , Accuracy= $\pm 2.2^{\circ}\text{C}$
Oil injection pressure	Pressure transducer, PDCR 922	Range=0-15 bar(a), Accuracy=0.6%
Oil flow rate	Gespasa MGI-110 Oval Gear Pulse Meter	Range=5-110 l/min, Accuracy= $\pm 0.5\%$

All measured and computed data are displayed on the computer screen as shown in Figure 6.8.

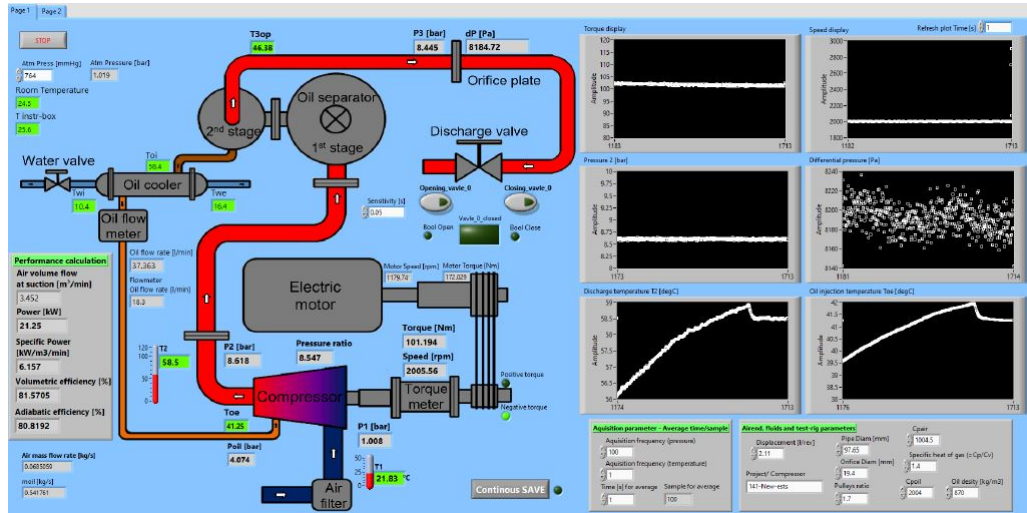


Figure 6.8: Labview front panel of experiment monitoring

6.3.3 Results

The outcomes of predictions generated by the proposed method are systematically contrasted with experimental measurements and predictions from the SCORPATH program (Stosic, 2005). These comparative analyses are visually depicted in Figure 6.9, 6.10, and 6.11. The computation of total shaft power based on the proposed method involves the summation of power losses incurred across individual components. This cumulative value is subsequently combined with the adiabatic shaft power of the compressor, aligning with the designated operating pressure ratio and speed parameters.

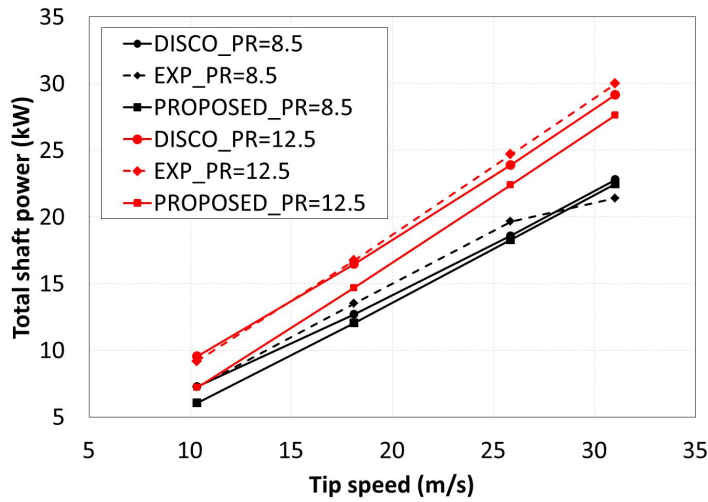


Figure 6.9: Total shaft power of 98mm compressor

A marginal decrease in the experimental measurement is observed at the highest tip speed in the context of a pressure ratio of 8.5, suggesting a potential error in the experimental data. Nevertheless, across other operational points encompassing elevated tip speeds and two distinct pressure ratios, the total shaft power predictions demonstrate a close alignment within an 8.5% margin in comparison to the experimental measurements. However, it's noteworthy that the predictions slightly under-predict the experimental measurements in these scenarios.

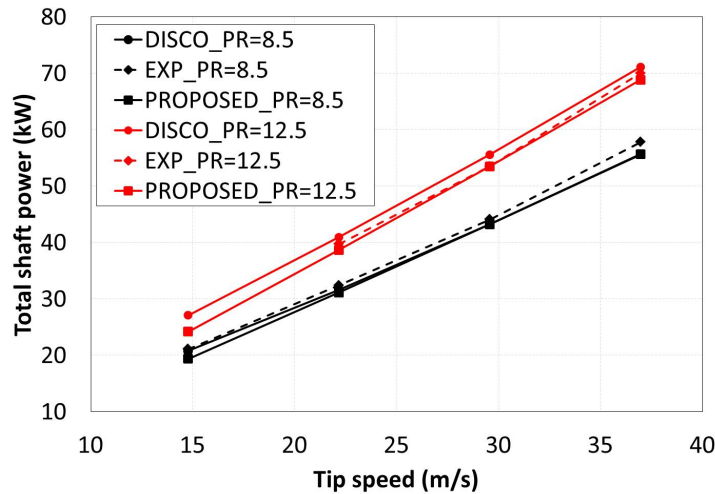


Figure 6.10: Total shaft power of 141mm compressor

Among the three different compressor sizes, the predictions of total shaft power exhibit the closest alignment with experimental measurements for the 141mm compressor. The agreement is particularly notable, being within a margin of 1.7%. However, it's worth noting that even in this case, the predictions tend to under-predict

the experimental measurements, especially at higher tip speeds and pressure ratios.

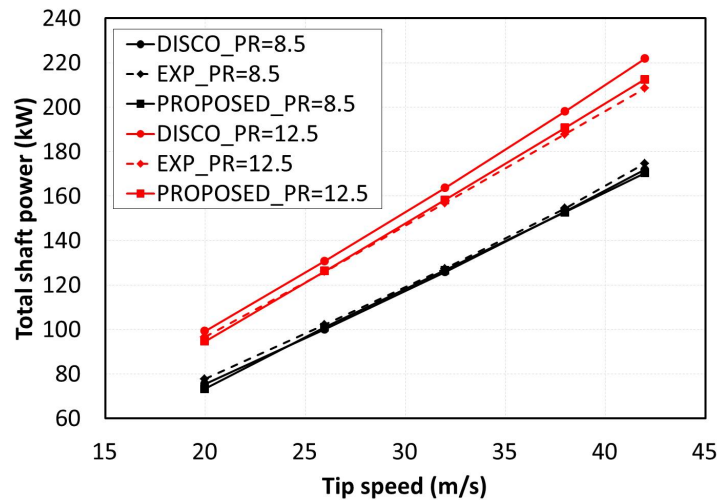


Figure 6.11: Total shaft power of 231mm compressor

The dissimilarity between the predictions of total shaft power and the corresponding experimental measurements for the 231mm compressor sizes, at pressure ratios of 8.5 and 12.5, lies within a range of 1.9% over-prediction to 2.5% under-prediction. Notably, when contrasting the predictions with empirical measurements and SCORPATH projections, a commendable level of agreement is observed across various compressor sizes, pressure ratios, and speeds.

6.4 Regression Analysis

Utilizing the predicted data points as a foundation, the attempt to establish a function representing these points is pursued in this section. The goal is to formulate a correlation capable of encapsulating the outcomes of the prediction model.

A viable method for achieving this is through Machine Learning, a methodology that entails training a model using the available dataset. However, it's important to note that this approach is applicable only on platforms equipped with libraries that facilitate model training, such as MATLAB, Python, and similar frameworks. For pre-existing screw compressor performance prediction programs that lack access to such libraries, the development of an appropriate regression model is imperative.

In this context, polynomial regression emerges as a promising technique. Three distinct correlations have been derived using polynomial regression to predict mechanical power loss attributed to bearing, shaft seal, and oil drag. The independent

variables feeding into these correlations comprise male rotor outer diameter [mm], pressure ratio, and male rotor tip speed [m/s]. This systematic approach ensures that these correlations effectively encapsulate the intricacies of the mechanical power loss phenomena across the designated parameters.

$$\begin{aligned}
 P_{loss}(x, y, z) = & a_1 + a_2x + a_3y + a_4z + a_5x^2 + a_6xy + a_7xz + a_8y^2 + a_9yz + a_{10}z^2 \\
 & + a_{11}x^3 + a_{12}x^2y + a_{13}x^2z + a_{14}y^2x + a_{15}xyz + a_{16}z^2x + a_{17}y^3 + a_{18}y^2z + a_{19}z^2y + a_{20}z^3
 \end{aligned}
 \tag{6.3}$$

where, P_{loss} is mechanical power loss [kW], x is male rotor tip speed [m/s], y is male rotor outer diameter [mm], z is pressure ratio and a 's are constants which are defined for the respective element of power loss. The constants are given in Table 6.11.

Table 6.11: Constants for power loss in bearing, shaft seal and oil drag

Constant	Bearing	Shaft seal	Oil drag
a_1	-2.63E+00	-2.36E-02	-3.45E-02
a_2	4.25E-01	5.16E-03	1.76E-04
a_3	9.93E-07	9.82E-09	2.17E-08
a_4	3.03E-03	-4.82E-14	-7.57E-08
a_5	-1.13E-03	-8.45E-05	-1.86E-03
a_6	-3.51E-03	-3.30E-05	-5.52E-05
a_7	-4.29E-02	6.77E-14	8.87E-04
a_8	1.46E-04	1.44E-06	3.18E-06
a_9	6.30E-04	4.59E-15	5.89E-07
a_{10}	3.14E-02	-1.29E-13	-1.59E-06
a_{11}	4.12E-05	9.58E-07	-1.02E-06
a_{12}	-8.85E-06	-9.85E-09	3.39E-05
a_{13}	1.31E-05	-4.97E-16	1.14E-05
a_{14}	1.18E-05	1.37E-07	2.48E-07
a_{15}	2.42E-04	-5.69E-19	-2.03E-07
a_{16}	9.61E-04	-1.87E-15	-6.69E-05
a_{17}	-6.81E-07	-6.02E-09	-1.38E-09
a_{18}	2.58E-07	-8.53E-18	-6.29E-07
a_{19}	-2.92E-05	-7.30E-17	1.01E-05
a_{20}	-1.65E-03	6.40E-15	-2.53E-05

The computation of power loss for bearing, shaft seal, and oil drag is facilitated through the utilization of Equation 6.3. Subsequently, the acquired results are meticulously compared against the predictions, with the graphical representation being interpreted in Figure 6.12, 6.13, and 6.14. In these figures, the R^2 values are

also prominently indicated, serving as a quantitative measure of the goodness of fit for the data points. This statistical metric aids in assessing the degree of alignment between the derived correlation and the actual data distribution.

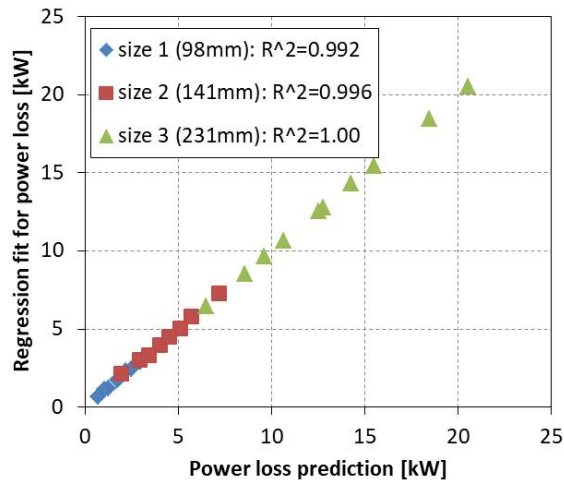


Figure 6.12: Prediction v/s Regression analysis: Bearing power loss

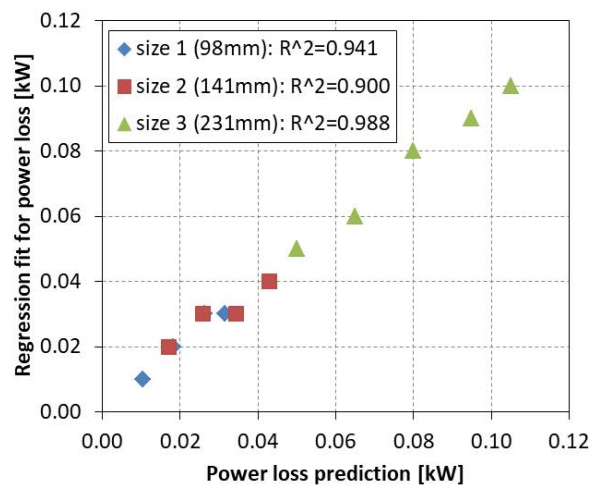


Figure 6.13: Prediction v/s Regression analysis: Shaft seal power loss

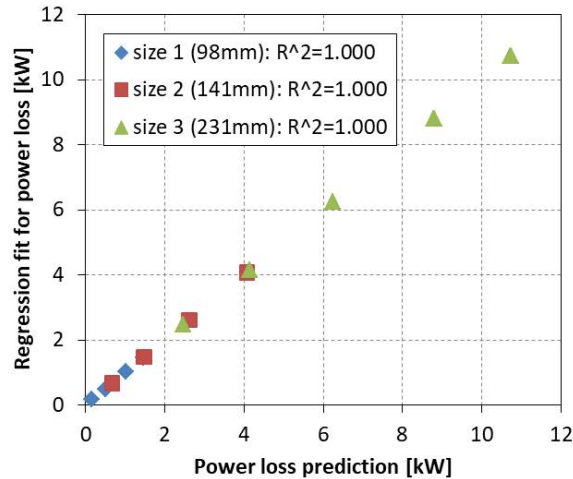


Figure 6.14: Prediction v/s Regression analysis: Oil drag loss

6.4.1 Summary of regression analysis

By employing polynomial regression analysis, a correlation has been formulated to ascertain the mechanical power loss associated with bearing, seal, and oil drag. This correlation is established as a function of key parameters, namely compressor size, tip speed, and pressure ratio. The commendable R^2 values attained for the losses incurred in bearing, seal, and drag substantiate the robust alignment between the polynomial regression model and the projected outcomes. This derived correlation, underpinned by polynomial regression, holds the potential for seamless integration into commercial performance prediction software, thereby facilitating accurate estimations of power loss in real-world scenarios.

6.5 Summary

Experimental validation has been conducted to assess the accuracy of drag loss prediction concerning distinct rotor profiles and the estimation of total shaft power under varying sizes and operational conditions. In this pursuit, three novel screw rotor profiles, namely ‘beta-1’, ‘beta-2’, and ‘beta-3’, were conceptualized and manufactured as derivative designs from the foundational ‘N’ rotor profile. These modifications were strategically aimed at inducing alternating increments and reductions in drag loss within the radial clearance of the compressor. The experimental trials were systematically undertaken to confirm the projections derived from the formulated drag loss model. The screw rotor profiles in question were integrated within the same

compressor housing, and a compressor package unit that operated under consistent working conditions.

The experimental measurements encompassed the recording of volumetric flow and shaft power. As anticipated, the shaft power pertaining to the ‘beta-1’ profile exhibited a decrement, while those corresponding to ‘beta-2’ and ‘beta-3’ profiles demonstrated increments in relation to the reference ‘N’ rotor profile. These observations aligned with the projected alterations in shaft power, and the quantitative assessment of this power variation concurred with experimental measurements for ‘beta-1’, ‘beta-2’, and ‘beta-3’ profiles. Consequently, grounded in the outcomes of the experimental validation, it can be inferred that the drag loss prediction model has been successfully validated for oil-flooded screw compressors.

Upon incorporation of power loss predictions generated by the proposed method into adiabatic power computations, a close alignment with experimental measurements and SCORPATH predictions is evident across varying compressor sizes, pressure ratios, and tip speeds. Notably, the disparities between the predictions of the proposed method and experimental measurements for total shaft power within the 141mm and 231mm compressor sizes, at pressure ratios of 8.5 and 12.5, remain within a margin of 2.5%. However, there is a slight tendency for underestimation in the case of the 98mm compressor.

The analysis indicates that a polynomial regression model offers the best fit for the projected outcomes. This correlation holds the potential for extrapolating predictions pertaining to mechanical power loss attributed to bearing, shaft seal, and oil drag across diverse compressor sizes, tip speeds, and pressure ratios.

Chapter 7

Conclusions and Recommendations for Future Work

7.1 Summary of Research

The literature is studied for available mathematical models for the prediction of the thermodynamic performance of the screw compressors. To design energy-efficient machines, the elements of the screw compressor that contribute to the power loss are identified during the literature review. It is observed that the available mathematical prediction tools approximate total mechanical power loss. This is based on the assumption that the mechanical power loss is some percentage of the adiabatic power. Also, the available tools do not quantify the contribution of the individual elements to the total power loss. The lack of this information can not lead to optimising the design of the compressor for a particular application.

A need was identified for a more accurate tool that can predict the mechanical power loss from the individual components and at the system level of the screw compressor. Once the individual-level contribution of elements to power loss is known for different operating conditions, the design can be suitably adopted to reduce the power loss and, ultimately, the compressor's power consumption. This can be achieved at the design stage and the efforts and costs involved in not only prototype development but also testing and validation of the new designs can be saved. The outcome

from the analysis would result in energy-efficient machines and savings in carbon footprint.

The methods adopted during this study resulted in

- Identification of the elements that contribute to mechanical power loss in the screw compressor. The elements that are identified are the rolling element bearings, shaft seals, drag loss caused by injected oil within oil-flooded machines and losses in the drive system like gears.
- Numerous available power loss prediction methods studied, analysed and compared for suitability in oil-flooded, twin-screw air compressor application range. Like the SKF, Harris and Palmgren methods (Harris and Kotzalas, 2007; SKF, 2018) have been reviewed for frictional loss predictions in rolling element bearings. During the prediction comparison and experimental validation (Gradu, 2000; Tu, 2016), it is seen that the Harris model predictions are in better agreement with the experimental observations within the load and speed range of application for screw compressors under analysis.
- A few of the available methods are studied that predict frictional power loss in shaft seals. The methods proposed by Engelke (2011) and Frölich et al. (2014) are referred which are based on combined empirical and semi-analytical methods for power loss prediction in seals that have been proposed during the study.
- The drag loss arising due to the injection of oil inside the compressor can be substantial. The available drag loss predictions are based on computer computational methods that require longer calculation times and can have limitations while satisfying the physical laws. The analytical tools presented in the literature are limited and do not quantify the drag loss arising in different clearance paths within the compression chamber (Deipenwisch and Kauder, 1999), (Gräßer and Brümmer, 2014), (Gräßer and Brümmer, 2014), (Gräßer and Brümmer, 2014), (Vasuthevan and Brümmer, 2018). So a simple analytical model has been developed for the drag loss prediction, which can be used to understand the effects of compression ratio, rotational speed, oil viscosity and type and magnitude of clearances present within the compressor.
- For the prediction of frictional power loss from gears, the proven method pro-

posed by Jelaska (2012) is used, and a parametric analysis is presented to understand the effect of torque transmitted, speed and gear ratio on overall power loss from the gears.

- Finally, experimental validation of the drag loss prediction model is done by designing, manufacturing and testing three different types of screw rotor profiles. It is found that the predictions from the drag loss model match very well with the experimental measurements, and the method can be used in commercial performance prediction tools for better accuracy.

7.2 Conclusions

Three oil-flooded, twin-screw compressors for air with a shaft power rating of 15 to 160 kW have been analysed. From the case studies, parametric analyses and experimental validation following conclusions can be drawn.

- The predictions from the proposed method for total shaft power which is a sum of adiabatic power and mechanical power losses, when compared with the experimental measurements for different compressor sizes at different pressure ratios and tip speeds, match very well within acceptable limits.
- For a direct-drive (without gears), oil-flooded compressor, bearings are the biggest contributor to power loss, 8-10% of total shaft power, while oil drag loss dominates after a certain tip speed (~ 40 m/s) and can contribute up to 10% of total shaft power.
- Oil drag loss in the discharge axial clearance is nearly 55% of the total drag loss, and nearly 43% in the radial clearance, while drag loss due to the interlobe clearance is very low $\sim 2\%$.
- Overall drag loss increases with a reduction in clearances and an increase in oil viscosity. The flow in clearance is dominated by Couette flow. Experimental validation of the drag loss prediction method shows good agreement with the experimental measurements.
- The axial load-carrying bearings are the biggest contributors to power loss in all bearings, while total bearing power loss increases with size, load and speed.

- The shaft seal power loss contribution is very low. FKM material make shaft seals exhibit lower power loss than nitrile material make. The power loss increases with shaft diameter and speed and does not show much change with the surface roughness and oil temperature.
- The gear power loss increases with input power, speed and gear ratio too.

The proposed method and its experimental validation show good agreement with experimental measurements; hence, this method can be used in commercial screw compressor performance prediction tools for better accuracy and enhanced capability in quantifying frictional power losses.

7.3 Future Work

Although the method proposed in this study focuses on frictional power loss arising inside the bare screw compressor, the study can be extended to electrical systems, variable frequency drive systems and different torque transmission systems like belt drive. Once complete, the prediction tool can become a comprehensive calculation tool for the complete screw compressor system, which consists of an electric motor, variable frequency drive or torque transmission drives and bare screw compressor.

- Power transmission: The mathematical modelling and experimental validation of the frictional power loss in the belt drive system can be done where such systems are used for small shaft power ratings up to 22 kW.
- Electric motors and frequency converters: A basic calculation method can be formulated for predicting mechanical power loss through the electric motors and frequency converters. From the literature studied, it is understood that a basic model for power loss from electric motors can be modelled, but for frequency converters, because of several converter topologies and different power devices, it is very challenging to propose a general mathematical model of the converter providing a high accuracy result.

Appendices

Appendix A

SKF Model

Listing A.1: SKF model

```
1 clear all
2 clc
3 format short
4 % Nomenclature
5 % M      total frictional moment
6 % Mrr    rolling frictional moment (N-mm)
7 % Msl    sliding frictional moment (N-mm)
8 % Mseal  frictional moment of seals
9 % Mdrag  frictional moment of drag losses, churning, splashing etc.
10 % phi_ish inlet shear heating reduction factor
11 % phi_rs kinematic replenishment/starvation reduction factor
12 % Grr    variable
13 % n      rotational speed (rpm)
14 % v      actual operating viscosity of the oil or base oil of the grease (mm2/s)
15 % Brg_d  bearing bore diameter (mm)
16 % Brg_D  bearing outside diameter (mm)
17 % Brg_dm bearing mean diameter (m)
18 % Brg_B  bearing width
19 % Co     basic static load rating of bearing (kN)
20 % Krs    replenishment/starvation constant
21 % Kz     bearing type related geometric constant
22 % Kl     roller bearing type related geometric constant
23 % e      base of natural logarithm
24 % Fa     axial force (N)
25 % Fr     radial force (N)
26 % R      geometric constants
27 % S      geometric constants
28 % Y      axial load factor
29 % Gsl    variable
30 % mu_sl  sliding friction coefficient
31 % phi_bl weighting factor for the sliding friction coefficient
32 % mu_bl  coefficient depending on the additive package in the lubricant
33 % mu_EHL sliding friction coefficient in full-film conditions
34 % VM     drag loss factor
35 % H      oil level
36 % irw    number of ball rows
37 % H      oil level
38
39 %*****LIMITATIONS OF THE MODEL*****
40 % Grease lubrication:  Only steady state conditions
41 %                      Lithium soap grease with mineral oil
```

```

42 %           Bearing free volume filled approximately 30%
43 %           Ambient temperature 20 degC or higher
44 % Oil lubrication:   Oil bath, oil-air or oil jet
45 %           Viscosity range from 2 to 500 mm2/s
46 % Loads equal to or larger than the recommended minimum load
47 % Constants loads in magnitude and direction
48 % Noraml operating clearance
49 % Constant speed, below the speed ratings
50 % Bearing does not exceed the limits of misalignment
51
52 n=input('Enter speed (rpm):');
53 v = input('Enter ISO VG viscosity of oil or base oil of the grease (mm2/s):');
54 % t=input('Enter operating temperature (degC):');
55 % tol=20;
56 % function nu=oil(nu_to,t)
57 % rho_to=0.8455;
58 % rho_t=rho_to-(t-40)*0.00065
59 % K=0.06;
60 % b=1344.2;
61 % c=153.75;
62 % mu_t=14.898;
63 % mu_T=K*exp(b/(T+c))
64 % nu=mu_t/rho_t
65 % end
66 % nu_t=oil(nu_to,t)
67 Fa = input('Please enter axial load on bearing (N):');
68 Fr = input('Please enter radial load on bearing (N):');
69 Co = input('Please enter bearing basic static load rating (N):');
70 Y = input('Please enter axial load factor:');
71 Oil_type=input(['Type of oil'...
72     '\n1.Mineral oil'...
73     '\n2.Synthetic oil'...
74     '\n3.Transmission fluids'...
75     '\nYour choice:']);
76 Krs = input(['Lubrication'...
77     '\n1.Low level oil bath and oil jet lubrication;'...
78     '\n2.Grease and oil-air lubrication'...
79     '\nYour choice:']);
80 if Krs==1
81     Krs=3e-8;
82 else if Krs==2
83     Krs=6e-8;
84     end
85 end
86 Brg_type=input(['Type of bearing:'...
87     '\n1.Deep groove ball bearing_single row'...
88     '\n2.Deep groove ball bearing_double row'...
89     '\n3.Angular contact ball bearing_single row'...
90     '\n4.Angular contact ball bearing_double row'...
91     '\n5.Angular contact ball bearing_four point contact'...
92     '\n6.Self-aligning ball bearings'...
93     '\n7.Cylindrical roller bearings_with a cage'...
94     '\n8.Cylindrical roller bearings_full complement'...
95     '\n9.Tapered roller bearing'...
96     '\n10.Spherical roller bearing'...
97     '\n11.Thrust ball bearing'...
98     '\n12.Cylindrical roller thrust bearing'...
99     '\n13.Spherical roller thrust bearing'...
100    '\nYour choice:']);

```

```

101 if Brg_type==1%Deep groove ball bearing_single row
102     Kz=3.1; irw=1;
103 elseif Brg_type==2%Deep groove ball bearing_double row
104     Kz=3.1; irw=2;
105 elseif Brg_type==3%Angular contact ball bearing_single row
106     Kz=4.4; irw=1;
107 elseif Brg_type==4%Angular contact ball bearing_double row
108     Kz=3.1; irw=2;
109 elseif Brg_type==5%Angular contact ball bearing_four point contact
110     Kz=3.1; irw=1;
111 elseif Brg_type==6%Self-aligning ball bearings
112     Kz=4.8; irw=1;
113 elseif Brg_type==7%Cylindrical roller bearings_with a cage
114     Kz=5.1; Kl=0.65;
115 elseif Brg_type==8%Cylindrical roller bearings_full complement
116     Kz=6.2; Kl=0.7;
117 elseif Brg_type==9%Tapered roller bearing
118     Kz=6; Kl=0.7;
119 elseif Brg_type==10%Spherical roller bearing
120     Kz=5.5; Kl=0.8;
121 elseif Brg_type==11%Thrust ball bearing
122     Kz=3.8; irw=1;
123 elseif Brg_type==12%Cylindrical roller thrust bearing
124     Kz=4.4; Kl=0.43;
125 elseif Brg_type==13%Spherical roller thrust bearing
126     Kz=5.6; Kl=0.58;
127 end
128 %Bearing geometrical dimensions
129 Brg_d = input('Please enter bearing bore diameter (mm):');
130 Brg_D = input('Please enter bearing outside diameter (mm):');
131 Brg_dm = 0.5*(Brg_d+Brg_D);
132 if Brg_type==9
133     Brg_B=input('Enter bearing width (mm): ');
134 elseif Brg_type==11
135     Brg_B=input('Enter bearing height (mm): ');
136 else Brg_B=input('Enter bearing width (mm): ');
137 end
138 H=input('Please enter height of oil bath (mm):');
139 e=2.718;
140 Brg_alphaF=24.6*(Fa/Co)^0.24;
141 if Brg_type==1 || Brg_type==2
142     temp=input(['Bearing series:'...
143         '\n1.2, 3'...
144         '\n2.42, 43'...
145         '\n3.60, 630'...
146         '\n4.62, 622'...
147         '\n5.63, 623'...
148         '\n6.64'...
149         '\n7.160, 161'...
150         '\n8.617, 618, 628, 637, 638'...
151         '\n9.619, 639'...
152         '\nYour choice:']);
153     if temp==1
154         R1=xlsread('Geometric constants.xlsx','Deep groove ball bearing','C2');
155         R2=xlsread('Geometric constants.xlsx','Deep groove ball bearing','D2');
156         S1=xlsread('Geometric constants.xlsx','Deep groove ball bearing','F2');
157         S2=xlsread('Geometric constants.xlsx','Deep groove ball bearing','G2');
158     elseif temp==2
159         R1=xlsread('Geometric constants.xlsx','Deep groove ball bearing','C3');

```

```

160     R2=xlsread('Geometric constants.xlsx','Deep groove ball bearing','D3');
161     S1=xlsread('Geometric constants.xlsx','Deep groove ball bearing','F3');
162     S2=xlsread('Geometric constants.xlsx','Deep groove ball bearing','G3');
163     elseif temp==3
164         R1=xlsread('Geometric constants.xlsx','Deep groove ball bearing','C4');
165         R2=xlsread('Geometric constants.xlsx','Deep groove ball bearing','D4');
166         S1=xlsread('Geometric constants.xlsx','Deep groove ball bearing','F4');
167         S2=xlsread('Geometric constants.xlsx','Deep groove ball bearing','G4');
168     elseif temp==4
169         R1=xlsread('Geometric constants.xlsx','Deep groove ball bearing','C5');
170         R2=xlsread('Geometric constants.xlsx','Deep groove ball bearing','D5');
171         S1=xlsread('Geometric constants.xlsx','Deep groove ball bearing','F5');
172         S2=xlsread('Geometric constants.xlsx','Deep groove ball bearing','G5');
173     elseif temp==5
174         R1=xlsread('Geometric constants.xlsx','Deep groove ball bearing','C6');
175         R2=xlsread('Geometric constants.xlsx','Deep groove ball bearing','D6');
176         S1=xlsread('Geometric constants.xlsx','Deep groove ball bearing','F6');
177         S2=xlsread('Geometric constants.xlsx','Deep groove ball bearing','G6');
178     elseif temp==6
179         R1=xlsread('Geometric constants.xlsx','Deep groove ball bearing','C7');
180         R2=xlsread('Geometric constants.xlsx','Deep groove ball bearing','D7');
181         S1=xlsread('Geometric constants.xlsx','Deep groove ball bearing','F7');
182         S2=xlsread('Geometric constants.xlsx','Deep groove ball bearing','G7');
183     elseif temp==7
184         R1=xlsread('Geometric constants.xlsx','Deep groove ball bearing','C8');
185         R2=xlsread('Geometric constants.xlsx','Deep groove ball bearing','D8');
186         S1=xlsread('Geometric constants.xlsx','Deep groove ball bearing','F8');
187         S2=xlsread('Geometric constants.xlsx','Deep groove ball bearing','G8');
188     elseif temp==8
189         R1=xlsread('Geometric constants.xlsx','Deep groove ball bearing','C9');
190         R2=xlsread('Geometric constants.xlsx','Deep groove ball bearing','D9');
191         S1=xlsread('Geometric constants.xlsx','Deep groove ball bearing','F9');
192         S2=xlsread('Geometric constants.xlsx','Deep groove ball bearing','G9');
193     elseif temp==9
194         R1=xlsread('Geometric constants.xlsx','Deep groove ball bearing','C10');
195         R2=xlsread('Geometric constants.xlsx','Deep groove ball bearing','D10');
196         S1=xlsread('Geometric constants.xlsx','Deep groove ball bearing','F10');
197         S2=xlsread('Geometric constants.xlsx','Deep groove ball bearing','G10');
198     end
199 elseif Brg_type==3
200     temp=input(['Bearing series:'.
201         '\n1.72xx BECBP'...
202         '\n2.73xx BECBP'...
203         '\n3.72xx ACCBM'...
204         '\n4.73xx ACCBM'...
205         '\nYour choice:']);
206     if temp==1
207         R1=xlsread('Geometric constants.xlsx','Angular contact ball bearing','C2');
208         R2=xlsread('Geometric constants.xlsx','Angular contact ball bearing','D2');
209         R3=xlsread('Geometric constants.xlsx','Angular contact ball bearing','E2');
210         S1=xlsread('Geometric constants.xlsx','Angular contact ball bearing','G2');
211         S2=xlsread('Geometric constants.xlsx','Angular contact ball bearing','H2');
212         S3=xlsread('Geometric constants.xlsx','Angular contact ball bearing','I2');
213     elseif temp==2
214         R1=xlsread('Geometric constants.xlsx','Angular contact ball bearing','C3');
215         R2=xlsread('Geometric constants.xlsx','Angular contact ball bearing','D3');
216         R3=xlsread('Geometric constants.xlsx','Angular contact ball bearing','E3');
217         S1=xlsread('Geometric constants.xlsx','Angular contact ball bearing','G3');
218         S2=xlsread('Geometric constants.xlsx','Angular contact ball bearing','H3');

```

```

219     S3=xlsread('Geometric constants.xlsx','Angular contact ball bearing','I3');
220 elseif temp==3
221     R1=xlsread('Geometric constants.xlsx','Angular contact ball bearing','C4');
222     R2=xlsread('Geometric constants.xlsx','Angular contact ball bearing','D4');
223     R3=xlsread('Geometric constants.xlsx','Angular contact ball bearing','E4');
224     S1=xlsread('Geometric constants.xlsx','Angular contact ball bearing','G4');
225     S2=xlsread('Geometric constants.xlsx','Angular contact ball bearing','H4');
226     S3=xlsread('Geometric constants.xlsx','Angular contact ball bearing','I4');
227 elseif temp==4
228     R1=xlsread('Geometric constants.xlsx','Angular contact ball bearing','C5');
229     R2=xlsread('Geometric constants.xlsx','Angular contact ball bearing','D5');
230     R3=xlsread('Geometric constants.xlsx','Angular contact ball bearing','E5');
231     S1=xlsread('Geometric constants.xlsx','Angular contact ball bearing','G5');
232     S2=xlsread('Geometric constants.xlsx','Angular contact ball bearing','H5');
233     S3=xlsread('Geometric constants.xlsx','Angular contact ball bearing','I5');
234 end
235 elseif Brg_type==4
236     temp=input(['Bearing series:'. ...
237         '\n1.32xxA'...
238         '\n2.33xxA'...
239         '\nYour choice:']);
240     if temp==1
241         R1=xlsread('Geometric constants.xlsx','Angular contact ball bearing','C6');
242         R2=xlsread('Geometric constants.xlsx','Angular contact ball bearing','D6');
243         R3=xlsread('Geometric constants.xlsx','Angular contact ball bearing','E6');
244         S1=xlsread('Geometric constants.xlsx','Angular contact ball bearing','G6');
245         S2=xlsread('Geometric constants.xlsx','Angular contact ball bearing','H6');
246         S3=xlsread('Geometric constants.xlsx','Angular contact ball bearing','I6');
247     elseif temp==2
248         R1=xlsread('Geometric constants.xlsx','Angular contact ball bearing','C7');
249         R2=xlsread('Geometric constants.xlsx','Angular contact ball bearing','D7');
250         R3=xlsread('Geometric constants.xlsx','Angular contact ball bearing','E7');
251         S1=xlsread('Geometric constants.xlsx','Angular contact ball bearing','G7');
252         S2=xlsread('Geometric constants.xlsx','Angular contact ball bearing','H7');
253         S3=xlsread('Geometric constants.xlsx','Angular contact ball bearing','I7');
254     end
255 elseif Brg_type==5
256     R1=xlsread('Geometric constants.xlsx','Angular contact ball bearing','C8');
257     R2=xlsread('Geometric constants.xlsx','Angular contact ball bearing','D8');
258     R3=xlsread('Geometric constants.xlsx','Angular contact ball bearing','E8');
259     S1=xlsread('Geometric constants.xlsx','Angular contact ball bearing','G8');
260     S2=xlsread('Geometric constants.xlsx','Angular contact ball bearing','H8');
261     S3=xlsread('Geometric constants.xlsx','Angular contact ball bearing','I8');
262 elseif Brg_type==6
263     temp=input(['Bearing series:'. ...
264         '\n1.12'...
265         '\n2.13'...
266         '\n3.22'...
267         '\n4.23'...
268         '\n5.112'...
269         '\n6.130'...
270         '\n7.139'...
271         '\nYour choice:']);
272     if temp==1
273         R1=xlsread('Geometric constants.xlsx','Self-aligning ball bearing','C2');
274         R2=xlsread('Geometric constants.xlsx','Self-aligning ball bearing','D2');
275         R3=xlsread('Geometric constants.xlsx','Self-aligning ball bearing','E2');
276         S1=xlsread('Geometric constants.xlsx','Self-aligning ball bearing','G2');
277         S2=xlsread('Geometric constants.xlsx','Self-aligning ball bearing','H2');

```

```

278     S3=xlsread('Geometric constants.xlsx','Self-aligning ball bearing','I2');
279 elseif temp==2
280     R1=xlsread('Geometric constants.xlsx','Self-aligning ball bearing','C3');
281     R2=xlsread('Geometric constants.xlsx','Self-aligning ball bearing','D3');
282     R3=xlsread('Geometric constants.xlsx','Self-aligning ball bearing','E3');
283     S1=xlsread('Geometric constants.xlsx','Self-aligning ball bearing','G3');
284     S2=xlsread('Geometric constants.xlsx','Self-aligning ball bearing','H3');
285     S3=xlsread('Geometric constants.xlsx','Self-aligning ball bearing','I3');
286 elseif temp==3
287     R1=xlsread('Geometric constants.xlsx','Self-aligning ball bearing','C4');
288     R2=xlsread('Geometric constants.xlsx','Self-aligning ball bearing','D4');
289     R3=xlsread('Geometric constants.xlsx','Self-aligning ball bearing','E4');
290     S1=xlsread('Geometric constants.xlsx','Self-aligning ball bearing','G4');
291     S2=xlsread('Geometric constants.xlsx','Self-aligning ball bearing','H4');
292     S3=xlsread('Geometric constants.xlsx','Self-aligning ball bearing','I4');
293 elseif temp==4
294     R1=xlsread('Geometric constants.xlsx','Self-aligning ball bearing','C5');
295     R2=xlsread('Geometric constants.xlsx','Self-aligning ball bearing','D5');
296     R3=xlsread('Geometric constants.xlsx','Self-aligning ball bearing','E5');
297     S1=xlsread('Geometric constants.xlsx','Self-aligning ball bearing','G5');
298     S2=xlsread('Geometric constants.xlsx','Self-aligning ball bearing','H5');
299     S3=xlsread('Geometric constants.xlsx','Self-aligning ball bearing','I5');
300 elseif temp==5
301     R1=xlsread('Geometric constants.xlsx','Self-aligning ball bearing','C6');
302     R2=xlsread('Geometric constants.xlsx','Self-aligning ball bearing','D6');
303     R3=xlsread('Geometric constants.xlsx','Self-aligning ball bearing','E6');
304     S1=xlsread('Geometric constants.xlsx','Self-aligning ball bearing','G6');
305     S2=xlsread('Geometric constants.xlsx','Self-aligning ball bearing','H6');
306     S3=xlsread('Geometric constants.xlsx','Self-aligning ball bearing','I6');
307 elseif temp==6
308     R1=xlsread('Geometric constants.xlsx','Self-aligning ball bearing','C7');
309     R2=xlsread('Geometric constants.xlsx','Self-aligning ball bearing','D7');
310     R3=xlsread('Geometric constants.xlsx','Self-aligning ball bearing','E7');
311     S1=xlsread('Geometric constants.xlsx','Self-aligning ball bearing','G7');
312     S2=xlsread('Geometric constants.xlsx','Self-aligning ball bearing','H7');
313     S3=xlsread('Geometric constants.xlsx','Self-aligning ball bearing','I7');
314 elseif temp==7
315     R1=xlsread('Geometric constants.xlsx','Self-aligning ball bearing','C8');
316     R2=xlsread('Geometric constants.xlsx','Self-aligning ball bearing','D8');
317     R3=xlsread('Geometric constants.xlsx','Self-aligning ball bearing','E8');
318     S1=xlsread('Geometric constants.xlsx','Self-aligning ball bearing','G8');
319     S2=xlsread('Geometric constants.xlsx','Self-aligning ball bearing','H8');
320     S3=xlsread('Geometric constants.xlsx','Self-aligning ball bearing','I8');
321 end
322 elseif Brg_type==7
323     temp=input(['Bearing series:'.
324         '\nBearing with cage of the N, NU, NJ or NUP design'...
325         '\n1.2, 3'...
326         '\n2.4'...
327         '\n3.10'...
328         '\n4.12, 20'...
329         '\n5.22'...
330         '\n6.23'...
331         '\nHigh capacity bearings with cage of the NCF..ECJB, RN.ECJB, NJF..ECJA, RNU..ECJA or
           NUH..ECMH design'...
332         '\n7.22'...
333         '\n8.23'...
334         '\nYour choice:']);
335 if temp==1

```

```

336     R1=xlsread('Geometric constants.xlsx','Cylindrical roller bearing','C2');
337     S1=xlsread('Geometric constants.xlsx','Cylindrical roller bearing','E2');
338     S2=xlsread('Geometric constants.xlsx','Cylindrical roller bearing','F2');
339 elseif temp==2
340     R1=xlsread('Geometric constants.xlsx','Cylindrical roller bearing','C3');
341     S1=xlsread('Geometric constants.xlsx','Cylindrical roller bearing','E3');
342     S2=xlsread('Geometric constants.xlsx','Cylindrical roller bearing','F3');
343 elseif temp==3
344     R1=xlsread('Geometric constants.xlsx','Cylindrical roller bearing','C4');
345     S1=xlsread('Geometric constants.xlsx','Cylindrical roller bearing','E4');
346     S2=xlsread('Geometric constants.xlsx','Cylindrical roller bearing','F4');
347 elseif temp==4
348     R1=xlsread('Geometric constants.xlsx','Cylindrical roller bearing','C5');
349     S1=xlsread('Geometric constants.xlsx','Cylindrical roller bearing','E5');
350     S2=xlsread('Geometric constants.xlsx','Cylindrical roller bearing','F5');
351 elseif temp==5
352     R1=xlsread('Geometric constants.xlsx','Cylindrical roller bearing','C6');
353     S1=xlsread('Geometric constants.xlsx','Cylindrical roller bearing','E6');
354     S2=xlsread('Geometric constants.xlsx','Cylindrical roller bearing','F6');
355 elseif temp==6
356     R1=xlsread('Geometric constants.xlsx','Cylindrical roller bearing','C7');
357     S1=xlsread('Geometric constants.xlsx','Cylindrical roller bearing','E7');
358     S2=xlsread('Geometric constants.xlsx','Cylindrical roller bearing','F7');
359 elseif temp==7
360     R1=xlsread('Geometric constants.xlsx','Cylindrical roller bearing','C8');
361     S1=xlsread('Geometric constants.xlsx','Cylindrical roller bearing','E8');
362     S2=xlsread('Geometric constants.xlsx','Cylindrical roller bearing','F8');
363 elseif temp==8
364     R1=xlsread('Geometric constants.xlsx','Cylindrical roller bearing','C9');
365     S1=xlsread('Geometric constants.xlsx','Cylindrical roller bearing','E9');
366     S2=xlsread('Geometric constants.xlsx','Cylindrical roller bearing','F9');
367 end
368 elseif Brg_type==8
369     R1=xlsread('Geometric constants.xlsx','Cylindrical roller bearing','C10');
370     S1=xlsread('Geometric constants.xlsx','Cylindrical roller bearing','E10');
371     S2=xlsread('Geometric constants.xlsx','Cylindrical roller bearing','F10');
372 elseif Brg_type==9
373     temp=input(['Bearing series:'];
374               '\n1.302'...
375               '\n2.303'...
376               '\n3.313(X)'...
377               '\n4.320(X)'...
378               '\n5.322'...
379               '\n6.322B'...
380               '\n7.323'...
381               '\n8.323B'...
382               '\n9.329'...
383               '\n10.330'...
384               '\n11.331'...
385               '\n12.332'...
386               '\n13.LL'...
387               '\n14.L'...
388               '\n15.LM'...
389               '\n16.M'...
390               '\n17.HM'...
391               '\n18.H'...
392               '\n19.HH'...
393               '\n20.ALL OTHER'...
394               '\nYour choice:']);

```



```

454     S2=xlsread('Geometric constants.xlsx','Tapered roller bearing','G13');
455 elseif temp==13
456     R1=xlsread('Geometric constants.xlsx','Tapered roller bearing','C14');
457     R2=xlsread('Geometric constants.xlsx','Tapered roller bearing','D14');
458     S1=xlsread('Geometric constants.xlsx','Tapered roller bearing','F14');
459     S2=xlsread('Geometric constants.xlsx','Tapered roller bearing','G14');
460 elseif temp==14
461     R1=xlsread('Geometric constants.xlsx','Tapered roller bearing','C15');
462     R2=xlsread('Geometric constants.xlsx','Tapered roller bearing','D15');
463     S1=xlsread('Geometric constants.xlsx','Tapered roller bearing','F15');
464     S2=xlsread('Geometric constants.xlsx','Tapered roller bearing','G15');
465 elseif temp==15
466     R1=xlsread('Geometric constants.xlsx','Tapered roller bearing','C16');
467     R2=xlsread('Geometric constants.xlsx','Tapered roller bearing','D16');
468     S1=xlsread('Geometric constants.xlsx','Tapered roller bearing','F16');
469     S2=xlsread('Geometric constants.xlsx','Tapered roller bearing','G16');
470 elseif temp==16
471     R1=xlsread('Geometric constants.xlsx','Tapered roller bearing','C17');
472     R2=xlsread('Geometric constants.xlsx','Tapered roller bearing','D17');
473     S1=xlsread('Geometric constants.xlsx','Tapered roller bearing','F17');
474     S2=xlsread('Geometric constants.xlsx','Tapered roller bearing','G17');
475 elseif temp==17
476     R1=xlsread('Geometric constants.xlsx','Tapered roller bearing','C18');
477     R2=xlsread('Geometric constants.xlsx','Tapered roller bearing','D18');
478     S1=xlsread('Geometric constants.xlsx','Tapered roller bearing','F18');
479     S2=xlsread('Geometric constants.xlsx','Tapered roller bearing','G18');
480 elseif temp==18
481     R1=xlsread('Geometric constants.xlsx','Tapered roller bearing','C19');
482     R2=xlsread('Geometric constants.xlsx','Tapered roller bearing','D19');
483     S1=xlsread('Geometric constants.xlsx','Tapered roller bearing','F19');
484     S2=xlsread('Geometric constants.xlsx','Tapered roller bearing','G19');
485 elseif temp==19
486     R1=xlsread('Geometric constants.xlsx','Tapered roller bearing','C20');
487     R2=xlsread('Geometric constants.xlsx','Tapered roller bearing','D20');
488     S1=xlsread('Geometric constants.xlsx','Tapered roller bearing','F20');
489     S2=xlsread('Geometric constants.xlsx','Tapered roller bearing','G20');
490 elseif temp==20
491     R1=xlsread('Geometric constants.xlsx','Tapered roller bearing','C21');
492     R2=xlsread('Geometric constants.xlsx','Tapered roller bearing','D21');
493     S1=xlsread('Geometric constants.xlsx','Tapered roller bearing','F21');
494     S2=xlsread('Geometric constants.xlsx','Tapered roller bearing','G21');
495 end
496 elseif Brg_type==10
497     temp=input(['Bearing series:']...
498         '\n1.213 E, 222 E'...
499         '\n2.222'...
500         '\n3.223'...
501         '\n4.223 E'...
502         '\n5.230'...
503         '\n6.231'...
504         '\n7.232'...
505         '\n8.238'...
506         '\n9.239'...
507         '\n10.240'...
508         '\n11.241'...
509         '\n12.248'...
510         '\n13.249'...
511         '\nYour choice:');
512 if temp==1

```



```

631     R1=1.03e-6; S1=1.6e-2;
632 elseif Brg_type==12
633     R1=2.25e-6; S1=0.154;
634 elseif Brg_type==13
635     temp=input([' Bearing series:'...
636               '\n1.292'...
637               '\n2.292 E'...
638               '\n3.293'...
639               '\n4.293 E'...
640               '\n5.294 E'...
641               '\nYour choice:']);
642     if temp==1
643         R1=xlsread('Geometric constants.xlsx','Spherical roller thrust bearing','C2');
644         R2=xlsread('Geometric constants.xlsx','Spherical roller thrust bearing','D2');
645         R3=xlsread('Geometric constants.xlsx','Spherical roller thrust bearing','E2');
646         R4=xlsread('Geometric constants.xlsx','Spherical roller thrust bearing','F2');
647         S1=xlsread('Geometric constants.xlsx','Spherical roller thrust bearing','G2');
648         S2=xlsread('Geometric constants.xlsx','Spherical roller thrust bearing','H2');
649         S3=xlsread('Geometric constants.xlsx','Spherical roller thrust bearing','I2');
650         S4=xlsread('Geometric constants.xlsx','Spherical roller thrust bearing','J2');
651         S5=xlsread('Geometric constants.xlsx','Spherical roller thrust bearing','K2');
652     elseif temp==2
653         R1=xlsread('Geometric constants.xlsx','Spherical roller thrust bearing','C3');
654         R2=xlsread('Geometric constants.xlsx','Spherical roller thrust bearing','D3');
655         R3=xlsread('Geometric constants.xlsx','Spherical roller thrust bearing','E3');
656         R4=xlsread('Geometric constants.xlsx','Spherical roller thrust bearing','F3');
657         S1=xlsread('Geometric constants.xlsx','Spherical roller thrust bearing','G3');
658         S2=xlsread('Geometric constants.xlsx','Spherical roller thrust bearing','H3');
659         S3=xlsread('Geometric constants.xlsx','Spherical roller thrust bearing','I3');
660         S4=xlsread('Geometric constants.xlsx','Spherical roller thrust bearing','J3');
661         S5=xlsread('Geometric constants.xlsx','Spherical roller thrust bearing','K3');
662     elseif temp==3
663         R1=xlsread('Geometric constants.xlsx','Spherical roller thrust bearing','C4');
664         R2=xlsread('Geometric constants.xlsx','Spherical roller thrust bearing','D4');
665         R3=xlsread('Geometric constants.xlsx','Spherical roller thrust bearing','E4');
666         R4=xlsread('Geometric constants.xlsx','Spherical roller thrust bearing','F4');
667         S1=xlsread('Geometric constants.xlsx','Spherical roller thrust bearing','G4');
668         S2=xlsread('Geometric constants.xlsx','Spherical roller thrust bearing','H4');
669         S3=xlsread('Geometric constants.xlsx','Spherical roller thrust bearing','I4');
670         S4=xlsread('Geometric constants.xlsx','Spherical roller thrust bearing','J4');
671         S5=xlsread('Geometric constants.xlsx','Spherical roller thrust bearing','K4');
672     elseif temp==4
673         R1=xlsread('Geometric constants.xlsx','Spherical roller thrust bearing','C5');
674         R2=xlsread('Geometric constants.xlsx','Spherical roller thrust bearing','D5');
675         R3=xlsread('Geometric constants.xlsx','Spherical roller thrust bearing','E5');
676         R4=xlsread('Geometric constants.xlsx','Spherical roller thrust bearing','F5');
677         S1=xlsread('Geometric constants.xlsx','Spherical roller thrust bearing','G5');
678         S2=xlsread('Geometric constants.xlsx','Spherical roller thrust bearing','H5');
679         S3=xlsread('Geometric constants.xlsx','Spherical roller thrust bearing','I5');
680         S4=xlsread('Geometric constants.xlsx','Spherical roller thrust bearing','J5');
681         S5=xlsread('Geometric constants.xlsx','Spherical roller thrust bearing','K5');
682     elseif temp==5
683         R1=xlsread('Geometric constants.xlsx','Spherical roller thrust bearing','C6');
684         R2=xlsread('Geometric constants.xlsx','Spherical roller thrust bearing','D6');
685         R3=xlsread('Geometric constants.xlsx','Spherical roller thrust bearing','E6');
686         R4=xlsread('Geometric constants.xlsx','Spherical roller thrust bearing','F6');
687         S1=xlsread('Geometric constants.xlsx','Spherical roller thrust bearing','G6');
688         S2=xlsread('Geometric constants.xlsx','Spherical roller thrust bearing','H6');
689         S3=xlsread('Geometric constants.xlsx','Spherical roller thrust bearing','I6');

```

```

690     S4=xlsread('Geometric constants.xlsx','Spherical roller thrust bearing','J6');
691     S5=xlsread('Geometric constants.xlsx','Spherical roller thrust bearing','K6');
692     end
693 end
694 for i=1:1:31
695     n(i)=n(i)+500;
696 % Calculation for Mrr starts here
697 phi_ish(i)=1/(1+1.84e-9*(n(i)*Brg_dm)^1.28*v^0.64);
698 phi_rs(i)=1/e^(Krs*v*n(i)*(Brg_d+Brg_D)*sqrt(Kz/(2*(Brg_D-Brg_d))));
699
700 if Brg_type==1 && Fa==0 || Brg_type==2 && Fa==0
701     Grr=R1*Brg_dm^1.96*Fr^0.54; Gsl(i)=S1*Brg_dm^-0.26*Fr^(5/3);
702 elseif Brg_type==1 && Fa>0 || Brg_type==2 && Fa>0
703     Grr=R1*Brg_dm^1.96*(Fr+(R2*Fa/sind(Brg_aplhaF)))^0.54; Gsl(i)=S1*Brg_dm^-0.145*(Fr^5+(S2*
704     Brg_dm^1.5*Fa^4/sind(Brg_aplhaF)))^(1/3);
705 elseif Brg_type==3 || Brg_type==4 || Brg_type==5
706     FgR(i)=R3*Brg_dm^4*n(i)^2; FgS(i)=S3*Brg_dm^4*n(i)^2;
707     Grr=R1*Brg_dm^1.97*(Fr+FgR(i)+R2*Fa)^0.54; Gsl(i)=S1*Brg_dm^0.26*((Fr+FgS(i))^(4/3)+S2*Fa
708     ^4/3);
709 elseif Brg_type==6
710     FgR(i)=R3*Brg_dm^3.5*n(i)^2; FgS(i)=S3*Brg_dm^3.5*n(i)^2;
711     Grr=R1*Brg_dm^2*(Fr+FgR(i)+R2*Fa)^0.54; Gsl(i)=S1*Brg_dm^-0.12*((Fr+FgS(i))^(4/3)+S2*Fa^(4/3)
712     );
713 elseif Brg_type==7 || Brg_type==8
714     Grr=R1*Brg_dm^2.41*Fr^0.31; Gsl(i)=S1*Brg_dm^0.9*Fa+S2*Brg_dm*Fr;
715 elseif Brg_type==9
716     Grr=R1*Brg_dm^2.38*(Fr+R2*Y*Fa)^0.31; Gsl(i)=S1*Brg_dm^0.82*(Fr+S2*Y*Fa);
717 elseif Brg_type==10
718     Grr_e=R1*Brg_dm^1.85*(Fr+R2*Fa)^0.54; Gsl_e=S1*Brg_dm^0.25*(Fr^4+S2*Fa^4)^(1/3);
719     Grr_l=R3*Brg_dm^2.3*(Fr+R4*Fa)^0.31; Gsl_l=S3*Brg_dm^0.94*(Fr^3+S4*Fa^3)^(1/3);
720     Grr=min(Grr_e,Grr_l); Gsl(i)=min(Gsl_e,Gsl_l);
721 elseif Brg_type==11
722     Grr=R1*Brg_dm^1.83*Fa^0.54; Gsl(i)=S1*Brg_dm^0.05*Fa^(4/3);
723 elseif Brg_type==12
724     Grr=R1*Brg_dm^2.38*Fa^0.31; Gsl(i)=S1*Brg_dm^0.62*Fa;
725 elseif Brg_type==13
726     Grr_e=R1*Brg_dm^1.96*(Fr+R2*Fa)^0.54; Gsl_e=S1*Brg_dm^-0.35*(Fr^(5/3)+S2*Fa^(5/3));
727     Grr_l=R3*Brg_dm^2.39*(Fr+R4*Fa)^0.31; Gsl_l=S3*Brg_dm^0.89*(Fr+Fa);
728     Grr=min(Grr_e,Grr_l); Gsr=min(Gsl_e,Gsl_l); Gf=S4*Brg_dm^0.76*(Fr+S5*Fa); Gsl(i)=Gsr+Gf/(e^1e
729     -6*(n(i)*v)^1.4*Brg_dm);
730 end
731 Mrr(i)=phi_ish(i)*phi_rs(i)*Grr*(v*n(i))^0.6;
732 % Calculation for Mrr ends here
733
734 % Calculation for Msl starts here
735 phi_bl(i)=1/(e^(2.6e-8*(n(i)*v)^1.4*Brg_dm));
736 if Brg_type==7 || Brg_type==8
737     mu_EHL=0.02;
738 elseif Brg_type==9
739     mu_EHL=0.002;
740 elseif Oil_type==1
741     mu_EHL=0.05;
742 elseif Oil_type==2
743     mu_EHL=0.04;
744 elseif Oil_type==3
745     mu_EHL=0.1;
746 end
747 mu_bl=0.15;
748 mu_sl=phi_bl(i)*mu_bl+(1-phi_bl(i))*mu_EHL;

```

```

745 Msl(i)=Gsl(i)*mu_sl;
746 % Calculation for Msl ends here
747
748 % Calculation for Mdrag starts here
749 fA=0.05*Kz*(Brg_d+Brg_D)/(Brg_D-Brg_d);
750 if H>1.2*Brg_dm
751     H=1.2*Brg_dm;
752 end
753 t=(2*acos((0.6*Brg_dm-H)/(0.6*Brg_dm)));
754 Rs=0.36*Brg_dm^2*((t)-sind(radtodeg(t)))*fA;
755 if t>=0 && t<=pi()
756     ft=sind(0.5*radtodeg(t));
757 elseif t>pi() && t<(2*pi())
758     ft=1;
759 end
760 if Brg_type==1 || Brg_type==2 || Brg_type==3 || Brg_type==4 || Brg_type==5 || Brg_type==6 ||
    Brg_type==11%ball bearings
761     VM=(-1.318*(H/Brg_dm)^6+1.597*(H/Brg_dm)^5+4.122*(H/Brg_dm)^4-7.761*(H/Brg_dm)^3+3.515*(H/
        Brg_dm)^2+0.811*(H/Brg_dm)-0.021)/1000;
762 %     VM=0.00004;
763     Kball=irw*Kz*(Brg_d+Brg_D)*1e-12/(Brg_D-Brg_d);
764     Mdrag(i)=0.4*VM*Kball*Brg_dm^5*n(i)^2+1.093e-7*n(i)^2*Brg_dm^3*(n(i)*Brg_dm^2*ft/v)^-1.379*Rs
        ;
765 else%roller bearings
766     VM=(1.518*(H/Brg_dm)^6-8.464*(H/Brg_dm)^5+16.22*(H/Brg_dm)^4-13.16*(H/Brg_dm)^3+3.887*(H/
        Brg_dm)^2+1.203*(H/Brg_dm)-0.009)/1000;
767 %     VM=0.00003;
768     lD=5*Kl*Brg_B/Brg_dm;
769     Cw=2.789e-10*lD^3-2.786e-4*lD^2+0.0195*lD+0.6439;
770     Kroll=Kl*Kz*(Brg_d+Brg_D)*1e-12/(Brg_D-Brg_d);
771     Mdrag(i)=4*VM*Kroll*Cw*Brg_B*Brg_dm^4*n(i)^2+1.093e-7*n(i)^2*Brg_dm^3*(n(i)*Brg_dm^2*ft/v)
        ^-1.379*Rs;
772 end
773 % Calculation for Mdrag ends here
774
775 % Calculation for M and power loss starts here
776 % M(i)=Mrr(i)+Msl(i)+Mdrag(i);
777 Mind(i)=Mdrag(i)*1e-3;%Unit Nm
778 Mdep(i)=(Mrr(i)+Msl(i))*1e-3;%Unit Nm
779 M(i)=Mdep(i)+Mind(i);%Unit Nm
780 Ploss(i)=1.05e-4*M(i)*1e3*n(i);%Unit W
781 % Calculation for M and power loss ends here
782 %plot(n(1:i),M(1:i),'-k*');
783 %plot(n(1:i),Ploss(1:i),'-go');
784 % plot(n(1:i),Mind(1:i),'-b+',n(1:i),Mdep(1:i),'m',n(1:i),M(1:i),'-go');
785 % plot(n(1:i),Mind(1:i),'m',n(1:i),Mdep(1:i),'-go',n(1:i),M(i),'-b+');
786 % plot(n(1:i),Mrr(1:i),'-r*',n(1:i),Msl(1:i),'-b+',n(1:i),Mdrag(1:i),'-go');
787 % legend('Rolling friction','Sliding friction','Drag friction');
788 % title('Female-Axial-Discharge');
789 %hold on;
790 %xlabel('Speed (rpm)'); ylabel('Frictional moment (Nm)');
791 %grid on
792 n(i+1)=n(i);
793 %hold off;
794 end

```

Appendix B

Palmgren Model

Listing B.1: Palmgren model

```
1 clear all
2 clc
3 Lubrication_type=input(['Type of lubrication:'...
4     '\n1.Grease'...
5     '\n2.Oil'...
6     '\nYour choice:']);
7 p=input ('Enter pressure (kg/mm2):');%0.01033;
8 v=input('Enter ISO VG viscosity of oil or base oil of the grease@40degC (cSt or mm2/s):');%68;
9 Fa=input('Please enter axial load on bearing (N):');
10 Fr=input('Please enter radial load on bearing (N):');
11 X=input('Enter radial load factor:');
12 Y=input('Enter axial load factor:');
13 Cs=input('Please enter bearing basic static load rating (N):');
14 d=input('Please enter bearing bore diameter (mm):');
15 D=input('Please enter bearing outside diameter (mm):');
16 dm=0.5*(d+D);
17 alpha=input('Enter bearing contact angle, alpha (degrees):');
18 rho=input('Enter oil density (g/ml):');
19 eta=v*rho;%dynamic viscosity in mPa.s
20 %Average values of factors from Palmgren model
21 fo=2.5;
22 f1=0.000275;
23 n=2400-50;
24 %Load independent friction torque
25 for i=1:1:70
26     n(i)=n(i)+50;
27     w(i)=2*pi()*n(i)/60;
28     if Lubrication_type==2 %Oil lubrication
29         if (eta*w(i)/p)<2e-6
30             M_0(i)=1.5572e-6*fo*p*dm^3
31         elseif (eta*w(i)/p)>=2e-6
32             M_0(i)=9.81e-10*fo*p*dm^3*((eta*w(i))/p)^(2/3);
33         end
34     elseif Lubrication_type==1 && v*n(i)>=2000 %Grease lubrication
35         M_0(i)=fo*9.81e-11*(v*n(i))^(2/3)*dm^3;
36     end
37     n(i+1)=n(i);
38     %Load dependent friction torque
39     g1P0=max(0.8*Fa*cot(deg2rad(alpha)),Fr);
40     M_l=0.00098*f1*g1P0*dm;
41     %Total friction torque
```

```

42     M_total(i)=M_0(i)+M_L;
43     %Total frictional power loss
44     n;
45     Ploss(i)=((2*pi()/60)*M_total(i)*n(i));
46     %Plotting values
47     % figure(1);
48     % plot(n(1:i),M_total(1:i),'r:');
49     % hold on;
50     % xlabel('Speed (rpm)')
51     % ylabel('Frictional moment (N-m)')
52     % title('Total Frictional Moment against Speed')
53     % grid on
54     n(i+1)=n(i);
55     % hold off;
56     % figure(2)
57     % plot(n(1:i),Ploss(1:i),'b-');
58     % hold on;
59     % xlabel('Speed (rpm)')
60     % ylabel('Frictional Power Loss (W)')
61     % title('Total Frictional Power loss against speed')
62     % grid on
63     % n(i+1)=n(i);
64     % hold off;
65     end
66     M_0(1);
67     M_L;
68     Ploss(1)

```

Appendix C

Harris Model

Listing C.1: Harris model

```
1 clear all
2 clc
3 format short
4 % Nomenclature
5 % B bearing width, mm
6 % Cs Bearing static load rating, N
7 % dm Bearing pitch/mean diameter, mm
8 % d Bearing bore diameter, mm
9 % D Bearing outside diameter, mm
10 % Fs Bearing static equivalent load, N
11 % fo Factor depending on the type of bearing and the method of lubrication
12 % fl Factor depending on the bearing design and relative bearing load
13 % Fbeta Factor depending on the magnitude and direction of applied load
14 % H Frictional power loss, W
15 % M Bearing friction torque, N-mm
16 % Mf Bearing friction torque due to roller end-flange load, N-mm
17 % ML Bearing friction torque due to load, N-mm
18 % Mv Bearing friction torque due to lubrication, N-mm
19 % n Rotational speed, rpm
20 % aplha Contact angle, rad,degree
21 % vo Lubricant kinematic viscosity, centistokes
22 % w Rotational speed, rad/s
23 Bearing_type=input(['Select Bearing_type of bearing:']...
24 '\n1.Ball bearing'...
25 '\n2.Roller bearing'...
26 '\nYour choice:']);
27 n=input('Enter bearing speed (rpm):');
28 n=n-1000;
29 d=input('Enter bearing bore diameter (mm):');
30 D=input('Enter bearing outside diameter (mm):');
31 dm=0.5*(d+D);
32 Cs=input('Enter bearing static load rating (N):');
33 Fr=input('Enter radial load on bearing (N):');
34 Fa=input('Enter axial load on bearing (N):');
35 if Bearing_type==2
36 X=1;Y=0;alpha=0;
37 else X=0.35;Y=0.57;1.07;alpha=40;
38 end
39 X=input('Enter radial load factor:');
40 Y=input('Enter axial load factor:');
41 alpha=input('Enter bearing contact angle, alpha (degrees):');
```

```

42 Fs=X*Fr+Y*Fa;
43 vo=input('Enter lubricant kinematic viscosity (cSt):');
44 Lubrication_type=4;
45 Lubrication_type=input(['Type of lubrication:'...
46     '\n1.Grease'...
47     '\n2.Oil mist'...
48     '\n3.Oil bath'...
49     '\n4.Oil bath (vertical shaft) or Oil jet'...
50     '\nYour choice:']);
51 if Bearing_type==1
52     Ball_type=input(['Ball bearing type:'...
53         '\n1.Radial deep-grove'...
54         '\n2.Angular-contact'...
55         '\n3.Thrust'...
56         '\n4.Double-row, self aligning'...
57         '\nYour choice:']);
58     if Ball_type==1 %Radial deep-grove
59         z=(0.0004+0.0006)/2; y=0.55;
60         Fbeta=3*Fa-0.1*Fr;
61         if Lubrication_type==1 %Grease
62             fo=(0.7+2)/2;
63         elseif Lubrication_type==2 %Oil mist
64             fo=1;
65         elseif Lubrication_type==3 %Oil bath
66             fo=2;
67         elseif Lubrication_type==4 %Oil bath (vertical shaft) or Oil jet
68             fo=4;
69         end
70     elseif Ball_type==2 %Angular-contact
71         z=0.001; y=0.33;
72         Fbeta1=0.9*Fa*atand(alpha)-0.1*Fr; Fbeta2=Fr;
73         Fbeta=max(Fbeta1,Fbeta2);
74         if Lubrication_type==1 %Grease
75             fo=2;
76         elseif Lubrication_type==2 %Oil mist
77             fo=1.7;
78         elseif Lubrication_type==3 %Oil bath
79             fo=3.3;
80         elseif Lubrication_type==4 %Oil bath (vertical shaft) or Oil jet
81             fo=6.6;
82         end
83     elseif Ball_type==3 %Thrust
84         z=0.0008; y=0.33;
85         Fbeta=Fa;
86         if Lubrication_type==1 %Grease
87             fo=5.5;
88         elseif Lubrication_type==2 %Oil mist
89             fo=0.8;
90         elseif Lubrication_type==3 %Oil bath
91             fo=1.5;
92         elseif Lubrication_type==4 %Oil bath (vertical shaft) or Oil jet
93             fo=3;
94         end
95     elseif Ball_type==4 %Double-row, self aligning
96         z=0.0003; y=0.4;
97         Fbeta1=0.9*Fa*atand(alpha)-0.1*Fr; Fbeta2=Fr;
98         Fbeta=max(Fbeta1,Fbeta2);
99         if Lubrication_type==1 %Grease
100             fo=(1.5+2)/2;

```

```

101         elseif Lubrication_type==2 %Oil mist
102             fo=(0.7+1)/2;
103         elseif Lubrication_type==3 %oil bath
104             fo=(1.5+2)/2;
105         elseif Lubrication_type==4 %Oil bath (vertical shaft) or Oil jet
106             fo=(3+4)/2;
107         end
108     end
109     elseif Bearing_type==2
110     Roller_type=input(['Roller bearing type:'...
111         '\n1.Cylindrical roller with cage'...
112         '\n2.Cylindrical roller with full complement'...
113         '\n3.Thrust cylindrical roller'...
114         '\nYour choice:']);
115     if Roller_type==1 %Cylindrical roller with cage
116         f1=0.0003;
117         Fbeta1=0.8*Fa*atand(alpha); Fbeta2=Fr;
118         Fbeta=max(Fbeta1,Fbeta2);
119         if Lubrication_type==1 %Grease
120             fo=(0.6+1)/2;
121             ff=(0.003+0.009)/2;
122         elseif Lubrication_type==2 %Oil mist
123             fo=(1.5+2.8)/2;
124             ff=(0.002+0.006)/2;
125         elseif Lubrication_type==3 %Oil bath
126             fo=(2.2+4)/2;
127             ff=(0.002+0.006)/2;
128         elseif Lubrication_type==4 %Oil bath (vertical shaft) or Oil jet
129             fo=(2.2+4)/2;
130             ff=(0.002+0.006)/2;
131         end
132     elseif Roller_type==2 %Cylindrical roller with full complement
133         f1=0.00055;
134         Fbeta1=0.8*Fa*atand(alpha); Fbeta2=Fr;
135         Fbeta=max(Fbeta1,Fbeta2);
136         if Lubrication_type==1 %Grease
137             fo=(5+10)/2;
138             ff=(0.006+0.015)/2;
139         elseif Lubrication_type==2 %Oil mist
140             fo=0;
141             ff=(0.003+0.009)/2;
142         elseif Lubrication_type==3 %Oil bath
143             fo=(5+10)/2;
144             ff=(0.003+0.009)/2;
145         elseif Lubrication_type==4 %Oil bath (vertical shaft) or Oil jet
146             fo=0;
147             ff=(0.003+0.009)/2;
148         end
149     elseif Roller_type==3 %Thrust cylindrical roller
150         f1=0.0015;ff=0;
151         Fbeta=Fa;
152         if Lubrication_type==1 %Grease
153             fo=9;
154         elseif Lubrication_type==2 %Oil mist
155             fo=0;
156         elseif Lubrication_type==3 %Oil bath
157             fo=3.5;
158         elseif Lubrication_type==4 %Oil bath (vertical shaft) or Oil jet
159             fo=8;

```

```

160         end
161     end
162 end
163 for i=1:1:9
164     n(i)=n(i)+1000;
165     if Bearing_type==1
166         f1=z*(Fs/Cs)^y;
167         % Torque applied due to load
168         ML=(f1*Fbeta*dm)*1e-3;%Unit Nm
169         % Torque due to lubricant viscous friction
170         if (vo*n(i))>=2000)
171             Mv(i)=(10^-7*fo*(vo*n(i))^(2/3)*dm^3)*1e-3;%Unit Nm
172         else
173             Mv(i)=(160e-7*fo*dm^3)*1e-3;%Unit Nm
174         end
175         %Total friction moment
176         M(i)=ML+Mv(i);%Unit Nm
177     elseif Bearing_type==2
178         % Torque applied due to load
179         ML=(f1*Fbeta*dm)*1e-3;%Unit Nm
180         % Torque due to lubricant viscous friction
181         if (vo*n(i))>=2000)
182             Mv(i)=(10^-7*fo*(vo*n(i))^(2/3)*dm^3)*1e-3;%Unit Nm
183         else
184             Mv(i)=(160e-7*fo*dm^3)*1e-3;%Unit Nm
185         end
186         %Torque due to roller end-ring flange sliding friction
187         Mf=(ff*Fa*dm)*1e-3;%Unit Nm
188         %Total friction moment
189         M(i)=(ML+Mv(i)+Mf);%Unit Nm
190     end
191     %Bearing power loss
192     H(i)=1.047e-4*M(i)*n(i)*1e3;%Unit W
193     n(i+1)=n(i);
194 end
195 FrictionalMoment_Nm=M(1);
196 BearingPowerLoss_Watts=H(1)

```

Appendix D

Shaft Seal Power Loss

Listing D.1: Shaft seal power loss model

```
1 clear all
2 clc
3 format short
4 % Nomenclature
5 % mu friction coefficient
6 % Fr radial force on seal lip N
7 % r radius of seal inner/shaft m
8 % eta oil dynamic viscosity Ns/m2
9 % t operating temperature of seal lip K
10 % b width of contact surface on shaft m
11 % Rp sum of all shaft surface roughness m
12 % n shaft speed rpm
13 % Mr frictional torque Nm
14 % P power loss W
15 % FPA frictional power loss per unit surface area W/mm2
16 %*****Frictional power loss calculation
17 error=1;
18 count=1;
19 mu=0.35;
20 d=input('Enter shaft diameter (m):');
21 %d=0.045;%25mm for 98; 45mm for 141; 60mm for 231
22 %MR, 45 & 30; FR 55 & 30
23 Fr=145.9*pi()*d;%assuming average 145.9 N/m of
24 r=d/2;
25 b=0.00022;
26 %Rp=input('Enter shaft surface roughness (m):');
27 Rp=0.8e-6;
28 n=input('Enter shaft speed (rpm):');
29 %t(count)=input('Enter oil sump temperature (K):');
30 t(count)=338;
31 A=0.0000389689;
32 B=1083.913;
33 C=166.2304;
34 eta(count)=A*exp(B/(t(count)-C));
35 %n=500;
36 Mr(count)=mu*Fr*r+eta(count)*t(count)*(b*Rp)*r^3*(2*pi())^2*n/60;
37 P(count)=2*pi()*n*Mr(count)/60;
38 FPA(count)=P(count)/(pi()*2*r*b*1e6);
39 % Vogel model constants (Ref.: Mathematical modeling of changing of dynamic
40 % viscosity as a function of temperature and pressure of mineral oils for
41 % hudyaulic systems by Darko Knezevic and Vladimir Savic
```

```

42 %      HM32      HM46      HM68      HVL46
43 % A    0.0000736317  0.0000633361  0.0000389689  0.000116198
44 % B    797.7122    879.7742    1083.913    799.7249
45 % C    177.3562    177.7865    166.2304    176.7128
46
47 % for i=1:1:20
48     while error>1e-5
49         count=count+1;
50         t(count)=t(count-1)+FPA(count-1)*16.5;
51         eta(count)=A*exp(B/(t(count)-C));
52         Mr(count)=mu*Fr*r+eta(count-1)*(b/Rp)*r^3*(2*pi())^2*n/60;
53         P(count)=2*pi()*n*Mr(count)/60;
54         FPA(count)=P(count)/(pi()*2*r*b*1e6);
55         error=abs(Mr(count)-Mr(count-1));
56     end
57     %Mr(count)
58     P(count)

```

Appendix E

Drag Loss

Listing E.1: Drag Loss Program

```
1 clear all
2 clc
3 format short
4
5 % Nomenclature
6 % z1: number of male rotor lobes
7 % z2: number of female rotor lobes
8 % p1: compressor suction pressure [bar a]
9 % p2: compressor discharge pressure [bar a]
10 % n1: rotational speed of male rotor [rpm]
11 % vair: suction volume flow rate of air [m3/min]
12 % rho_air: air density at suction [kg/m3]
13 % mair: mass flow rate of air [kg/s]
14 % mass_ratio: mass flow rate of oil divided by mass flow rate of air
15 % moil: mass flow rate of oil [kg/s]
16 % rho_oil: oil density [kg/m3]
17 % nu: oil kinematic viscosity [cSt]
18 % mu: oil dynamic viscosity [Pa.s]
19 % GAPA: axial clearance [m]
20 % GAPI: interlobe clearance [m]
21 % GAPR(1): radial clearance at rotor leading edge [m]
22 % GAPR(10): radial clearance at rotor trailing edge [m]
23 % B1: top land width of rotor tip, male rotor [m]
24 % B2: top land width of rotor tip, female rotor [m]
25 % InterlobeLeakageArea: Interlobe leakage area [m2]
26 % helix: helix angle at pitch [deg]
27 % Di1: outer diameter, male rotor [m]
28 % Dr1: root diameter, male rotor [m]
29 % Di2: outer diameter, female rotor [m]
30 % Dr2: root diameter, female rotor [m]
31 % Do1: housing bore diameter, male [m]
32 % Do2: housing bore diameter, female [m]
33 % cd: centre distance between the rotors [m]
34 % L_D1 L/D ratio, male rotor
35 % phil: wrap angle, male rotor [deg]
36 % philc: compression end angle [deg]
37 % phi_inj: oil injection angle [deg]
38 % RotorGasArea1: gas area between male rotor lobes [m2]
39 % RotorGasArea2: gas area between female rotor lobes [m2]
40 % InterlobeSLlength: interlobe sealing line length [m]
41
```

```

42 % L1 profile length of the rotor, male rotor [m]
43 % L2 profile length of the rotor, female rotor [m]
44
45 % pcd1 pitch circle diameter, male rotor [m]
46 % pcd2 pitch circle diameter, female rotor [m]
47 % shaft_dia1 shaft diameter at discharge side of male rotor [m]
48 % shaft_dia2 shaft diameter at discharge side of female rotor [m]
49
50
51
52
53 %inputs
54 z1=input('number of lobes on male rotor');
55 z2=input('number of lobes on female rotor');
56 p1=input('suction pressure, bar abs');
57 p2=input('discharge pressure, bar abs');
58 n1=input('male rotor speed, rpm');
59 n2=n1*(z1/z2);
60 vair=input('volume flow rate of air at suction, m3/min');
61 rho_air=p1*1e5/(287*(30+273));
62 mair=rho_air*vair;
63 mass_ratio=6;
64 moil=mair*mass_ratio;
65 rho_oil=input('lubricant density, kg/m3');
66 nu=input('lubricant kinematic viscosity, cSt');
67 mu=nu*1e-6*rho_oil;
68
69 %Geometrical inputs
70 GAPA=input('axial clearance gap, m');%GAPA=32e-6;
71 GAPI=input('interlobe clearance gap, m');%GAPI=32e-6;
72 GAPR(1)=input('minimum radial clearance at rotor top land, m');
73 %GAPR(1)_N=40e-6;%GAPR(1)_Beta1=40e-6;%GAPR(1)_Beta2=40e-6;%GAPR(1)_Beta3=40e-6;
74 GAPR(10)=input('maximum radial clearance at rotor top land, m');
75 %GAPR(10)_N=40e-6;%GAPR(10)_Beta1=2500e-6;%GAPR(10)_Beta2=40e-6;%GAPR(10)_Beta3=3000e-6;
76 B1=input('top land width of male rotor, m');%B1=1e-3;
77 B2=input('top land width of female rotor, m');
78 %B2_98=9e-3;%B2_141=14e-3;%B2_231=19e-3;
79 %B2_N=14e-3;%B2_Beta1=14e-3;%B2_Beta2=24e-3;%B2_Beta3=24e-3;
80 InterLobeLeakageArea=input('interlobe leakage area, m2');
81 %InterLobeLeakageArea_98=16.554030e-6;InterLobeLeakageArea_141_N=24.18514e-6;
82 % InterLobeLeakageArea_231=48.051850e-6;InterLobeLeakageArea_141_Beta1=24.19074e-6;
83 %InterLobeLeakageArea_141_Beta2=27.46058e-6;%InterLobeLeakageArea_141_Beta3=27.3658e-6;
84 helix=input('helix angle at pitch, deg');
85 %helix_98=46.346;helix_141=46.835;helix_231=46.295;
86 Di1=input('male rotor outer diameter, m');
87 %Di1_size1=0.098809;Di1_size2=0.1412;Di1_size3=0.231014;
88 Dr1=input('male rotor root diameter, m');
89 %Dr1_size1=0.057211;Dr1_size2=0.08216;Dr1_size3=0.134214;
90 Di2=input('female rotor outer diameter, m');
91 %Di2_size1=0.077746;Di2_size2=0.114;Di2_size3=0.180734;
92 Dr2=input('female rotor root diameter, m');
93 %Dr2_size1=0.036148;Dr2_size2=0.05496;Dr2_size3=0.083934;
94 cd=input('centre distance between rotors, m');
95 %cd_size1=0.0675;%cd_size2=0.0981;%cd_size3=0.1575;
96 L_D1=input('L/D ratio of male rotor');
97 phi1=input('screw rotor wrap angle, deg');%307
98 phi1c=input('screw rotor angle of compression end, deg');%phi1c_98=266;%phi1c_141=264;%phi1c_231
    =260;
99 phi_inj(1)=input('oil injection angle, deg');%68

```

```

100 RotorGasArea1=input('gas area between male rotor lobes, m2');
101 %RotorGasArea1_98=646e-6;RotorGasArea1_141=1305e-6;RotorGasArea1_231=3485e-6;
102 RotorGasArea2=input('gas area between female rotor lobes, m2');
103 %RotorGasArea2_98=536e-6;RotorGasArea2_141=1095e-6;RotorGasArea2_231=2923e-6;
104 InterlobeSLlength=input('interlobe sealing line length, m');%0.185497;
105 %InterlobeSLlength_98=127.153e-3;%InterlobeSLlength_231=375.720e-3;
106 %InterlobeSLlength_141_N=172.751e-3;%InterlobeSLlength_141_beta1=172.791e-3;
107 %InterlobeSLlength_141_beta2=196.147e-3;%InterlobeSLlength_141_beta3=195.47e-3;
108
109 %Calculations
110 Do1=Di1+GAPR(1)*2;
111 Do2=Di2+GAPR(1)*2;
112 pcd1=2*cd*z1/(z1+z2);
113 pcd2=2*cd*z2/(z1+z2);
114 Ri1=Di1/2;
115 Ri2=Di2/2;
116 L1=Di1*L_D1;
117 Lead1=pi*pcd1/tan(helix*pi/180);
118 Lead2=pi*pcd2/tan(helix*pi/180);
119 pitch1=Lead1/z1;
120 helix_outer1=rad2deg(atan(tan(deg2rad(helix))*Do1/pcd1));
121 helix_outer2=rad2deg(atan(tan(deg2rad(helix))*Do2/pcd2));
122 Vt1=pi*Di1*n1/60;
123 Vt2=pi*Di2*n2/60;
124 %Cusp area calculations
125 malecuspangle=2*rad2deg(acos((cd^2+(Do1/2)^2-(Do2/2)^2)/(2*(Do1/2)*cd)));
126 femalecuspangle=2*rad2deg(acos((cd^2+(Do2/2)^2-(Do1/2)^2)/(2*(Do2/2)*cd)));
127 %Calculation for variable clearance length
128 for i=1:196
129     AxialPosition(i)=pitch1+phi_inj(i)*pitch1/(360/z1);
130     dx(i)=(L1-AxialPosition(i))/cos(deg2rad(helix_outer1))+(L1-AxialPosition(i))/cos(deg2rad(
131         helix_outer2));
132     phi_inj(i+1)=phi_inj(i)+1;
133 end
134 dp_98_85=[9.32E+02,8.84E+02,6.17E+02,2.39E+02,-9.00E+01,-2.62E+02,-2.56E+02,...
135     -1.32E+02,3.10E+01,1.83E+02,3.10E+02,4.24E+02,4.95E+02,5.43E+02,5.78E+02,...
136     6.07E+02,6.31E+02,6.51E+02,6.70E+02,6.84E+02,6.99E+02,7.12E+02,7.23E+02,...
137     7.35E+02,7.45E+02,7.56E+02,7.66E+02,7.76E+02,7.84E+02,7.95E+02,8.03E+02,...
138     8.12E+02,8.22E+02,8.30E+02,8.39E+02,8.48E+02,8.57E+02,8.66E+02,8.74E+02,...
139     8.84E+02,8.93E+02,9.02E+02,9.11E+02,9.21E+02,9.30E+02,9.39E+02,9.49E+02,...
140     9.59E+02,9.68E+02,9.79E+02,9.88E+02,9.99E+02,1.01E+03,1.02E+03,1.03E+03,...
141     9.96E+02,9.71E+02,9.80E+02,9.89E+02,1.00E+03,1.01E+03,1.02E+03,1.03E+03,...
142     1.04E+03,1.05E+03,1.06E+03,1.07E+03,1.08E+03,1.10E+03,1.10E+03,1.09E+03,...
143     1.11E+03,1.12E+03,1.13E+03,1.14E+03,1.15E+03,1.17E+03,1.18E+03,1.19E+03,...
144     1.21E+03,1.22E+03,1.24E+03,1.25E+03,1.27E+03,1.29E+03,1.31E+03,1.33E+03,...
145     1.35E+03,1.37E+03,1.39E+03,1.40E+03,1.42E+03,1.44E+03,1.45E+03,1.47E+03,...
146     1.49E+03,1.51E+03,1.52E+03,1.54E+03,1.56E+03,1.58E+03,1.60E+03,1.62E+03,...
147     1.65E+03,1.67E+03,1.70E+03,1.73E+03,1.76E+03,1.79E+03,1.82E+03,1.86E+03,...
148     1.90E+03,1.94E+03,1.99E+03,2.03E+03,2.07E+03,2.11E+03,2.14E+03,2.16E+03,...
149     2.19E+03,2.21E+03,2.23E+03,2.25E+03,2.27E+03,2.29E+03,2.31E+03,2.34E+03,...
150     2.36E+03,2.39E+03,2.41E+03,2.44E+03,2.47E+03,2.49E+03,2.52E+03,2.55E+03,...
151     2.58E+03,2.61E+03,2.64E+03,2.67E+03,2.71E+03,2.74E+03,2.78E+03,2.81E+03,...
152     2.85E+03,2.89E+03,3.00E+03,3.11E+03,3.15E+03,3.20E+03,3.25E+03,3.30E+03,...
153     3.35E+03,3.40E+03,3.45E+03,3.51E+03,3.56E+03,3.79E+03,3.87E+03,3.94E+03,...
154     4.01E+03,4.08E+03,4.15E+03,4.23E+03,4.31E+03,4.39E+03,4.48E+03,4.56E+03,...
155     4.65E+03,4.75E+03,4.84E+03,4.94E+03,5.04E+03,5.15E+03,5.26E+03,5.33E+03,...
156     5.35E+03,5.47E+03,5.60E+03,5.73E+03,5.87E+03,6.01E+03,6.15E+03,6.31E+03,...
157     6.47E+03,6.63E+03,6.80E+03,6.98E+03,7.17E+03,7.37E+03,7.42E+03,7.62E+03,...
158     8.20E+03,9.15E+03,1.04E+04,1.19E+04,1.36E+04];

```

158 dp_98_10=[7.60E+02,7.63E+02,7.21E+02,6.32E+02,5.14E+02,3.91E+02,2.87E+02,...
159 2.22E+02,2.01E+02,2.30E+02,2.95E+02,3.88E+02,4.70E+02,5.21E+02,5.50E+02,...
160 5.69E+02,5.84E+02,5.95E+02,6.06E+02,6.15E+02,6.25E+02,6.33E+02,6.41E+02,...
161 6.50E+02,6.57E+02,6.65E+02,6.71E+02,6.79E+02,6.86E+02,6.93E+02,7.00E+02,...
162 7.07E+02,7.14E+02,7.21E+02,7.28E+02,7.34E+02,7.42E+02,7.49E+02,7.56E+02,...
163 7.63E+02,7.71E+02,7.78E+02,7.85E+02,7.93E+02,8.01E+02,8.08E+02,8.17E+02,...
164 8.24E+02,8.32E+02,8.41E+02,8.49E+02,8.57E+02,8.67E+02,8.75E+02,8.54E+02,...
165 8.65E+02,8.74E+02,8.82E+02,8.91E+02,9.00E+02,9.09E+02,9.18E+02,9.27E+02,...
166 9.37E+02,9.46E+02,9.56E+02,9.66E+02,9.76E+02,9.86E+02,9.97E+02,1.01E+03,...
167 1.02E+03,1.03E+03,1.04E+03,1.05E+03,1.06E+03,1.08E+03,1.09E+03,1.10E+03,...
168 1.11E+03,1.12E+03,1.14E+03,1.16E+03,1.18E+03,1.21E+03,1.23E+03,1.25E+03,...
169 1.28E+03,1.30E+03,1.32E+03,1.34E+03,1.35E+03,1.36E+03,1.38E+03,1.39E+03,...
170 1.41E+03,1.43E+03,1.45E+03,1.47E+03,1.48E+03,1.51E+03,1.52E+03,1.54E+03,...
171 1.57E+03,1.59E+03,1.61E+03,1.63E+03,1.66E+03,1.68E+03,1.71E+03,1.74E+03,...
172 1.77E+03,1.80E+03,1.83E+03,1.86E+03,1.89E+03,1.93E+03,1.96E+03,2.00E+03,...
173 2.03E+03,2.07E+03,2.10E+03,2.13E+03,2.17E+03,2.20E+03,2.23E+03,2.26E+03,...
174 2.29E+03,2.32E+03,2.36E+03,2.39E+03,2.42E+03,2.46E+03,2.49E+03,2.53E+03,...
175 2.56E+03,2.60E+03,2.64E+03,2.68E+03,2.72E+03,2.76E+03,2.80E+03,2.84E+03,...
176 2.88E+03,2.99E+03,3.03E+03,3.09E+03,3.14E+03,3.19E+03,3.25E+03,3.30E+03,...
177 3.36E+03,3.42E+03,3.48E+03,3.55E+03,3.61E+03,3.68E+03,3.75E+03,3.82E+03,...
178 3.90E+03,3.97E+03,4.08E+03,4.21E+03,4.30E+03,4.39E+03,4.48E+03,4.58E+03,...
179 4.68E+03,4.78E+03,4.89E+03,5.00E+03,5.11E+03,5.23E+03,5.35E+03,5.48E+03,...
180 5.61E+03,5.75E+03,5.89E+03,6.04E+03,6.19E+03,6.35E+03,6.52E+03,6.69E+03,...
181 6.87E+03,7.06E+03,7.26E+03,7.46E+03,7.68E+03,7.90E+03,8.03E+03,8.36E+03,...
182 8.94E+03,9.83E+03,1.09E+04,1.21E+04,1.34E+04];
183 dp_98_125=[9.31E+02,8.64E+02,5.13E+02,2.80E+01,-3.44E+02,-4.62E+02,-3.48E+02,...
184 -1.30E+02,7.60E+01,2.35E+02,3.59E+02,4.61E+02,5.26E+02,5.67E+02,5.99E+02,...
185 6.25E+02,6.47E+02,6.65E+02,6.81E+02,6.95E+02,7.09E+02,7.20E+02,7.31E+02,...
186 7.42E+02,7.53E+02,7.62E+02,7.72E+02,7.81E+02,7.91E+02,8.01E+02,8.09E+02,...
187 8.19E+02,8.28E+02,8.38E+02,8.46E+02,8.56E+02,8.65E+02,8.74E+02,8.83E+02,...
188 8.93E+02,9.02E+02,9.12E+02,9.22E+02,9.31E+02,9.40E+02,9.25E+02,8.90E+02,...
189 8.99E+02,9.07E+02,9.16E+02,9.25E+02,9.34E+02,9.44E+02,9.53E+02,9.61E+02,...
190 9.71E+02,9.80E+02,9.90E+02,1.00E+03,1.01E+03,1.02E+03,1.03E+03,1.04E+03,...
191 1.05E+03,1.06E+03,1.08E+03,1.09E+03,1.10E+03,1.11E+03,1.12E+03,1.12E+03,...
192 1.12E+03,1.13E+03,1.15E+03,1.16E+03,1.17E+03,1.19E+03,1.20E+03,1.21E+03,...
193 1.23E+03,1.24E+03,1.26E+03,1.28E+03,1.29E+03,1.31E+03,1.33E+03,1.35E+03,...
194 1.37E+03,1.39E+03,1.41E+03,1.42E+03,1.44E+03,1.46E+03,1.48E+03,1.49E+03,...
195 1.51E+03,1.53E+03,1.55E+03,1.57E+03,1.59E+03,1.61E+03,1.63E+03,1.65E+03,...
196 1.68E+03,1.71E+03,1.74E+03,1.77E+03,1.81E+03,1.85E+03,1.90E+03,1.95E+03,...
197 2.01E+03,2.07E+03,2.13E+03,2.20E+03,2.26E+03,2.33E+03,2.40E+03,2.46E+03,...
198 2.51E+03,2.55E+03,2.58E+03,2.60E+03,2.63E+03,2.65E+03,2.67E+03,2.70E+03,...
199 2.72E+03,2.75E+03,2.78E+03,2.80E+03,2.83E+03,2.86E+03,2.89E+03,2.92E+03,...
200 3.00E+03,3.11E+03,3.14E+03,3.18E+03,3.22E+03,3.26E+03,3.30E+03,3.35E+03,...
201 3.39E+03,3.44E+03,3.48E+03,3.53E+03,3.58E+03,3.63E+03,3.68E+03,3.73E+03,...
202 3.93E+03,4.02E+03,4.08E+03,4.15E+03,4.21E+03,4.28E+03,4.35E+03,4.43E+03,...
203 4.50E+03,4.58E+03,4.66E+03,4.74E+03,4.83E+03,4.92E+03,5.01E+03,5.10E+03,...
204 5.20E+03,5.30E+03,5.41E+03,5.51E+03,5.63E+03,5.74E+03,5.86E+03,5.99E+03,...
205 6.12E+03,6.25E+03,6.39E+03,6.53E+03,6.68E+03,6.84E+03,7.00E+03,7.17E+03,...
206 7.34E+03,7.53E+03,7.72E+03,7.91E+03,8.12E+03,8.34E+03,8.32E+03,8.53E+03,...
207 9.45E+03,1.11E+04,1.35E+04,1.63E+04,1.96E+04];
208 dp=[8.73E+02,8.91E+02,9.07E+02,9.17E+02,9.25E+02,9.29E+02,9.30E+02,...
209 9.28E+02,9.24E+02,9.18E+02,9.09E+02,8.99E+02,8.88E+02,8.75E+02,8.61E+02,...
210 8.48E+02,8.33E+02,8.19E+02,8.04E+02,7.89E+02,7.75E+02,7.62E+02,7.48E+02,...
211 7.37E+02,7.24E+02,7.14E+02,7.05E+02,6.96E+02,6.88E+02,6.82E+02,6.76E+02,...
212 6.72E+02,6.68E+02,6.66E+02,6.65E+02,6.65E+02,6.65E+02,6.67E+02,6.69E+02,...
213 6.72E+02,6.76E+02,6.81E+02,6.85E+02,6.92E+02,6.97E+02,7.05E+02,7.10E+02,...
214 7.19E+02,7.27E+02,7.34E+02,7.43E+02,7.51E+02,7.61E+02,7.68E+02,7.79E+02,...
215 7.87E+02,7.96E+02,8.06E+02,8.16E+02,8.25E+02,8.35E+02,8.44E+02,8.55E+02,...
216 8.65E+02,8.96E+02,8.82E+02,8.82E+02,8.91E+02,9.02E+02,9.13E+02,9.24E+02...

217 9.33E+02,9.46E+02,9.49E+02,9.70E+02,1.01E+03,1.05E+03,1.09E+03,1.13E+03,...
 218 1.17E+03,1.19E+03,1.21E+03,1.20E+03,1.20E+03,1.20E+03,1.20E+03,1.20E+03,...
 219 1.21E+03,1.22E+03,1.23E+03,1.24E+03,1.25E+03,1.26E+03,1.27E+03,1.29E+03,...
 220 1.30E+03,1.32E+03,1.33E+03,1.35E+03,1.36E+03,1.38E+03,1.40E+03,1.42E+03,...
 221 1.43E+03,1.45E+03,1.47E+03,1.49E+03,1.51E+03,1.53E+03,1.55E+03,1.57E+03,...
 222 1.60E+03,1.62E+03,1.64E+03,1.67E+03,1.70E+03,1.72E+03,1.75E+03,1.78E+03,...
 223 1.81E+03,1.84E+03,1.87E+03,1.90E+03,1.93E+03,1.96E+03,1.99E+03,2.01E+03,...
 224 2.04E+03,2.07E+03,2.10E+03,2.13E+03,2.16E+03,2.19E+03,2.22E+03,2.25E+03,...
 225 2.28E+03,2.31E+03,2.35E+03,2.38E+03,2.41E+03,2.45E+03,2.48E+03,2.52E+03,...
 226 2.56E+03,2.59E+03,2.63E+03,2.67E+03,2.72E+03,2.76E+03,2.80E+03,2.84E+03,...
 227 2.89E+03,2.94E+03,2.99E+03,3.00E+03,3.11E+03,3.19E+03,3.24E+03,3.30E+03,...
 228 3.36E+03,3.41E+03,3.47E+03,3.54E+03,3.60E+03,3.67E+03,3.74E+03,3.81E+03,...
 229 3.88E+03,3.96E+03,4.04E+03,4.11E+03,4.20E+03,4.28E+03,4.37E+03,4.46E+03,...
 230 4.56E+03,4.65E+03,4.75E+03,4.85E+03,4.96E+03,5.07E+03,5.18E+03,5.31E+03,...
 231 5.37E+03,5.48E+03,5.61E+03,5.75E+03,5.89E+03,6.04E+03,6.18E+03,6.34E+03,...
 232 6.50E+03,6.67E+03,6.81E+03,7.15E+03,7.68E+03];
 233 dp_141_10=[9.62E+02,9.77E+02,9.88E+02,9.92E+02,9.91E+02,9.87E+02,9.78E+02,...
 234 9.65E+02,9.50E+02,9.33E+02,9.13E+02,8.93E+02,8.71E+02,8.49E+02,8.26E+02,...
 235 8.05E+02,7.84E+02,7.65E+02,7.45E+02,7.28E+02,7.11E+02,6.98E+02,6.85E+02,...
 236 6.75E+02,6.66E+02,6.59E+02,6.53E+02,6.49E+02,6.48E+02,6.47E+02,6.47E+02,...
 237 6.50E+02,6.52E+02,6.57E+02,6.62E+02,6.68E+02,6.74E+02,6.81E+02,6.89E+02,...
 238 6.97E+02,7.05E+02,7.15E+02,7.22E+02,7.32E+02,7.41E+02,7.51E+02,7.59E+02,...
 239 7.69E+02,7.78E+02,7.88E+02,7.97E+02,8.06E+02,8.17E+02,8.25E+02,8.35E+02,...
 240 8.44E+02,8.54E+02,8.63E+02,8.73E+02,8.82E+02,8.93E+02,9.01E+02,9.13E+02,...
 241 9.21E+02,9.17E+02,9.25E+02,9.36E+02,9.46E+02,9.57E+02,9.67E+02,9.79E+02,...
 242 9.88E+02,9.99E+02,1.01E+03,1.03E+03,1.06E+03,1.10E+03,1.14E+03,1.18E+03,...
 243 1.21E+03,1.23E+03,1.24E+03,1.23E+03,1.22E+03,1.22E+03,1.22E+03,1.23E+03,...
 244 1.24E+03,1.25E+03,1.26E+03,1.27E+03,1.29E+03,1.30E+03,1.32E+03,1.33E+03,...
 245 1.35E+03,1.36E+03,1.38E+03,1.40E+03,1.41E+03,1.43E+03,1.45E+03,1.47E+03,...
 246 1.49E+03,1.51E+03,1.53E+03,1.55E+03,1.57E+03,1.59E+03,1.61E+03,1.64E+03,...
 247 1.66E+03,1.69E+03,1.71E+03,1.74E+03,1.77E+03,1.80E+03,1.83E+03,1.86E+03,...
 248 1.90E+03,1.93E+03,1.97E+03,2.00E+03,2.04E+03,2.07E+03,2.11E+03,2.14E+03,...
 249 2.18E+03,2.21E+03,2.24E+03,2.27E+03,2.30E+03,2.33E+03,2.36E+03,2.39E+03,...
 250 2.43E+03,2.46E+03,2.49E+03,2.53E+03,2.56E+03,2.60E+03,2.64E+03,2.67E+03,...
 251 2.71E+03,2.75E+03,2.79E+03,2.83E+03,2.87E+03,2.92E+03,2.99E+03,3.03E+03,...
 252 3.08E+03,3.13E+03,3.18E+03,3.26E+03,3.31E+03,3.37E+03,3.42E+03,3.48E+03,...
 253 3.54E+03,3.60E+03,3.67E+03,3.73E+03,3.80E+03,3.87E+03,3.94E+03,4.01E+03,...
 254 4.09E+03,4.17E+03,4.25E+03,4.33E+03,4.42E+03,4.50E+03,4.59E+03,4.68E+03,...
 255 4.78E+03,4.88E+03,4.99E+03,5.09E+03,5.20E+03,5.32E+03,5.43E+03,5.55E+03,...
 256 5.68E+03,5.81E+03,5.94E+03,6.09E+03,6.22E+03,6.38E+03,6.53E+03,6.70E+03,...
 257 6.86E+03,7.04E+03,7.11E+03,7.43E+03,8.10E+03];
 258 dp_141_125=[1.29E+03,1.24E+03,1.16E+03,1.08E+03,9.87E+02,8.98E+02,8.17E+02,...
 259 7.45E+02,6.86E+02,6.40E+02,6.08E+02,5.90E+02,5.79E+02,5.79E+02,5.86E+02,...
 260 5.97E+02,6.11E+02,6.26E+02,6.43E+02,6.59E+02,6.76E+02,6.91E+02,7.04E+02,...
 261 7.18E+02,7.30E+02,7.42E+02,7.52E+02,7.63E+02,7.73E+02,7.83E+02,7.93E+02,...
 262 8.01E+02,8.10E+02,8.20E+02,8.29E+02,8.38E+02,8.48E+02,8.56E+02,8.66E+02,...
 263 8.74E+02,8.85E+02,9.83E+02,9.96E+02,1.00E+03,9.74E+02,8.88E+02,9.11E+02,...
 264 9.26E+02,9.38E+02,9.49E+02,9.59E+02,9.69E+02,9.79E+02,9.91E+02,1.00E+03,...
 265 1.01E+03,1.02E+03,1.03E+03,1.05E+03,1.06E+03,1.07E+03,1.08E+03,1.09E+03,...
 266 1.09E+03,1.10E+03,1.11E+03,1.13E+03,1.14E+03,1.15E+03,1.17E+03,1.18E+03,...
 267 1.19E+03,1.22E+03,1.24E+03,1.27E+03,1.29E+03,1.31E+03,1.33E+03,1.35E+03,...
 268 1.36E+03,1.38E+03,1.38E+03,1.39E+03,1.40E+03,1.42E+03,1.44E+03,1.46E+03,...
 269 1.48E+03,1.50E+03,1.52E+03,1.54E+03,1.56E+03,1.58E+03,1.60E+03,1.63E+03,...
 270 1.65E+03,1.67E+03,1.70E+03,1.72E+03,1.75E+03,1.77E+03,1.80E+03,1.83E+03,...
 271 1.86E+03,1.89E+03,1.93E+03,1.97E+03,2.01E+03,2.06E+03,2.11E+03,2.17E+03,...
 272 2.22E+03,2.28E+03,2.34E+03,2.41E+03,2.47E+03,2.54E+03,2.60E+03,2.66E+03,...
 273 2.71E+03,2.74E+03,2.78E+03,2.81E+03,2.85E+03,2.88E+03,2.91E+03,2.94E+03,...
 274 2.98E+03,3.01E+03,3.05E+03,3.09E+03,2.98E+03,3.02E+03,3.06E+03,3.18E+03,...
 275 3.40E+03,3.43E+03,3.47E+03,3.52E+03,3.57E+03,3.62E+03,3.68E+03,3.73E+03,...

276 3.79E+03,3.85E+03,3.90E+03,3.97E+03,4.03E+03,4.10E+03,4.16E+03,4.23E+03,...
 277 4.30E+03,4.37E+03,4.45E+03,4.53E+03,4.61E+03,4.69E+03,4.77E+03,4.86E+03,...
 278 4.95E+03,5.04E+03,5.13E+03,5.23E+03,5.33E+03,5.43E+03,5.54E+03,5.65E+03,...
 279 5.77E+03,5.89E+03,6.01E+03,6.13E+03,6.27E+03,6.41E+03,6.55E+03,6.70E+03,...
 280 6.85E+03,7.00E+03,7.17E+03,7.34E+03,7.52E+03,7.70E+03,7.89E+03,8.08E+03,...
 281 8.30E+03,8.51E+03,8.73E+03,8.97E+03,9.21E+03,9.28E+03,9.68E+03,1.07E+04,...
 282 1.23E+04,1.41E+04,1.65E+04,1.92E+04,2.23E+04];
 283 dp_231_85=[6.99E+02,6.36E+02,4.98E+02,3.19E+02,1.39E+02,2.00E+00,-6.00E+01,...
 284 -3.50E+01,5.50E+01,1.79E+02,3.10E+02,4.12E+02,4.70E+02,4.92E+02,5.04E+02,...
 285 5.12E+02,5.21E+02,5.28E+02,5.38E+02,5.46E+02,5.54E+02,5.62E+02,5.70E+02,...
 286 5.78E+02,5.84E+02,5.91E+02,5.99E+02,6.06E+02,6.12E+02,6.17E+02,6.24E+02,...
 287 6.30E+02,6.37E+02,6.44E+02,6.50E+02,6.58E+02,6.64E+02,6.71E+02,6.77E+02,...
 288 6.85E+02,6.92E+02,6.98E+02,7.07E+02,7.13E+02,7.20E+02,7.27E+02,7.36E+02,...
 289 7.37E+02,7.40E+02,7.47E+02,7.54E+02,7.63E+02,7.69E+02,7.78E+02,8.11E+02,...
 290 8.26E+02,8.34E+02,8.44E+02,8.52E+02,8.60E+02,8.71E+02,8.80E+02,8.89E+02,...
 291 8.99E+02,9.10E+02,9.19E+02,9.27E+02,9.40E+02,9.50E+02,9.61E+02,9.71E+02,...
 292 9.83E+02,9.94E+02,1.00E+03,1.02E+03,1.03E+03,1.04E+03,1.05E+03,1.07E+03,...
 293 1.08E+03,1.09E+03,1.11E+03,1.13E+03,1.15E+03,1.16E+03,1.18E+03,1.19E+03,...
 294 1.21E+03,1.23E+03,1.24E+03,1.26E+03,1.27E+03,1.29E+03,1.30E+03,1.32E+03,...
 295 1.34E+03,1.36E+03,1.37E+03,1.39E+03,1.41E+03,1.43E+03,1.45E+03,1.47E+03,...
 296 1.49E+03,1.51E+03,1.54E+03,1.56E+03,1.58E+03,1.61E+03,1.64E+03,1.67E+03,...
 297 1.70E+03,1.73E+03,1.76E+03,1.79E+03,1.83E+03,1.86E+03,1.90E+03,1.93E+03,...
 298 1.97E+03,2.00E+03,2.04E+03,2.07E+03,2.10E+03,2.14E+03,2.17E+03,2.20E+03,...
 299 2.23E+03,2.27E+03,2.30E+03,2.33E+03,2.36E+03,2.40E+03,2.43E+03,2.46E+03,...
 300 2.50E+03,2.53E+03,2.58E+03,2.62E+03,2.66E+03,2.70E+03,2.74E+03,2.78E+03,...
 301 2.83E+03,2.82E+03,2.86E+03,2.90E+03,2.95E+03,3.00E+03,3.05E+03,3.10E+03,...
 302 3.15E+03,3.21E+03,3.26E+03,3.32E+03,3.38E+03,3.44E+03,3.51E+03,3.57E+03,...
 303 3.64E+03,3.71E+03,3.78E+03,3.85E+03,3.93E+03,4.01E+03,4.09E+03,4.17E+03,...
 304 4.26E+03,4.35E+03,4.44E+03,4.54E+03,4.64E+03,4.74E+03,4.85E+03,4.96E+03,...
 305 5.07E+03,5.19E+03,5.31E+03,5.44E+03,5.58E+03,5.71E+03,5.86E+03,5.91E+03,...
 306 6.07E+03,6.23E+03,6.40E+03,6.58E+03,6.76E+03,6.95E+03,7.15E+03,7.26E+03,...
 307 7.50E+03,7.99E+03,8.72E+03,9.60E+03,1.06E+04];
 308 dp_231_10=[6.90E+02,6.53E+02,5.61E+02,4.29E+02,2.81E+02,1.39E+02,3.30E+01,...
 309 -1.30E+01,0.00E+00,7.40E+01,1.90E+02,3.17E+02,4.14E+02,4.71E+02,5.02E+02,...
 310 5.18E+02,5.26E+02,5.32E+02,5.39E+02,5.45E+02,5.51E+02,5.59E+02,5.65E+02,...
 311 5.71E+02,5.78E+02,5.86E+02,5.92E+02,5.98E+02,6.05E+02,6.11E+02,6.16E+02,...
 312 6.23E+02,6.30E+02,6.36E+02,6.43E+02,6.49E+02,6.57E+02,6.62E+02,6.69E+02,...
 313 6.76E+02,6.83E+02,6.90E+02,6.97E+02,7.05E+02,7.11E+02,7.17E+02,7.26E+02,...
 314 7.28E+02,7.33E+02,7.40E+02,7.48E+02,7.56E+02,7.62E+02,7.71E+02,8.00E+02,...
 315 8.08E+02,8.16E+02,8.25E+02,8.34E+02,8.41E+02,8.52E+02,8.61E+02,8.69E+02,...
 316 8.80E+02,8.88E+02,8.99E+02,9.07E+02,9.18E+02,9.29E+02,9.39E+02,9.49E+02,...
 317 9.60E+02,9.71E+02,9.81E+02,9.93E+02,1.01E+03,1.02E+03,1.03E+03,1.04E+03,...
 318 1.05E+03,1.07E+03,1.09E+03,1.11E+03,1.13E+03,1.15E+03,1.17E+03,1.19E+03,...
 319 1.20E+03,1.22E+03,1.23E+03,1.24E+03,1.26E+03,1.27E+03,1.29E+03,1.30E+03,...
 320 1.32E+03,1.34E+03,1.36E+03,1.38E+03,1.39E+03,1.41E+03,1.43E+03,1.45E+03,...
 321 1.47E+03,1.49E+03,1.52E+03,1.54E+03,1.56E+03,1.58E+03,1.61E+03,1.64E+03,...
 322 1.67E+03,1.70E+03,1.73E+03,1.76E+03,1.79E+03,1.82E+03,1.85E+03,1.89E+03,...
 323 1.92E+03,1.96E+03,1.99E+03,2.03E+03,2.07E+03,2.10E+03,2.14E+03,2.18E+03,...
 324 2.21E+03,2.25E+03,2.29E+03,2.32E+03,2.36E+03,2.40E+03,2.43E+03,2.47E+03,...
 325 2.51E+03,2.55E+03,2.60E+03,2.64E+03,2.68E+03,2.72E+03,2.77E+03,2.81E+03,...
 326 2.86E+03,2.87E+03,2.91E+03,2.96E+03,3.01E+03,3.06E+03,3.11E+03,3.16E+03,...
 327 3.22E+03,3.27E+03,3.33E+03,3.39E+03,3.45E+03,3.52E+03,3.58E+03,3.65E+03,...
 328 3.72E+03,3.79E+03,3.87E+03,3.95E+03,4.03E+03,4.11E+03,4.19E+03,4.28E+03,...
 329 4.37E+03,4.47E+03,4.57E+03,4.67E+03,4.77E+03,4.88E+03,4.99E+03,5.11E+03,...
 330 5.23E+03,5.36E+03,5.49E+03,5.63E+03,5.77E+03,5.91E+03,6.07E+03,6.23E+03,...
 331 6.39E+03,6.56E+03,6.75E+03,6.93E+03,7.13E+03,7.33E+03,7.55E+03,7.69E+03,...
 332 7.98E+03,8.52E+03,9.30E+03,1.02E+04,1.13E+04];
 333 dp_231_125=[6.93E+02,6.02E+02,4.10E+02,1.66E+02,-6.30E+01,-2.10E+02,-2.35E+02,...
 334 -1.40E+02,2.20E+01,2.00E+02,3.48E+02,4.47E+02,4.88E+02,4.99E+02,5.04E+02,...

```

335 5.11E+02,5.18E+02,5.26E+02,5.35E+02,5.44E+02,5.51E+02,5.60E+02,5.67E+02,...
336 5.74E+02,5.80E+02,5.88E+02,5.96E+02,6.02E+02,6.08E+02,6.14E+02,6.20E+02,...
337 6.26E+02,6.33E+02,6.40E+02,6.47E+02,6.53E+02,6.61E+02,6.67E+02,6.73E+02,...
338 6.82E+02,6.88E+02,6.95E+02,7.03E+02,7.09E+02,7.17E+02,7.24E+02,7.23E+02,...
339 7.28E+02,7.36E+02,7.44E+02,7.68E+02,7.90E+02,7.96E+02,8.07E+02,8.14E+02,...
340 8.23E+02,8.32E+02,8.41E+02,8.50E+02,8.58E+02,8.68E+02,8.78E+02,8.87E+02,...
341 8.97E+02,9.07E+02,9.18E+02,9.26E+02,9.38E+02,9.48E+02,9.59E+02,9.70E+02,...
342 9.82E+02,9.92E+02,1.00E+03,1.02E+03,1.03E+03,1.04E+03,1.05E+03,1.07E+03,...
343 1.08E+03,1.09E+03,1.11E+03,1.13E+03,1.15E+03,1.16E+03,1.18E+03,1.19E+03,...
344 1.21E+03,1.22E+03,1.24E+03,1.25E+03,1.27E+03,1.28E+03,1.30E+03,1.32E+03,...
345 1.33E+03,1.35E+03,1.37E+03,1.39E+03,1.41E+03,1.43E+03,1.45E+03,1.47E+03,...
346 1.49E+03,1.51E+03,1.53E+03,1.56E+03,1.59E+03,1.61E+03,1.65E+03,1.68E+03,...
347 1.72E+03,1.75E+03,1.79E+03,1.83E+03,1.86E+03,1.91E+03,1.95E+03,1.99E+03,...
348 2.04E+03,2.08E+03,2.13E+03,2.18E+03,2.23E+03,2.27E+03,2.32E+03,2.37E+03,...
349 2.41E+03,2.45E+03,2.49E+03,2.53E+03,2.57E+03,2.60E+03,2.64E+03,2.68E+03,...
350 2.72E+03,2.77E+03,2.81E+03,2.85E+03,2.89E+03,2.89E+03,2.92E+03,2.96E+03,...
351 3.01E+03,3.05E+03,3.10E+03,3.14E+03,3.19E+03,3.24E+03,3.29E+03,3.35E+03,...
352 3.40E+03,3.46E+03,3.52E+03,3.58E+03,3.64E+03,3.70E+03,3.77E+03,3.84E+03,...
353 3.91E+03,3.98E+03,4.05E+03,4.13E+03,4.21E+03,4.29E+03,4.38E+03,4.46E+03,...
354 4.56E+03,4.65E+03,4.75E+03,4.85E+03,4.95E+03,5.06E+03,5.17E+03,5.29E+03,...
355 5.41E+03,5.53E+03,5.66E+03,5.79E+03,5.93E+03,6.08E+03,6.23E+03,6.39E+03,...
356 6.55E+03,6.72E+03,6.90E+03,7.08E+03,7.27E+03,7.48E+03,7.69E+03,7.76E+03,...
357 8.04E+03,8.77E+03,9.97E+03,1.15E+04,1.32E+04];
358
359 %Drag loss in radial clearance
360 %Male rotor calculations
361 for j=1:11
362     r1(1)=0;
363     for i=1:196
364         u1(i)=(Vt1/GAPR(j))*r1(i)+(1/(2*mu))*dp(i)/dx(i)*(r1(i)^2-GAPR(j)*r1(i));%velocity[m/s]
365         tau_radial1(i)=(mu*Vt1/GAPR(j)+(1/2)*(2*r1(i)-GAPR(j))*dp(i)/dx(i));%shear stress[N/m2]
366         r1(i+1)=r1(i)+GAPR(j)/1000;
367     end
368     T_radial1(j)=tau_radial1(i)*B1/10*Lead1*Ri1;%torque[Nm]
369     power_loss_radial1(j)=2*pi*n1*T_radial1(j)/60*z1;%[W]
370     GAPR(j+1)=GAPR(j)+(GAPR(10)-GAPR(1))/10;
371 end
372 power_loss_radial1=sum(power_loss_radial1(1:10));
373 power_loss_radial1_corrected=power_loss_radial1*(1-malecusangle/360)*(1-phi_inj(1)/phi1c);%[W]
374 %Female rotor calculations
375 for j=1:10
376     r2(1)=0;
377     for i=1:196
378         u2(i)=(Vt2/GAPR(j))*r2(i)+(1/(2*mu))*dp(i)/dx(i)*(r2(i)^2-GAPR(j)*r2(i));%velocity[m/s]
379         tau_radial2(i)=(mu*Vt2/GAPR(j)+(1/2)*(2*r2(i)-GAPR(j))*dp(i)/dx(i));%shear stress[N/m2]
380         r2(i+1)=r2(i)+GAPR(j)/1000;
381     end
382     T_radial2(j)=tau_radial2(i)*B2/10*Lead2*Ri2;%torque[Nm]
383     power_loss_radial2(j)=2*pi*n2*T_radial2(j)/60*z2;%[W]
384     GAPR(j+1)=GAPR(j)+(GAPR(10)-GAPR(1))/10;
385 end
386 power_loss_radial2=sum(power_loss_radial2(1:10));
387 power_loss_radial2_corrected=power_loss_radial2*(1-femalecusangle/360)*(1-phi_inj(1)/phi1c);%[W]
388
389 %Total radial power loss [W]
390 TotalPowerLossRadial_Watts=power_loss_radial1_corrected+power_loss_radial2_corrected
391
392 %Drag loss in discharge axial clearance
393 RotorArea1=((pi/4*(Do1^2-Dr1^2))-RotorGasArea1*z1)/z1;

```

```

394 RotorArea2=((pi/4*(Do2^2-Dr2^2))-RotorGasArea2*z2)/z2;
395 dr1=sqrt(RotorArea1);
396 dr2=sqrt(RotorArea2);
397 for i=1:196
398     tau_axial1(i)=(mu*Vt1/GAPA)+(1/2)*(GAPA)*dp(i)/dr1;%shear stress[N/m2]
399     tau_axial2(i)=(mu*Vt2/GAPA)+(1/2)*(GAPA)*dp(i)/dr2;%shear stress[N/m2]
400 end
401 tau_axial1=sum(tau_axial1(1:196))*(moil/rho_oil)/((moil/rho_oil)+(mair/rho_air));
402 tau_axial2=sum(tau_axial2(1:196))*(moil/rho_oil)/((moil/rho_oil)+(mair/rho_air));
403
404 T_axial1=tau_axial1*RotorArea1*(Do1+Dr1)/4*z1;%torque[Nm]
405 T_axial2=tau_axial2*RotorArea2*(Do2+Dr2)/4*z2;%torque[Nm]
406
407 power_loss_axial1=T_axial1*2*pi*n1/60;%[W]
408 power_loss_axial2=T_axial2*2*pi*n2/60;%[W]
409 TotalPowerLossAxial_Watts=power_loss_axial1+power_loss_axial2
410
411 %Drag Loss in interlobe clearance
412 for i=1:196
413     tau_interlobe(i)=(mu*z1/z2/B2)+(B2/2)*dp(i)/InterlobeSLlength;%shear stress[N/m2]
414 end
415 tau_interlobe=sum(tau_interlobe(1:i));
416 %Rotor interlobe power loss [W]
417 T_interlobe=tau_interlobe*InterlobeLeakageArea*pcdl/2;%torque[Nm]
418 TotalPowerLossInterlobe_Watts=2*pi*n1*T_interlobe/60*z1%[W]
419
420 %Total drag loss
421 DragPowerLoss_Watts=TotalPowerLossAxial_Watts+TotalPowerLossRadil_Watts+
    TotalPowerLossInterlobe_Watts

```

Guide to use the drag loss computer-programme:

To effectively model and analyse the compressor's operation and process, it is required to define various input parameters that encompass both operational and geometric aspects.

Operational Parameters:

- Compressor suction pressure (p1) and discharge pressure (p2)
- Rotational speed of male rotor (n1)
- Anticipated volume flow rate of air at the suction inlet (vair)
- The ratio of oil mass to air mass in the mixture (mass-ratio)
- The density of the oil used in the compressor (rho-oil)
- The kinematic viscosity of the oil used (nu)

Geometric Parameters:

- Number of lobes of male rotor (z1) and female rotor (z2)
- Axial clearance gap at high-pressure end (GAPA)
- Interlobe clearance gap between the rotors (GAPR)

- Radial clearance gap at rotor leading tip (GAPR(1))
- Radial clearance gap at rotor trailing tip (GAPR(10))
- Top land width of the male rotor (B1) and female rotor (B2)
- Outer diameter of the male rotor (Di1) and female rotor (Di2)
- Root diameter of the male rotor (Dr1) and female rotor (Dr2)
- Centre distance between the rotors (cd)
- Length to diameter ratio (L-D1)
- Helix angle at pitch (helix)
- Screw wrap angle (phi1), angle of the compression end (phi1c) and oil injection angle (phi-inj)
- Interlobe leakage area (InterlobeLeakageArea) and interlobe sealing line length (InterlobeSLlength)
- Gas area between male rotor (RotorGasArea1) and female rotor lobes (RotorGasArea2)
- Differential pressure values (dp) for each compressor size and pressure ratio. Like, dp-98-85, represent differential pressure for 98 size compressor at 8.5 pressure ratio.

Various geometric parameters are specified as comments at corresponding lines within the program for distinct compressor sizes (98, 141, and 231) and various rotor profiles (N, beta-1, beta-2, and beta-3). These parameters collectively define the compressor's characteristics, operation, and geometry, allowing for accurate modelling and analysis of its performance.

The outlined method involves several distinct steps in the analysis process:

Calculation of Geometric Parameters: The initial step encompasses the calculation of essential geometric attributes such as tip velocities, lead, pitch, and helix angle at the outer diameter of the rotors. These standard geometric calculations lay the foundation for subsequent analysis.

Cusp Angle Calculation: Following the geometric calculations, cusp angles for both male and female rotors are computed. These angles play a pivotal role in considering the actual radial clearance gap that covers the rotors within the housing. This finer calculation is integral to accounting for the actual behaviour of the compressor.

Varying Axial Position Calculation: The next stage involves determining the varying axial position of the rotor starting from the angle of oil injection. This information is crucial for calculating the sealing line length as a function of rotor rotation angle.

Pressure Variation and Gradient Calculation: Utilizing SCORPATH data, the pressure variation across rotor rotation angles is acquired. This information, coupled with the length variation calculated earlier, aids in defining the pressure gradient that influences the drag losses.

Drag Loss Calculations: The drag loss calculation begins with the radial clearance, followed by calculations for axial clearance and interlobe clearance. These sequential steps facilitate a comprehensive understanding of the drag losses within different clearances.

Shear Area Calculation: The torque calculations necessitate the computation of shear areas for different clearances. The shear area for the radial clearance is determined using the product of top land width and rotor lead. The axial clearance's shear area is calculated by subtracting the gas area (obtained from SCORPATH) from the total annular area. The interlobe clearance's shear area is based on the leakage area calculated in SCORPATH.

Oil-to-Gas Mass Ratio Consideration: To account for the effect of the oil-to-gas mass ratio, the shear stress calculated for discharge axial clearance is multiplied by the mass ratio between oil and gas. This adjustment ensures that the analysis captures the realistic behaviour that arises from alterations in oil flow rate, offering a more comprehensive understanding of the performance's response to changing operational parameters.

This stepwise approach demonstrates the intricate process of analysing drag losses, including the integration of geometric, fluid dynamics, and operational considerations to provide a holistic view of the compressor's behaviour.

References

- Abdan, S., N. Stosic, A. Kovacevic, I. Smith, and N. Asati
2022. Oil drag loss in oil-flooded, twin-screw compressors. *Proceedings of the Institution of Mechanical Engineers, Part E: Journal of Process Mechanical Engineering*, P. 09544089221115493. SAGE Publications Sage UK: London, England.
- Basha, N., A. Kovacevic, N. Stosic, and I. Smith
2018. Effect of oil-injection on twin screw compressor performance. In *IOP Conference Series: Materials Science and Engineering*, volume 425, P. 012009. IOP Publishing.
- Bell, I. H., D. Ziviani, V. Lemort, C. R. Bradshaw, M. Mathison, W. T. Horton, J. E. Braun, and E. A. Groll
2020. PDSim: A general quasi-steady modeling approach for positive displacement compressors and expanders. *International Journal of Refrigeration*, 110:310–322. Elsevier.
- Bertini, L., L. Carmignani, and F. Frendo
2014. Analytical model for the power losses in rubber V-belt continuously variable transmission (CVT). *Mechanism and Machine Theory*, 78:289–306. Elsevier.
- Brown, R. N.
1997. *Compressors: Selection and sizing*. Gulf Professional Publishing.
- Cengel, Y. and J. Cimbala
2013. *Fluid Mechanics Fundamentals and Applications (SI units)*. McGraw Hill.
- Chaprabazaar
2022. Chapra bazaar. **url:** <https://chaprabazaar.blogspot.com/2018/09/lobe-compressor.html>. visited on 16/08/2022.
- Chukanova, E.
2016. *Modelling of screw compressor plant operation under intermittent conditions*. PhD thesis, City, University of London.
- Compressed-Air-Best-Practices
2022. Compressed Air Best Practices. **url:** <https://www.airbestpractices.com>.

com/sites/default/files/IMSACV%20Schematic%20copy.png. visited on 16/08/2022.

Compressed-Air-Blog

2022. How it Works: Liquid Ring Pump. **url:** <https://www.thecompressedairblog.com/how-it-works-liquid-ring-pump>. visited on 16/08/2022.

Deipenwisch, R. and K. Kauder

1999. Oil as a design parameter in screw. type compressors: oil distribution and power losses caused by oil in the working chamber of a screw-type compressor. In *IMECHE Conference Transactions*, volume 6, Pp. 49–58. Mechanical Engineering Publications.

EDUCBA

2022. Uncertainty formula. **url:** <https://www.educba.com/uncertainty-formula/>. accessed in December 2022.

El-Ibiary, Y.

2003. An accurate low-cost method for determining electric motors' efficiency for the purpose of plant energy management. *IEEE transactions on industry applications*, 39(4):1205–1210. IEEE.

Electricalvolt

2022. The electrical volt website for understanding of the current transformer measurement inaccuracy. **url:** <https://www.electricalvolt.com/2020/10/what-is-the-difference-between-0-2-and-0-2s-class-ct/#:~:text=A%200.2S%20CT%20has,be%20guaranteed%20from%205%25%20loading>. accessed in June 2022.

Engelke, T.

2011. *Einfluss der Elastomer-Schmierstoff-Kombination auf das Betriebsverhalten von Radialwellendichtringen*. PhD thesis, Hannover: Gottfried Wilhelm Leibniz Universität Hannover.

Fleming, J. S., Y. Tang, and G. Cook

1998. The twin helical screw compressor part 2: a mathematical model of the working process. *Proceedings of the institution of mechanical engineers, Part C: journal of mechanical engineering science*, 212(5):369–380. SAGE Publications Sage UK: London, England.

Frölich, D., B. Magyar, and B. Sauer

2014. A comprehensive model of wear, friction and contact temperature in radial shaft seals. *Wear*, 311(1-2):71–80. Elsevier.

- Fujiwara, M., K. Kasuya, T. Matsunaga, and M. Watanabe
 1984. Computer modeling for performance analysis of rotary screw compressor. In *International Compressor Engineering Conference*, number 503, Pp. 536–543. Purdue e-Pubs.
- Gardner, J. W.
 1969. Variable lead compressor. US Patent 3,424,373.
- GMI
 2022. Oil Filled Air Compressor Market Analysis - Industry Size Report 2024. url: <https://www.gminsights.com/industry-analysis/stationary-air-compressor-market>. visited on 10/08/2022.
- Gradu, M.
 2000. Tapered roller bearings with improved efficiency and high power density for automotive transmissions. *SAE transactions*, Pp. 1696–1705. JSTOR.
- Gräßer, M. and A. Brümmer
 2014. An analytic model of the incompressible one-phase clearance flow in liquid injected screw expanders. In *9th International Conference on Screw Machines, VDI Bericht 2228, Dortmund, Germany*, Pp. 71–89.
- Gräßer, M. and A. Brümmer
 2015. Influence of liquid in clearances on the operational behaviour of twin screw expanders. In *IOP Conference Series: Materials Science and Engineering*, volume 90, P. 012060. IOP Publishing.
- Gräßer, M. and A. Brümmer
 2016. Influence of water and oil clearance flow on the operational behavior of screw expanders. *Proceedings of the Institution of Mechanical Engineers, Part E: Journal of Process Mechanical Engineering*, 23(1):38–46. SAGE Publications Sage UK: London, England.
- Gray, L., T. Stratman, B. Conley, B. Ransdell, and D. Peana
 2018. Complex screw rotors. US Patent App. 15/760,086.
- Hamrock, B. J., S. R. Schmid, and B. O. Jacobson
 2004. *Fundamentals of fluid film lubrication*. CRC press.
- Hanjalic, K. and N. Stosic
 1997. Development and optimization of screw machines with a simulation model- Part ii: Thermodynamic performance simulation and design optimization. *Journal of fluids engineering*, 119(3):664–670. American Society of Mechanical Engineers.
- Harris, T. and M. Kotzalas
 2007. *Rolling Bearing Analysis: Essential Concepts of Bearing Technology*. CRC Press, Boca Raton.

- Hauser, J., M. Beinert, and D. Huettermann
2016. High Pressure, Single Stage Rotor. US Patent App. 14/600,997.
- Hauser, J., A. Bruemmer, and K. Kauder
2008. Rotor profile generation and optimization of screw machines using nurbs. In *International Compressor Engineering Conference*, number 1861. Purdue e-Pubs.
- He, Z., T. Wang, X. Wang, X. Peng, and Z. Xing
2018. Experimental investigation into the effect of oil injection on the performance of a variable speed twin-screw compressor. *Energies*, 11(6):1342. MDPI.
- Helpertz, M.
2003. *Methode zur stochastischen Optimierung von Schraubenrotorprofilen*. PhD thesis, Universität Dortmund.
- Huang, C.-Y.
2015. *New Twin Screw Compressor Design by Deviation Function Method*. PhD thesis, UCLA.
- Hughes, A. and B. Drury
2019. *Electric motors and drives: fundamentals, types and applications*. Newnes.
- IMARC
2021. Screw Compressor Market: Global Industry Trends, Share, Size, Growth, Opportunity and Forecast 2021-2026. [url: https://www.imarcgroup.com/screw-compressor-market](https://www.imarcgroup.com/screw-compressor-market). visited on 05/12/2021.
- Jacobs, J. S.
2006. Variable Speed Tri-Rotor Screw Compression Technology. In *International Compressor Engineering Conference*, number 1825. Purdue e-Pubs.
- Jelaska, D. T.
2012. *Gears and gear drives*. John Wiley & Sons.
- Kátai, L. and I. Szabó
2015. Identification of V-belt power losses with temperature measurement. *Journal of Mechanical Science and Technology*, 29(8):3195–3203. Springer.
- Kauder, K., M. Helpertz, B. Reusch, and S. Berlik
2002. Optimisation methods for rotors of twin-screw compressors. *VDI BERICHTE*, 1715:29–50. VDI.
- Knežević, D., V. Savić, et al.
2006. Mathematical modeling of changing of dynamic viscosity, as a function of temperature and pressure, of mineral oils for hydraulic systems. *Facta Universitatis. Series. Mechanical Engineering (Serbia)*.

Kovacevic, A. and N. Stosic

2013. Grid generation for screw compressors with variable geometry rotors. *International Journal of Aerospace and Lightweight Structures*, 3(2). Research Publishing.

Kovacevic, A., N. Stosic, and I. Smith

1999. Development of CAD-CFD interface for screw compressor design. In *IMECHE Conference Transactions*, volume 6, Pp. 757–768. Mechanical Engineering Publications.

Kovacevic, A., N. Stosic, and I. Smith

2007. *Screw compressors: Three Dimensional Computational Fluid Dynamics and Solid Fluid Interaction*, volume 46. Springer Science & Business Media.

Kovacevic, A., N. Stosic, and I. K. Smith

2002. CFD analysis of screw compressor performance. *Advances of CFD in Fluid Machinery Design*. Professional Engineering Publishing of IMechE, London.

Liu, Y., C. Hung, and Y. Chang

2010. Design optimization of scroll compressor applied for frictional losses evaluation. *International Journal of Refrigeration*, 33(3):615–624. Elsevier.

Lysholm, A.

1967. Screw rotor machine. US Patent 3,314,598.

MATLAB

2022. The mathworks, inc. **url:** <https://matlab.mathworks.com/>. Version R2022b.

Mechanical-Jungle

2022. Construction of Vane Compressor. **url:** <https://mechanicaljungle.com/vane-blower-compressor-construction-of-vane-compressor-working-of-vane-compressor/>. visited on 10/08/2022.

Mehltretter, N. A.

2014. Applying variable speed compressors in multiple compressor applications—application success stories and improvement stories. *Energy Engineering*, 111(2):25–42. Taylor & Francis.

O’Neill, P. A.

1993. *Industrial Compressors, Theory and Equipment*. Butterworth-Heinemann, Oxford.

Persson, J. E.

1968. Screw rotor machines and profiles. US Patent 3,414,189.

- Prasanna
2023. Engineering hub. **url:** <https://engihub.com/air-oil-flow-in-screw-air-compressor/>. accessed in March 2023.
- Raimondi, A. and J. Boyd
1958. A solution for the finite journal bearing and its application to analysis and design: Iii. *ASLE Transactions*, 1(1):194–209. Taylor & Francis.
- Rane, S.
2015. *Grid generation and CFD analysis of variable geometry screw machines*. PhD thesis, City University London.
- Read, M., I. Smith, and N. Stosic
2017. Internally geared screw machines with ported end plates. In *IOP Conference Series: Materials Science and Engineering*, volume 232, P. 012058. IOP Publishing.
- Ref-Wiki
2022. Construction of vane compressor. **url:** <https://www.ref-wiki.com/technical-information/145-compressors/31166-sliding-and-rotary-vane-compressors.html>. visited on 12/08/2022.
- Rinder, L.
1979. *Schraubenverdichter (Screw Compressors)*. Springer Verlag, New York.
- Sakun, I.
1960. *Vintovie kompresorii (Screw Compressors)*. Mashinostroenie Leningrad.
- Sangfors, B.
1984. Computer simulation of the oil injected twin screw compressor. In *International Compressor Engineering Conference*, number 502. Purdue e-Pubs.
- Schibbye, L.
1970. Improvements in and relating to rotary positive displacement machines of the intermeshing screw type and rotors therefor. GB Patent App. 3,421,766 A.
- Schiffmann, J.
2014. Small-scale and oil-free turbocompressor for refrigeration applications. In *International Compressor Engineering Conference*, number 2354. Purdue e-Pubs.
- Singh, P. J. and A. D. Onuschak
1984. A comprehensive, computerized method for twin-screw rotor profile generation and analysis. In *International Compressor Engineering Conference*, number 501. Purdue e-Pubs.
- Sirovỳ, M., Z. Peroutka, J. Molnár, J. Michalík, and M. Byrtus
2011. Sophisticated software for design and optimization of variable speed drives

for high-power pumps: Hydrodynamic coupling versus frequency converter. In *IECON 2011-37th Annual Conference of the IEEE Industrial Electronics Society*, Pp. 955–960. IEEE.

SKF

2018. The SKF model for calculating the frictional moment, Retrieved from. **url:** https://www.skf.com/binaries/pub110/Images/The%20SKF%20model%20for%20calculating%20the%20frictional%20moment_tcm_12-299767_tcm_110-299767.pdf. visited on 21/06/2018.

Stosic, N.

1996. Rotary compressor. GB Patent 9610289.2.

Stosic, N.

2005. SCORPATH - Screw Compressor Optimal Rotor Profiles and Thermodynamics. **url:** <http://www.staff.city.ac.uk/~ra600/DISCO/DISCO%20SCORPATH.htm>.

Stosic, N. and K. Hanjalic

1997. Development and optimization of screw machines with a simulation model-part I: Profile generation. *Journal of fluids engineering*, 119(3):659–663. American Society of Mechanical Engineers.

Stosic, N., K. Hanjalic, J. Koprivica, N. Lovren, and M. Ivanovic

1986. CAD of screw compressor elements. *Strojarstvo Journal Zagreb*, 28:181.

Stošić, N., L. Milutinović, K. Hanjalić, and A. Kovačević

1992. Investigation of the influence of oil injection upon the screw compressor working process. *International Journal of Refrigeration*, 15(4):206–220. Elsevier.

Stosic, N., I. Smith, and A. Kovacevic

2005. *Screw Compressors: Mathematical Modelling and Performance Calculation*. Springer Science & Business Media.

Stosic, N., I. K. Smith, and A. Kovacevic

2003. Optimisation of screw compressors. *Applied Thermal Engineering*, 23(10):1177–1195. Elsevier.

Tang, Y.

1995. *Computer aided design of twin screw compressors*. PhD thesis, University of Strathclyde.

Tu, M.

2016. Validation and modeling of power losses of NJ406 cylindrical roller bearings. Master of Science Thesis.

Vaidya, A.

2019. Screw rotor with high lobe count. US Patent 10,436,196.

Vasuthevan, H. and A. Brümmer

2018. Multiphase-flow simulation of a rotating rectangular profile within a cylinder in terms of hydraulic loss mechanisms. In *IOP Conference Series: Materials Science and Engineering*, volume 425, P. 012002. IOP Publishing.

Vert

2021. Vert. [url: https://www.vertrotors.com/](https://www.vertrotors.com/). visited on 17/09/2021.

Wu, W. and Q. Feng

2008. Leakage paths two type of meshing pairs in single screw compressors. In *International Compressor Engineering Conference, Purdue*, number 1864. Purdue e-Pubs.

Xing, Z.

2000. *Screw Compressors: Theory, Design and Application*. China Machine Press, Beijing.

Yen, Y.

2022. Yes yen. [url: https://yesyen.com/compressor_types.php](https://yesyen.com/compressor_types.php). visited on 06/05/2021.

Zaytsev, D. and C. I. Ferreira

2005. Profile generation method for twin screw compressor rotors based on the meshing line. *International Journal of Refrigeration*, 28(5):744–755. Elsevier.

Ziviani, D., I. H. Bell, X. Zhang, V. Lemort, M. De Paepe, J. E. Braun, and E. A. Groll

2020. Pdsim: Demonstrating the capabilities of an open-source simulation framework for positive displacement compressors and expanders. *International Journal of Refrigeration*, 110:323–339. Elsevier.

List of Publications and Presentations

Refereed Journals

1. **Abdan, S.**, Stosic, N., Kovacevic, A., Smith, I., and Asati, N. (2022). Oil drag loss in oil-flooded, twin-screw compressors. *Proceedings of the Institution of Mechanical Engineers, Part E: Journal of Process Mechanical Engineering*, 09544089221115493.
2. **Abdan, S.**, Patil, S., Stosic, N., Kovacevic, A., and Smith, I. (2023). Experimental validation of the screw compressor oil drag model for various rotor profiles. *Proceedings of the Institution of Mechanical Engineers, Part E: Journal of Process Mechanical Engineering*, 09544089231163514.

Conference Proceedings

1. **Abdan, S.**, Basha, N., Kovacevic, A., Stosic, N., Birari, A., and Asati, N. (2019, August). Development and Design of Energy Efficient Oil-Flooded Screw Compressors. In *IOP Conference Series: Materials Science and Engineering*, Vol. 604, No. 1, p. 012015. IOP Publishing.
2. **Abdan, S.**, Stosic, N., Kovacevic, A., Smith, I., and Deore, P. (2018, September). Identification and analysis of screw compressor mechanical losses. In *IOP Conference Series: Materials Science and Engineering* (Vol. 425, No. 1, p. 012015). IOP Publishing.
3. **Abdan, S.**, Stosic, N., Kovacevic, A., Smith, I., and Asati, N. (2019, August). Analysis of rolling bearing power loss models for twin screw oil injected compressor. In *IOP Conference Series: Materials Science and Engineering* (Vol. 604, No. 1, p. 012013). IOP Publishing.
4. **Abdan, S.**, Stosic, N., Kovacevic, A., Smith, I., and Asati, N. (2021, September). Estimation of radial shaft seal, oil drag and windage loss in twin screw oil injected compressor. In *IOP Conference Series: Materials Science and Engineering* (Vol. 1180, No. 1, p. 012010). IOP Publishing.

5. Tankhiwale, S., Dagwar, A., Rane, S., Kovacevic, A., Birari, A., **Abdan, S.**, and Asati, N. (2021, September). Numerical evaluation of an Oil free Screw Compressor's Suction Port design using Ansys CFX and SCORG. In *IOP Conference Series: Materials Science and Engineering* (Vol. 1180, No. 1, p. 012005). IOP Publishing.
6. Dundagekar, S.; **Abdan, S.**; Munde, A.; Patil, S.; and Asati, N. (2022) Experimental Investigation of the Effect of Oil Injection Flow Rate on the Performance of Oil-Injected Twin-Screw Compressor. In *26th International Compressor Engineering Conference, Purdue*. Paper 1442.